Surface and Bulk Transport of Samarium Hexaboride

by

Yun Suk Eo

A dissertation submitted in partial fulfillment
of the requirements for the degree of
Doctor of Philosophy
(Physics)
in the University of Michigan
2017

Doctoral Committee:

Professor Çağlıyan Kurdak, Chair
Emeritus Professor James W. Allen
Associate Professor Lu Li
Associate Professor Vanessa Sih
Associate Professor Kai Sun
Associate Professor Zhaohui Zhong

Yun Suk Eo
eohyung@umich.edu
ORCID iD: 0000-0002-8715-8649

Acknowledgements

I would like to thank, first and foremost, my parents, Jinwoo Eo and Jeonghyeon Kim, for always supporting me in everything I do. I would not have been able to complete this long journey without their endless love and support. I also thank Janet Eo for being a good sister. It was always great to have a family member also studying in the United States.

My deepest gratitude goes to my advisor, Professor Çağlıyan Kurdak. He always taught me physics in the most exciting way. There are so many things I learned from him that I cannot list all of them here. Just mentioning a few, I was greatly influenced by his emphasis on listening to the data while taking measurements. Also, I learned a lot by his encouragement for me to come up with any ideas while we think about physics.

One of the best parts of working on SmB_6 at Michigan was that I could interact with other professors very closely. Professor Kai Sun has always welcomed me when I visited his office, and answered all my questions, no matter how elementary they were. His insights on SmB_6, from a theoretical point of view, were always very helpful. It was always an enjoyment to learn about SmB_6 from a historical perspective from Professor James W. Allen. Also, I appreciate him for always considering my data seriously, and providing me with very thoughtful suggestions. I have also learned a lot from Professor Lu Li about the experimental aspects that are different from our group's work. Because of his presence, I was able to learn SmB_6 with a broader perspective.

I have also met fantastic group members. I really enjoyed working together with Alexa Rakoski, Juniar Lucien, and Dmitri Mihaliov. They helped me so much and were very kind to me during the last two years. Special thanks go to Dr. Steven Wolgast. I think my journey on SmB_6 was possible because of his successful work on the initial SmB_6 projects. Dr. Teoman Ozturk has also been a good friend. It was a pleasant experience reading SmB_6 papers together when we had both just started the projects. Although we did not directly work together, I think I learned a great deal from Dr. Elizabeth Covington and Dr. Richard Field III.

Outside of our group, I was very fortunate to meet good friends. I have learned a lot of experimental techniques from Dr. Gang Li, Dr. Ziji Xiang, Dr. Benjamin Lawson, Tomoya

Asaba, Colin Tinsman, and Lu Chen. Also, I enjoyed learning many-body physics from Jiahua Gu. I must note that the mentioned people above, in addition to our group members, formed the SmB_6 journal club, which was a very helpful and fun experience. Before working on SmB_6, I had a wonderful opportunity to work on graphene with Professor Zhaohui Zhong and Dr. Kyunghoon Lee for a brief period. In retrospect, what I learned from them about graphene had so many ties to topological insulators. I must acknowledge Dr. Mijin Yoon, Dr. Yongsoo Yang, Dr. Jieun Lee, Dr. Sunghoon Jung, Dr. Geehyun Kim, and Seonghoon Kim. Throughout my graduate school journey, I interacted a lot with them at the physics department.

At the Lurie Nanofabrication Facility, I must thank Dr. Nadine Wang and Dr. Pilar Herrera-Fierro. Whenever we had to start something new in the clean room, they were always the right scientists to ask for help. Of course, my experiments would not have been possible without the SmB_6 samples. I must, therefore, thank our collaborators who grew the crystals: Professor Zachary Fisk, Dr. Dae-Jeong Kim, Dr. Priscilla F. S. Rosa, Professor Byunggi Cho, Dr. Boyoun Kang, Myungsuk Song, Professor Geetha Balakrishnan, and Dr. Monica C. Hatnean.

Completing this dissertation would not have been possible without the guidance of my advisor, Professor Çağlıyan Kurdak. I must thank him again. Also, I especially would like to thank Alexa Rakoski for reading my dissertation carefully and catching so many typos and grammatical errors. Also, I appreciate Professor James W. Allen for carefully reading my dissertation and providing me with very thoughtful comments. Also, whenever I had a manuscript ready Professor Jean Krisch, my undergraduate academic advisor, also proofread them. I thank her for the kind suggestions and advice overall. Lastly, I would like to thank Dr. Elizabeth Hildinger, who taught me technical writing.

Funding for this work was provided by NSF Grants No. DMR-1006500, No. DMR-1441965, No. DMR-163145, and No. DMR-0801253. The PPMS system, which was used for cryogenic measurements, was acquired through the National Science Foundation MRI Award No. 1428226. The high-field experiments were performed at the National High Magnetic Field Laboratory, which is supported by NSF Cooperative Agreement No. DMR-084173 and No. DMR-1157490 by the State of Florida, and by the DOE. I acknowledge the University of Michigan College of Engineering for financial support and the Michigan Center for Materials Characterization for use of the instruments and staff assistance. I would also like to thank the financial support from the Physics Department at the University of Michigan, especially Student Services, who gave me the opportunity to teach classes for many semesters.

Table of Contents

List of Figures

List of Tables

List of Appendices

Abstract

There has been a renewed interest in SmB_6 during the past several years after the theoretical prediction that it is a topological Kondo insulator (TKI). Soon after, the conducting surface was experimentally discovered, which is the key initial step for the TKI verification. Motivated by this work, this dissertation further studies both the surface and the bulk properties of SmB_6 using electrical transport methods.

To study the surface transport of SmB_6, choosing the appropriate transport geometry is extremely important. A Corbino disk geometry, which confines the current path to a single surface, was used in this study. The measurements from the Corbino disk resulted in more physically acceptable values of carrier density than the results that were obtained from other conventional transport geometries. During this study, we also found that subsurface cracks that are created during surface preparation and domain boundaries of a polycrystal can provide unwanted conduction paths. After careful surface preparation, the magnetotransport was measured with an applied magnetic field of 34.5 T and a temperature of 0.3 K. A higher magnetic field was also applied up to 93 T, using the pulsed magnetic field, but Shubnikov de-Haas oscillations were not observed. Therefore, the strongest signatures needed to verify the nontrivial topology, such as the half-integer Landau index in the fan diagram have not yet been seen, nor were we able to find signatures of the three Fermi pockets predicted by theory.

Instead, the Corbino disk magnetotransport results were consistent with the case when only one Fermi pocket exists. This can happen when the mobilities for each of the pockets are too small. From analyzing our magnetotransport, possible ranges of carrier density and mobility of each of the three Fermi pockets could be constructed in a 2D parameter space. When comparing with these Fermi pocket ranges that were constructed by magnetotransport to other experimental reports, only the angle-resolved photoemission spectroscopy reports are within the X-pocket range.

To study the bulk of SmB_6, a new transport method was invented, called the inverted resistance measurement. This inverted resistance measurement can be used for studying the bulk of SmB_6 when the surface conduction dominates. By comparing the numerical

simulation and the experimental measurement, the bulk resistivity was successfully extracted in the low-temperature range, where previously this was impossible due to the overwhelming surface conduction.

Using this new method, we investigated the bulk of pure and disorder-induced SmB_6 samples. We find that the bulk of SmB_6 is an ideal insulator. The thermally activated behavior, with an activation energy of 4.01 meV, continues for ten orders of magnitude in resistivity. This thermally activated bulk behavior is found to be almost identical in the highly disordered SmB_6 samples. These results suggest that the bulk of SmB_6 has an energy gap that is free of impurity states, making the bulk transport remarkable. In addition to the thermally activated bulk behavior, in our disorder-induced samples, our measurements revealed a mysterious bulk resistivity plateau that has been buried under the surface conduction. This bulk plateau cannot be understood by normal impurity states. Instead, a new understanding of impurity and disorder may be required for the case of SmB_6.

Chapter 1

Introduction

1.1 Introduction to SmB_6: Early History

Samarium hexaboride (SmB_6) refers to a chemical composition of a material, which is studied in this dissertation. A crystal consists of atoms and molecules, and it has a repeating structure. The basic unit that repeats in the material is called a unit cell. In SmB_6, the unit cell is shown in Fig. (1.1) (a), and the repeating nature is shown in Fig. (1.1) (b). This unit cell consists of one samarium (Sm) and six borons (B). The boron atoms are arranged in an octahedral[1] structure. If one is familiar with the group theory notation (Hermann-Mauguin notation), the corresponding space group is $Pm\bar{3}m$, which is identical to cesium chloride (CsCl) [1]. The size of the unit cell can be represented by a lattice constant, which is $a = 4.133$ Å for SmB_6.

Metallic hexaboride crystal structures, in general, have been studied and confirmed by X-ray crystallography even in the early 1930s [2], and their electronic structure has been studied since the 1950s [3–5]. Finding the hexaboride orbitals from hybridization of the boron atomic orbitals is not as intuitive as finding hybridization orbitals of simple molecules such as ammonia (NH_3). H. C. Longuet-Higgins and M. de V. Roberts [3] have shown theoretically that the metallic hexaboride structure results in 10 bonding and 14 antibonding molecular orbitals in the metallic hexaboride structure. The 10 bonding orbitals try to become filled, requiring a total of 20 electrons. The electronic configuration of a boron atom itself is $[He]2s^2 2p^1$, so 18 electrons (3 e/boron $\times$ 6 borons) can be filled by the six borons. Then, the two remaining electrons must be acquired from the metallic atom. The understanding around the 1950s was that, when only considering s and p orbitals, the hexaborides formed with divalent metals are insulators, and the hexaborides formed with trivalent metals are

[1] The prefix octa- comes from the fact that it has eight faces.

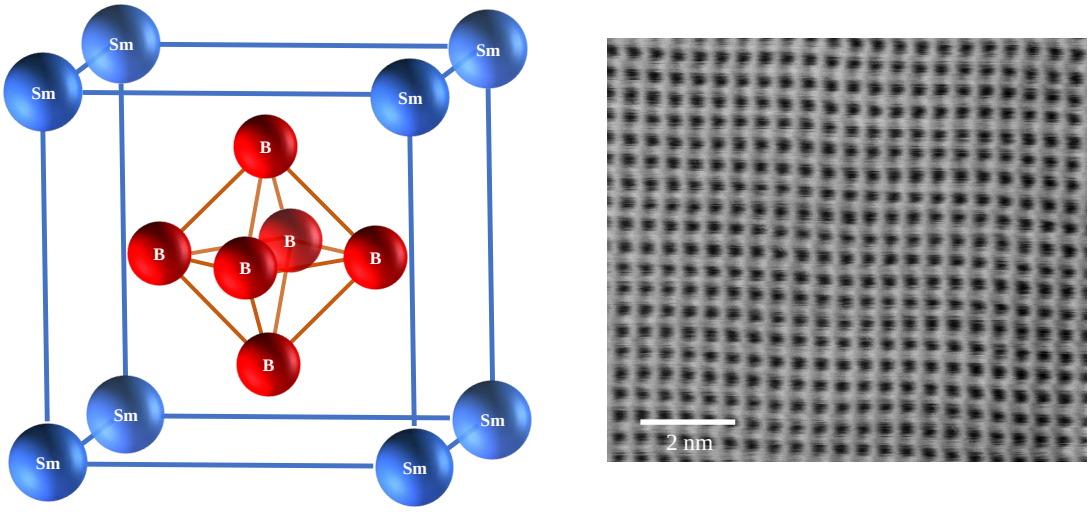

Figure 1.1: SmB_6 crystal structure. (a) Unit cell of SmB_6 (b) The periodic structure (lattice) of SmB_6 seen by TEM. Figure courtesy of A. Rakoski.

metals [3, 4].

The electronic configuration of a Sm atom is $[Xe]4f^6 6s^2$. Samarium is particularly interesting because it has f electrons, which occupy localized orbitals that can potentially result in magnetic moments in the material[2]. For SmB_6, one of the first transport studies was done by A. Menth, E. Buehler, and T. H. Geballe in the late 1960s [7]. Of course, the band structure of SmB_6 was not known at the time (50s - 60s). Nevertheless, their primary goal was to understand the relation of the electric and magnetic properties of SmB_6. They measured the magnetic susceptibility and concluded that SmB_6 has no magnetic ordering at low temperatures. Their interpretation was that Sm is in the $4f^6$ state (Sm^{2+}) since $J = 0$. This made sense in that the two electrons in the $6s^2$ can be taken away from B_6, according to the hexaboride theory from H. C. Longuet-Higgins *et al.*, and the $4f^6$ electrons remain together. Also, the resistance increased as the temperature was lowered, so they concluded that SmB_6 at low temperature is an insulator. At high temperatures, they see a Curie-Weiss-like susceptibility behavior. They interpret this behavior is due to the Sm magnetic moments in the $4f^5$ state (Sm^{3+}), resulting from the loss of one electron by thermal excitations. Also, the resistivity vs. temperature shows a metallic behavior at this range. Therefore, Menth *et al.*'s interpretation of SmB_6 was that at low temperatures the Sm is in the 2+ valence state, and SmB_6 is insulating, and at high temperatures the valence of

[2]I must acknowledge that this summary was greatly influenced by Prof. J. W. Allen's historic review of SmB_6 [6]. The history introduced in is chapter is a very trimmed down version, and I recommend the reader to watch the video for a more complete story.

Sm changes to 3+, and SmB_6 becomes metallic. This interpretation was acceptable at that time, although the researchers did not know the electronic band structure of SmB_6. One year later in 1970, the same researchers, together with G. W. Hull, measured SmB_6 doped with Eu^{2+} and Gd^{3+} [8]. In this study, they show that the resistivity of the Gd-doped SmB_6 drops drastically compared to the Eu-doped SmB_6. This is consistent with their picture that an increasing number of atoms in the 3+ valence state will become less insulating.

In the studies by Menth *et al.*, the resistivity vs. temperature was mostly consistent with a narrow gapped insulator ($R \propto \exp(E_a/k_BT)$). However, at temperatures below ~3 K, there was a mysterious plateau that they attribute to an impurity band conduction, but did not investigate in great detail as it was not the main focus of their study. Although not known as well as the report by Menth *et al.*, there is also another report that was published almost at the same time by Yu. B. Paderno, V. I. Novikov, and E. S. Garf that focused on the general electrical properties of various metallic hexaborides [9]. They also report the resistivity plateau of SmB_6 at low temperatures, and they mention that the plateau appears continuously in samples, independent of the crystal growth method. 40 years later by our group, this plateau becomes identified as a surface conductor. We will discuss this in Sec. 1.3.

In 1970, very soon after the reports by Menth *et al.*, their interpretation of the valence change was challenged by the reports from R. L. Cohen, M. Eibschutz, and K. W. West [10]. R. L. Cohen *et al.* study Mössbauer spectroscopy and see that the valence of Sm is neither a 2+ nor 3+. In contrast to what was explained by Menth *et al.*, their susceptibility measurement fits well with a linear combination of 40 % of Sm^{2+} and 60 % of Sm^{3+}, resulting in a non-integer valence (2.6+) that is almost independent of temperature. This result meant that SmB_6 cannot be understood by an integer valence change from 3+ to 2+, suggested by Menth *et al.* It is worth to mention that samarium sulfide was also studied during this era (the early 1970s). In 1970, A. Jayaraman, V. Narayanamuri, E. Bucher, and R. G. Maines find that an insulator-to-metal transition happens when a pressure is applied [11]. At room temperature and ambient pressure, SmS is an insulator, called the black phase, and becomes a metal at 6.5 kbar, called the gold phase. Similar to Menth *et al.*'s interpretation, they attribute this behavior from a change in Sm valence from 2+ to 3+. A year later, in 1971, M. B. Maple and D. Wohlleben further studied the susceptibility of SmS [12]. Their measurement of susceptibility in the gold phase is similar to the one of SmB_6 measured from Cohen *et al.* in that the valence of SmS also does not demonstrate an integer value shift. The materials such as SmB_6 and SmS became categorized into (homogeneous) mixed valence compounds in which the valence of an atom is not in an integer state [13].

As mentioned before, to tell if the material is an insulator or a metal with confidence, one should refer to the band structure. The minimum requirement is that we look at the band

structure near the Fermi energy. The relevance of band theory to transport will be discussed in more detail in the following chapter (Chapter 2), but the bottom line is that if the Fermi energy crosses one of the bands, we know the material is a metal, whereas if the Fermi energy lies in the forbidden gap between two bands, we know it is an insulator. However, the band structure of SmB_6 was not known in the early 1970s, as it had just became appreciated as a mixed valence material. Thinking that SmB_6 and the gold phase of SmS belong in the same class, and a general perception that mixed valent compounds are metallic [13], researchers had doubts that SmB_6 is an insulator, and it is a metal instead [14][3]. In the metal scenario, the resistivity rise by lowering the temperature seen by researchers [7, 15] can be explained as a mobility (μ) change by a Kondo-like $f-d$ scattering instead of the carrier density (n) change.

What was understood about mixed valence systems in the 1970s is that the $4f$ (ionization) energy levels are separated by a large Coulomb interaction (U), and at least one of them crosses the dispersive band (d band in the case of SmB_6). Then, the width of the f band broadens, and the Fermi energy lies at the broadened peak [13, 16]. If SmB_6 involves this picture only, it is a metal because the Fermi energy crosses a band. To consider SmB_6 to be an insulator instead, a gap must somehow exist where the Fermi energy is located. In 1974, N. F. Mott proposed that f and d bands can hybridize and form a gap, and suggested that this mechanism can explain the insulating behavior of SmB_6 [17]. It is also important to note that the possible gap opening was developed in another way, started by S. Doniach. S. Doniach introduced a model called a Kondo lattice in which the local moments are located in an array that interacts with the conduction electrons [18]. The idea is tied intimately to the Kondo effect, which describes the scattering of conduction electrons by magnetic impurities [19]. In the Kondo effect, the scattering enhances at a lower temperature. This scattering is related to the conduction electron and magnetic moment of the impurity forming a singlet. In S. Doniach′s model, using the same kind of antiferromagnetic interaction in the Kondo effect, he explained the moment loss from the exchange interaction between the f and d electrons. Later, C. Lacroix and M. Cyrot further developed this model and constructed a phase diagram. Under certain exchange interaction strength compared to the bandwidth of the conduction band [20, 21], the gap opens at the hybridization between the f and d bands. This dual history is related to why SmB_6 is referred to as a Kondo insulator after the early 1990s [22], and not only as a mixed-valent insulator. In both descriptions, if a band gap opens and the Fermi energy lies in that gap, the material is an insulator.

The more realistic band gap opening model was proposed later by R. M. Martin and J.

[3] In fact, Prof. Allen remembers in the mid 70s, the community thought SmB_6 was a metal although researchers have not published such ideas that much [6].

W. Allen, where they referred to the band structure of LaB_6 to estimate the d bands, and carefully considered the symmetry of the f levels of SmB_6 [23,24]. This band gap model was motivated after the Hall measurement from J. W. Allen, B. Batlogg, and P. Wachter [25] in 1979. At the time, the increasing resistivity by lowering the temperature was thought as either SmB_6 being a metal or an insulator. In the metal scenario, the resistivity rise by lowering the temperature is from a Kondo-like scattering mechanism. In the insulator scenario, the increase in resistivity by lowering the temperature is from the carrier density decrease. To distinguish the two, the mobility (μ) and carrier density (n) needed to be separated from the conductivity ($\sigma = ne\mu$). This is why the Hall coefficient ($R_H = 1/ne$) had to be measured. An earlier Hall measurement was taken by J. C. Nickerson *et al.* in 1971 [15], but it was not clear enough to claim that SmB_6 is either a metal or an insulator because their resistivity magnitude change was only a factor of $\sim$2.5. J. W. Allen *et al.* measured the Hall effect in 1979 [25] with high-quality crystals and demonstrated the resistivity rise of four orders of magnitude. The large resistivity magnitude at low temperatures already suggested that the temperature dependence rules out the metal scenario involving scattering by magnetic moments because their resistivity magnitude exceeds the allowed scattering limit, so-called the unitarity limit [26]. Also, in their Hall effect measurement, they saw a large thermally activated behavior. This is consistent with the picture of an insulator, where the carrier density changes with temperature.

However, at low temperatures, they also observed the mysterious resistivity plateau that was continuously observed since 1969 by A. Menth *et al.* and Yu. B. Paderno *et al.* [7, 9], and they had trouble explaining the origin using impurity conduction. J. W. Allen *et al.* calculated the Mott impurity limit, which is the minimum conductivity allowed for the resistivity plateau to be attributed to impurity conduction, and found that its value exceeded this limit by a factor of 15 [25]. Other researchers such as T. Kasuya, K. Kojima, and M. Kasaya tried to explain this feature by variable range hopping in 1977 [27], but two years later T. Kasuya and his collaborators realized that their estimation was also unphysical [28][4].

1.2 Topology in Condensed Matter Physics

In this section, we will pause our discussion on SmB_6, and discuss topology in a solid. Topology is a subfield of mathematics that studies the properties of objects. More specifically, if an object can be smoothly deformed into another object, the two objects are topologically indistinguishable. For example, a sphere and an ellipsoid are topologically identical. However, if one needs to punch a hole or tear the object to change from one object to another,

[4] They alternatively proposed that SmB_6 [28] forms a Wigner lattice.

then the two objects are topologically distinct. For example, a sphere and a donut (torus) are topologically distinct.

To categorize objects (more precisely manifolds) in this way, mathematicians have developed a label called the Euler characteristic, χ. If the manifold, M, is closed, χ can be found by a surface (S) integral of the curvature, K:

$$\chi = \frac{1}{2\pi} \oint_M K dS. \tag{1.1}$$

From Eq. (1.1), we can find if two objects are topologically identical. For example, a sphere and an ellipsoid both have $\chi = 2$, and a donut has χ=0.[5]

The integer quantum Hall (IQH) effect is one of the earliest examples that use topology in solid state physics. In a high-quality two-dimensional electron gas (2DEG) system, when a perpendicular magnetic field is applied, the Hall conductivity becomes quantized at certain levels:

$$\sigma_{xy} = N \frac{e^2}{h}. \tag{1.2}$$

This is the IQH effect that was discovered by K. von Klitzing in 1980 [29]. In the IQH state, the 2DEG is an insulator in which the electrons form a closed cyclotron orbit, but at the boundary of the sample, electrons move in a skipping motion, which is also referred to as a chiral edge state. In 1982, Thouless, Kohmoto, Nightingale, and den Nijs (TKNN for short) explained the quantized Hall conductivity using topology [30]. As a brief summary of the idea, if $u(\vec{k})$ is the Bloch part of the wave function, with crystal momentum, $\vec{k}$, we define the Berry phase that integrates around the boundary of the Brillouin zone (BZ):

$$\gamma = -\sum_n \oint_{\partial BZ} dk \cdot \vec{a}_n, \tag{1.3}$$

where $\vec{a}_n$ is called the Berry connection for the n'th band, defined as:

$$\vec{a}_n(\vec{k}) = -i < u_n(k) | \frac{\partial}{\partial \vec{k}} | u_n(k) > \tag{1.4}$$

It turns out that the the integer N, in the quantized Hall conductivity in Eq. (1.2), is related to the Berry connection by:

$$N = \frac{1}{2\pi} \sum_n \oint_{\partial BZ} d\vec{k} \cdot \vec{a}_n. \tag{1.5}$$

[5] A famous example is that a donut and coffee cup have the identical Euler characteristic.

Alternatively, we can use Stokes′ theorem and express this as:

$$N = \frac{1}{2\pi} \sum_{n} \oint_{BZ} \vec{A}_n \, d^2\vec{k}. \tag{1.6}$$

where $\vec{A}_n$ is called the Berry curvature in the crystal momentum space, defined as:

$$\vec{A}_n = \nabla_{\vec{k}} \times \vec{a}_k. \tag{1.7}$$

Notice that there is a resemblance between Eq. (1.1) and Eq. (1.6). However, the difference is that we are integrating the sum of the Berry curvatures instead of the curvature of the manifold, and integrating the BZ instead of the manifold (M) in real space. One can see that this formalism is based on the wave function (Bloch wave function) of the material and not related to the curvature of the real sample. Therefore, the topology that is related in this context is not about the shape of real objects. It is related to the mathematical structure of the electron wave function. What is important for an experimentalist is that the topology has measurable consequences such as Eq. (1.2).

The 2DEG that is in the IQH state is an insulator in the sense that the electrons form a closed cyclotron orbit and becomes inert, but it is a nontrivial insulator because of the presence of the chiral edge modes at the boundary of the sample. The nontrivial topology information is encoded in the value N, in Eq. (1.6), not being zero. Another way theorists view this is that the insulator of a quantum Hall state ($N = 1, 2, ..$) cannot be adiabatically deformed into a vacuum, which is a trivial insulating state. Bands of most well-known insulators can be adiabatically deformed into a vacuum, and they are classified topologically trivial.

A topological insulator is an insulator that has a nontrivial topological structure encoded in the electron wave function, just like the IQH effect. However, the IQH state is not the topological insulator that researchers refer to nowadays. Notice that in σ_{xy}, $N \neq 0$ in Eq. (1.2), can only be obtained when the magnetic field is applied to the 2DEG. In other words, time-reversal symmetry must be broken to achieve a topologically nontrivial insulating state. The topological insulators we refer today are materials that have nontrivial topology while the time-reversal symmetry is preserved. An important ingredient is strong spin-orbit coupling. In 2005, C. Kane and E. Mele proposed a model of graphene with spin-orbit coupling that can realize a quantum spin Hall insulator [31]. It turns out that the spin-orbit coupling in graphene is too small for this to be realized, but they noticed that their model has a topology that is nontrivial even without breaking the time-reversal symmetry. In their work, C. Kane and E. Mele proposed a topological index called $\mathbb{Z}_2$ [32]: $+1$ if the topology

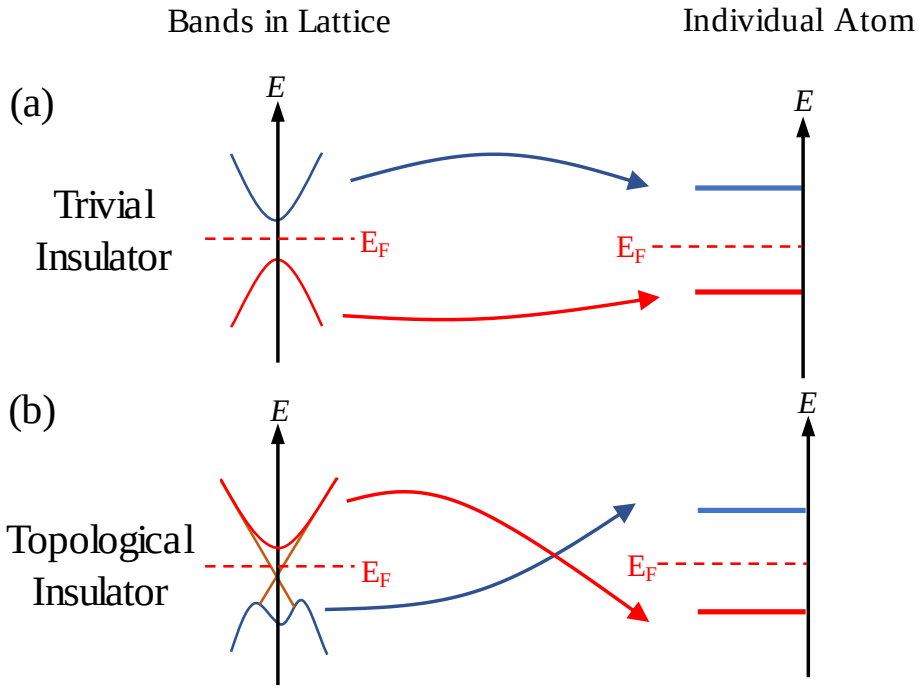

Figure 1.2: Idea of band inversion. Adiabatic atomic separation from an insulator to an atom. (a) Trivial insulator. No band inversion. (b) Band inversion of a topological insulator.

is trivial, -1 if nontrivial. Soon after their work, B. Bernevig, T. Hughes, and C. Zhang proposed a quantum spin Hall effect that can be realized in CdTe/HgTe/CdTe quantum wells [33]. In 2007, this effect was experimentally verified by L. Molenkamp's group [34].

This idea of $\mathbb{Z}_2$ topology in materials that preserve time-reversal symmetry was expanded to a three-dimensional version by L. Fu, C. Kane, E. Mele [35], and J. Moore and L. Balents [36]. In 3D systems, there are four $\mathbb{Z}_2$ indices that categorize the topology of materials. Depending on the indices, there can be weak 3D TIs and strong 3D TIs. When the topological indices are nontrivial, this is what we call today a 3D Topological insulator (TI). The interpretation, roughly speaking, is that if we were able to separate the atoms in the material slowly, the band structure of the material deforms into atomic energy levels, as shown in Fig. (1.2). If the order of the bands does not change, then the material has a trivial topology, as shown in Fig. (1.2) (a). If the order of the conduction band and valence band invert, as shown in Fig. (1.2) (b), then the material has a nontrivial topology, and leaves a gapless edge state, as shown in orange. Because the edge state crosses the Fermi energy, it manifests a conducting state at the surface. L. Fu and C. Kane soon developed a simple and powerful way to distinguish topological insulators from trivial insulators when the material

has inversion symmetry in addition to time-reversal symmetry [37]. What is most important here is that they predict that surface states will have the following unique properties that can be verified by experiments: odd number of Dirac cones, the spin of the electrons being locked to the crystal momentum direction (helical spin structure), and lack of backscattering, resulting in weak antilocalization. They predicted that $Bi_{1-x}Sb_x$ is a 3D TI, with the mentioned surface properties. In 2008, D. Hsieh and others from Z. Hasan's group verified this prediction experimentally from angle-resolved photoemission spectroscopy (ARPES). To date, there are many 3D topological insulators that have been verified [38, 39].

It is important to note that when L. Fu and C. Kane proposed a way to distinguish 3D TIs with inversion symmetry in addition to time-reversal symmetry, theorists had gained a powerful tool to search for 3D TIs in many other materials [37]. The $\mathbb{Z}_2$ topology index can be calculated by:

$$(-1)^{\nu} = \prod_{n=1}^{8} \prod_{i=1}^{N} \xi_n(\Gamma_i), \tag{1.8}$$

where ν is the topological index (+1 or -1), n is the band index for filled bands, and $\xi_n(\Gamma_i)$ is the parity eigenvalue at one of the eight high symmetry points (Γ_i). Notice that the dispersion of the bands are irrelevant in this calculation except at the high symmetry points. This is extremely powerful because, even for a complicated band structure that is not fully known, the topology can still be found as long as the parities of the bands at the high symmetry points are known.

1.3 Topological Kondo Insulators

We come back to our discussion of SmB_6. It is interesting to note that when R. M. Martin and J. W. Allen proposed their gap model of SmB_6 [24], they did notice that the hybridization cannot take place at the X and Γ high symmetry point in the BZ because the parity is violated. Instead, they proposed that the hybridization takes place along the Δ line (Γ to X) to avoid the parity violation.

About 30 years later, in 2010, M. Dzero, K. Sun, V. Galitski, and P. Coleman considered the topology in Kondo insulators by using the criterion of Eq. (1.8) [41]. They predicted that SmB_6 is almost at the border of a weak and strong topological insulator. In 2011, T. Takimoto specifically focused on SmB_6 and claimed that SmB_6 is a strong topological insulator, with three Dirac pockets in the BZ, existing on the (001) surface [42]. These theoretical predictions had an important impact on both the traditional SmB_6 community and the 3D TI community. If SmB_6 could be a 3D topological insulator, it also had the possibility to explain the mysterious resistance plateau that puzzled the researchers.

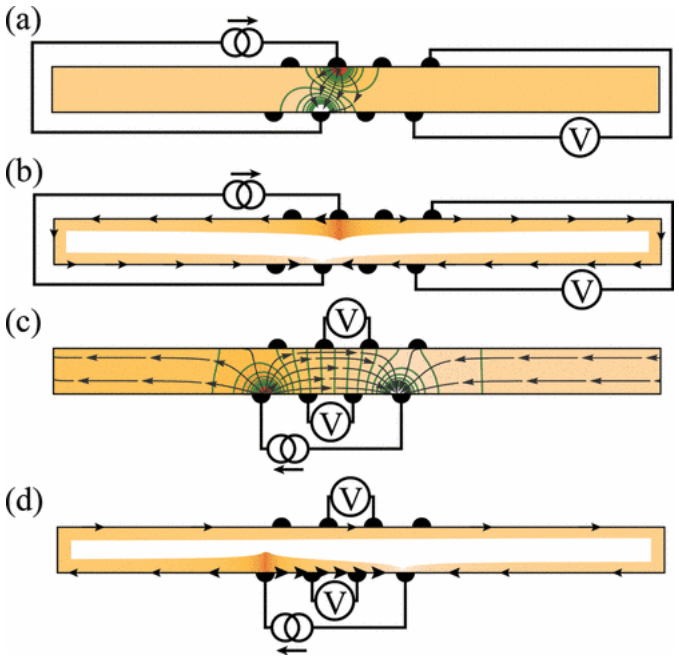

Figure 1.3: Transport configuration to verify the surface states of SmB_6 that was performed by S. Wolgast *et al*. (a) Bulk origin scenario of the vertical configuration transport. (b) Surface origin scenario of the vertical configuration transport. (c) Bulk origin scenario of the lateral and hybrid configuration transport. (d) Surface origin scenario of the lateral and hybrid configuration transport. Reprinted figure with permission from [40], and also additional kind permission from the first author. Copyright (2013) by the American Physical Society.

In 2012, to verify that the resistance plateau is from the surface conducting state, S. Wolgast, Ç. Kurdak, K. Sun, and J. W. Allen used a nonlocal transport geometry on a slab-shaped SmB_6 sample, grown by D. J. Kim and Z. Fisk [40]. If the resistivity behavior, both the high temperature and low temperature, is purely a bulk phenomenon, the resistance, R, must always be inversely proportional to the bulk conductivity, σ_b:

$$R = \frac{C_b}{\sigma_b}. \tag{1.9}$$

If this is the case, two resistances that are measured with different contact configurations will only differ by a prefactor (C_b)[6], so the ratio of the two resistances will always be constant.

On the other hand, if the high-temperature region is from the bulk conduction and the low-temperature region is from the surface conduction, Eq. (1.9) only holds approximately true at high temperatures, and at low temperatures, the resistance is more dominated by

[6]We will introduce C_b and C_s as C_{-1} and C_1/t, respectively, in Chapter 4.

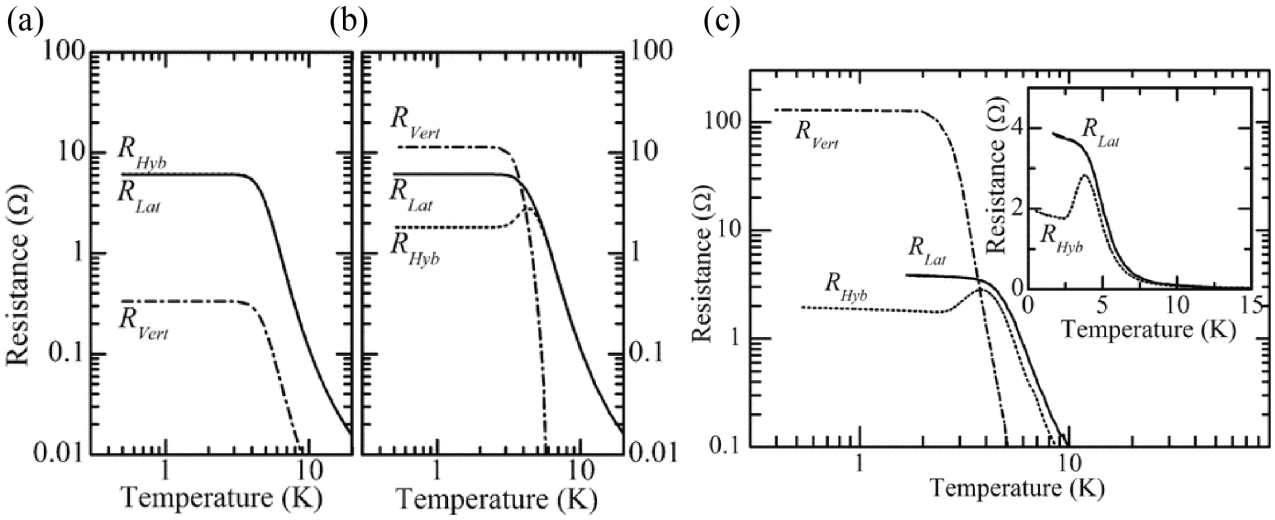

Figure 1.4: Numerical simulations and experimental results of the non-local transport geometry that were performed by S. Wolgast *et al*. (a) Simulation of SmB_6, assuming that both high- and low-temperature resistance originate from the bulk only. (b) Simulation of SmB_6, assuming that the low-temperature resistance plateau originates from the surface. (c) Experimental result of R vs. T. Reprinted figure with permission from [40], and also additional kind permission from the first author. Copyright (2013) by the American Physical Society.

the surface conductivity, σ_s:

$$R \approx \frac{C_s}{\sigma_s}, \tag{1.10}$$

with a different prefactor, C_s. C_b is determined by how the current flows in bulk, and C_s is determined by how the current flows on the surface, and they are not the same (even the units are different). Therefore, if the surface conduction is responsible for the resistance plateau, in contrast to the bulk conduction at high temperatures, the two resistance measurements with different contact configurations will have different values of transition, C_b to C_s, as the temperature is lowered. This is the key idea that S. Wolgast *et al*. used to verify the conducting surface. They used three different contact configurations. If the resistance is purely from a bulk origin, the current will flow as shown in Fig. (1.3) (a) and Fig. (1.3) (c), whereas if the conducting origin is from the surface, the current will flow as Fig. (1.3) (b) and Fig. (1.3) (d). The numerical simulations for the corresponding configurations are shown in Fig. (1.4) (a) and Fig. (1.4) (b) for both the purely bulk scenario and the transition from bulk to surface state scenario, respectively. S. Wolgast *et al*. measured three different resistance configurations, and found that the resistance vs. temperature measurements do indeed follow the surface conduction scenario, as shown in Fig. (1.4) (c). This measurement clearly resolved the mystery of the resistance plateau. Soon after, many other experimental reports came

out, including many other transport experiments, dHvA studies, ARPES studies, tunneling spectroscopy studies, etc. Many of them support the picture of the 3D TI, although many others disagree with the picture of the 3D TI.

The work in this dissertation started soon after the discovery of S. Wolgast *et al*. The work by S. Wolgast *et al*. opened up a wide range of new experimental questions that must be answered to fully understand SmB_6. Of course, the most important question the researchers ask is: "Is the surface state really from a nontrivial topological origin?" To fully answer with confidence, we must verify the key signatures that L. Fu *et al*. suggested for satisfying 3D TI surface (odd number of Dirac cones, helical spin structure, etc.). Also related to this question, we must resolve the disagreement among other experimental results that have been reported by many groups[7].

From a slightly different perspective, 2DEG physics becomes immediately important as soon as a 2D conducting surface is discovered. Historically, notice that a new 2DEG platform, with high quality, has provided exciting discoveries, including IQH effect, fractional quantum Hall effect [43], Dirac fermions in graphene [44, 45], and many more. Related to this, we must answer: "What is the quality of the 2DEG of the SmB_6 surface?"

Lastly, when comparing to the weakly correlated 3D TIs, in which the bulk overwhelms the surface because of the existence of hopping conduction, it is fascinating that the surface conducting state in SmB_6 can be measured without interference from the bulk if the temperature is low enough. This is because the bulk carrier density continues to become smaller at low temperatures, not being disturbed by the presence of impurities. This implies that the role of disorder and impurities in SmB_6 may play a very different role than in other materials. Therefore, the bulk must also be investigated related to this aspect.

[7]The related references will be cited in Chapter 3.

Chapter 2

Understanding the Properties of Solids from Resistance Measurements

2.1 Introduction

Throughout this dissertation, the experimental technique that is used to understand the properties of SmB_6 is electrical transport close to zero frequency (DC limit). Transport measurements are typically performed on samples with multiple contacts where resistance, R, is obtained by passing a current, I, and measuring the voltage, V: $R = V/I$. When we measure the resistance, we typically change the conditions of the environment that surround the material. Many parameters of the sample′s environment can be controlled during the measurement of R. In this work, we control the temperature, T, and the magnetic field, B. The dependence of resistance on these two parameters, $R(T)$ and $R(B)$, contains valuable information about the material property. For example, $R(T)$ increases as T is lowered when the material is an insulator. We need to understand why this is the case. This chapter is, therefore, devoted to touching on the basics of transport theory. The subsections are designed in a sequence so that the reader can understand how a measured resistance can be used to understand fundamental properties of a solid. The connection between transport and band theory will be emphasized in this chapter. Also, we will mention whenever there is a difference between an ordinary material and a 3D TI while introducing key ideas of transport and band theory.

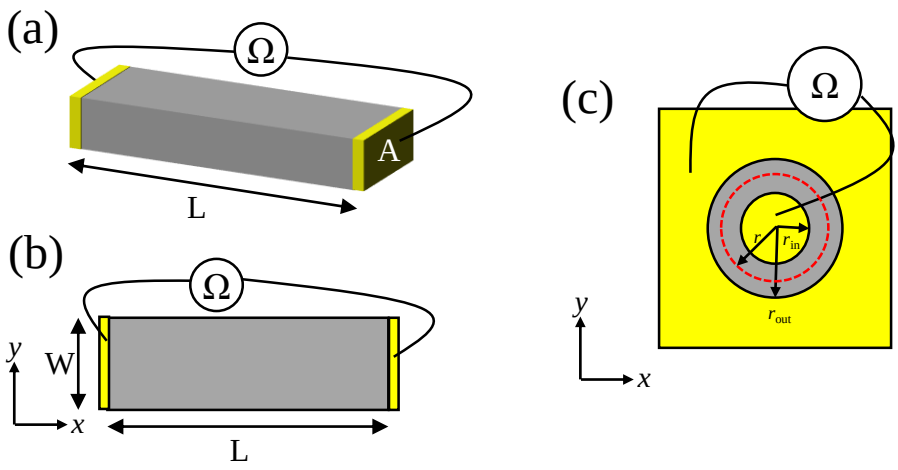

Figure 2.1: Basic transport geometries. The gray color is the sample and yellow is a highly conductive metal. (a) 3D slab geometry. (b) 2D sheet geometry. (c) Corbino disk geometry. Dotted line is the Gaussian surface for integration.

2.2 Resistance to Conductivity: Ohm′s law

When we measure the resistance, R, of a sample, we apply a current, I, through the sample and measure the voltage, V (i.e., $R = V/I$), across the sample[1]. Here, we only consider the resistance when the current is sufficiently small, so that I and V have a linear relationship (Ohmic regime).

The measured resistance, R, is then expected to depend on the shape, position of the contacts, as well as the type of material of the sample. Suppose we measure a resistance of a slab sample that is shown in Fig. (2.1) (a). We intuitively know that the carriers will experience more of the material if the sample is longer, and feel less when the cross-sectional area is larger. Therefore, the resistance of the slab sample shown in Fig. (2.1) (a) scales with length, L, and inversely scales with the cross-sectional area, A. That is:

$$R = \frac{V}{I} = \frac{1}{\sigma_b}\frac{L}{A}. \tag{2.1}$$

In addition to the geometry of the sample, the resistance also depends on the type of material (Cu, Ag, Si, SmB_6, etc.). This information is contained in the bulk conductivity, σ_b. Therefore, if we want to understand the material property by transport (measuring the resistance), we must first know the conductivity from the resistance.

This intuition of geometry also holds for a two-dimensional case. If electrons are confined

[1]One can measure the resistance alternatively by applying a voltage and measure the current.

in a two-dimensional space, this system is called a two-dimensional electron gas (2DEG). Consider a sheet sample that is shown in Fig. (2.1) (b). We know that the resistance increases as the length, L, increases, and the resistance decreases as the width, W, increases. Therefore, we have the following relation:

$$R = \frac{V}{I} = \frac{1}{\sigma_s}\frac{L}{W}, \tag{2.2}$$

where σ_s is the surface conductivity. Note that in Eq. (2.1), σ_b is in units of $1/(\Omega \cdot \text{cm})$, in Eq. (2.2), σ_s is in units of $(1/\Omega)$. We were able to easily guess Eq. (2.1) and Eq. (2.2) because the current in Fig. (2.1) (a) and Fig. (2.1) (b) flows uniformly.

In order to analyze general transport geometries with irregular shapes, we must consider a more general form that works for transport geometries of any shape. This is the differential form of Ohm′s law, which we learn from classical electrodynamics [46, 47]:

$$\vec{J} = \sigma\vec{\mathcal{E}}, \tag{2.3}$$

where $\vec{J}$ is the current density, and $\vec{\mathcal{E}}$ is the electric field.

Here we introduce a slightly more complicated geometry, as shown in Fig. (2.1) (c). This is a ring-shaped sample in 2D, also famously known as the Corbino disk. The current flows radially in the annular region for this geometry. To find the resistance of this geometry, let us consider a circular loop that is shown in a red-dotted circle (Gaussian circle). The current is enclosed in this circle, so integrating the current density, which is the left-hand side of Eq. (2.3), of an enclosed circle will be the total current, I, that is being applied to the Corbino disk. Also, from symmetry, we know that $\vec{\mathcal{E}}$ is always in the radial direction ($\hat{r}$) and the magnitude is constant along the circumference of the red-dotted circle. Integrating the right-hand side of Eq. (2.3) along the enclosed loop is:

$$\sigma_s \oint \vec{\mathcal{E}}\, dl = \sigma_s\, \vec{\mathcal{E}}\, (2\pi r). \tag{2.4}$$

Since Eq. (2.4) is equal to I, the electric field can be expressed as:

$$\vec{\mathcal{E}} = \frac{I}{2\pi r}\frac{1}{\sigma_s}\, \hat{r}. \tag{2.5}$$

By integrating the electric field in the radial direction from r_{in}, the inner radius of the disk, to r_{out}, the outer radius of the disk, results in the potential difference (or voltage) between the inner- and the outer-region of the annulus. Then, the resistance is found by dividing this

voltage to the current:

$$R = \frac{1}{\sigma_s}\frac{\ln(r_{\text{out}}/r_{\text{in}})}{2\pi}. \tag{2.6}$$

We will use this transport geometry when analyzing the surface of SmB_6 in Chapter 3. In other complicated geometries, we no longer have a good way to find the resistance analytically. The problem becomes even more complicated when the bulk and surface conductivity both exist in the sample. In fact, a 3D topological insulator is exactly this case. The geometry consideration for this case is challenging. We will discuss how we overcome this challenge in Chapter 4. In most other geometries besides the cases in Fig. (2.1), finding the resistance from Eq. (2.3) cannot be done analytically, and we must use numerical calculations instead.

In this section, we have reviewed how the resistance depends on the geometry of the sample and the conductivity of the material. If we can find the conductivity, then we must know how it is related to the microscopic details of the material. The approach we will take in the following sections is that we start from a more fundamental physics knowledge with certain assumptions and find a linear relationship between the electric field and the current density. From this, we will find the conductivity, and we will find that it can be expressed in terms of fundamental quantities of a solid. Here we do this twice following a historical sequence: the classical way (Drude model), and then the semiclassical way (Boltzmann model). From this sequence, we understand from the crudest properties to the more detailed properties of a solid.

2.3 Conductivity from Classical Transport Theory

In the previous subsection, we have mentioned that Ohm′s law (Eq. (2.3)) can be used to find the relation between the resistance and the conductivity of the sample. We want to know more about σ in detail, and from it, we want to understand the properties of solids. Let us try to find Eq. (2.3), where the current density is proportional to the electric field. The prefactor will be the conductivity. We introduce the idea of freely moving charged particles in a solid to justify Eq. (2.3).

How should we define the current density, $\vec{J}$, in terms of charged carriers? It should depend on the charge of each carrier (e), the density of the carriers (n), and the (drift) velocity of the carriers (v). We just multiply them all together:

$$\vec{J} = ne\vec{v}. \tag{2.7}$$

By defining the current density this way, we have assumed that every carrier behaves identically with the same drift velocity. Then, we can first consider a single carrier and then scale

with the carrier density afterward. Of course, this is an oversimplification, and we will later modify Eq. (2.7) based on our knowledge of statistical mechanics of fermions (i.e. electrons) in non-equilibrium.

Next, we need to find a linear relationship between $\vec{J}$ and $\vec{\mathcal{E}}$. According to Newtonian mechanics, a particle must accelerate when there is an external force. Then, the charged carriers must accelerate if the applied electric field is the only external force present in the system: $\vec{F} = e\vec{\mathcal{E}} = m\vec{a}$. Since we want the velocity to be proportional to the electric field, instead of the acceleration, we need to additionally introduce a drag force of $\vec{F_d} = m\vec{v}/\tau$ in the equation of motion:

$$\vec{F} = e\vec{\mathcal{E}} - m\vec{v}/\tau, \tag{2.8}$$

where τ is the relaxation time. At steady state, $\vec{F} = 0$, and we then arrive at a relation between velocity and electric field:

$$\vec{v} = e\tau/m\vec{\mathcal{E}}. \tag{2.9}$$

Inserting Eq. (2.9) in Eq. (2.7), we then have:

$$\vec{J} = ne\frac{e\tau}{m}\vec{\mathcal{E}}. \tag{2.10}$$

Comparing Eq. (2.10) with Eq. (2.3), the conductivity is:

$$\sigma = \frac{ne^2\tau}{m} = ne\mu, \tag{2.11}$$

where we have defined the mobility, $\mu = e\tau/m$. The approach in this section to find the conductivity is called the Drude model, and Eq. (2.11) is the famous Drude conductivity. From this model, we have found the conductivity from Newtonian mechanics after making some crude modeling and assumptions. Based on this development, the conductivity depends on the density of carriers in the material and some scattering (relaxation) time. This way of thinking works extremely well for many materials. However, when it comes to attempting to understand what those carriers exactly are (they are not electrons in a vacuum), and what n and μ are in a classical way, the model fails to explain correctly. Perhaps most seriously, the model does not capture why some materials are metals and why other are insulators.

In the following section, we will briefly review our knowledge of band theory from introductory solid state physics. Then, we will introduce the semiclassical transport theory. We will come back to the current density, $\vec{J}$, with a more sophisticated definition than Eq. (2.7), and find the conductivity that is related to the band structure of the material. From this, we will correctly interpret the meaning of carrier density and mobility.

2.4 Band Theory in a Nutshell

To understand basic electrical properties of a solid, we need to start from band theory of solids. This section is designed for the reader to learn how to read the dispersion relation and the density of (energy) states. Before moving on, we note that the review here is based on weakly correlated materials.

Understanding materials using band theory is one of the greatest success of quantum mechanics in the 20th century. In quantum mechanics, we solve the Schrödinger equation with a given Hamiltonian, H, that describes the system of interest. For a material, the system consists of a collection of ions (with charge Ze) and electrons. We can write the corresponding Hamiltonian as [48, 49]:

$$H = \sum_i \frac{P_i^2}{2M} + \sum_j \frac{p_j^2}{2m} + \frac{(Ze)^2}{2} \sum_{i,i'} \frac{1}{|R_i - R_{i'}|} + \frac{e^2}{2} \sum_{j,j'} \frac{1}{|r_j - r_{j'}|} - Ze^2 \sum_{i,j} \frac{1}{|r_j - R_i|}, \quad (2.12)$$

where M is the mass of the ion, m is the mass of the electron, and R_i (r_j) and P_i (p_j), respectively, is the position and momentum of the ith (jth) ion (electron). The first term is the sum of the kinetic energy of the ions ($T_{\rm i}$), the second term is the sum of the kinetic energy of the electrons ($T_{\rm e}$), the third term is the sum of interaction between the ions ($V_{\rm ii}$), the fourth term is the sum of interaction between electrons ($V_{\rm ee}$), and the last term is the sum of the interaction between the ions and the electrons ($V_{\rm ie}$). Here, we ignore the effect of spin-orbit coupling, Zeeman effect, and the Stark effect. From quantum mechanics, we learn that even for a single particle system, only a few examples are available that can be solved exactly. Therefore, solving Eq. (2.12) is hopeless without making good assumptions and dramatic simplifications.

To simplify Eq. (2.12), we use the Born-Oppenheimer approximation [50]. That is, we assume that the ions move much less compared to the conduction electrons. Then, the dynamics of the ions and electrons are on different energy scales, and we can separate the two. Let us separate the wave function for the Hamiltonian of Eq. (2.12) into two pieces:

$$\Psi(r, R) = \sum_n \Phi_n(R)\psi_n(r, R), \quad (2.13)$$

where n is the index of the energy eigenvalues (later band indices). When this wave function is acted on the Hamiltonian, the Born-oppenheimer approximation allows us to regard $\psi_n(r, R)$ as the solution for the electron wave functions in the presence of ions at position R:

$$(T_{\rm e} + V_{\rm ee} + V_{\rm ie})\psi_n(r, R) = E_n(R)\psi_n(r, R), \quad (2.14)$$

and $\Phi_n(R)$ as the wave function for the ions at position R:

$$(T_{\mathrm{i}} + V_{\mathrm{ii}} + E_n(R))\Phi_n(R) = \xi_n \Phi_n(R), \tag{2.15}$$

where ξ_n is the modes for phonons.

In our studies, we are more interested in Eq. (2.14), which describes electrons. Even Eq. (2.14) is too difficult to solve in general if we do not make any further simplifications. What makes this equation particularly difficult to solve is the presence of the electron-electron interactions (V_{ee})[2].

Let us keep simplifying the Hamiltonian by only considering a weakly correlated material case (week e-e interactions). Notice that each term on the left-hand side of Eq. (2.14) is a sum of j (jth electron).

$$T_e + V_{ee} + V_{ie} = \sum_j (t_{e,j} + v_{ee,j} + v_{ie,j}) = \sum_j h_j, \tag{2.16}$$

By boldly ignoring $v_{\mathrm{ee,j}}$ or treating it as a constant (an average field created by the other electrons that the electron feels) [49], and solving $h_j = t_{e,j} + v_{ee,j} + v_{ie,j}$ instead of Eq. (2.12), we have simplified the problem into an independent single-electron problem.

We can further work with h_j using Bloch′s theorem. Since we have assumed that the ions do not move greatly in position compared to the electrons, we can regard that the ions are positioned periodically, say with a lattice constant of a. Then the electron feels a periodic (ion) potential,

$$v_{ie,j}(r) = v_{ie,j}(r + a), \tag{2.17}$$

Bloch's theorem states that the wave function of an electron can be expressed in the following form [1, 49, 51]:

$$\psi_n(r) = \sum_k u_{n,k} \exp(ikr), \tag{2.18}$$

where $u_{n,k}(r)$ is a periodic function that satisfies $u_{n,k}(r) = u_{n,k}(r + a)$, k is the crystal momentum that is the momentum modulo the reciprocal lattice (e.g., $2\pi/a$ in 1D). As a result, the energy eigenvalue of an electron is parameterized by k, i.e., $E_n(k)$. And because of the periodicity of the lattice, the crystal momentum is bound to a certain range, called the Brillouin zone (BZ) (e.g., $-\pi/a \leq k \leq +\pi/a$ in 1D).

Furthermore, Eq. (2.16) can be solved approximately in different ways, which will not be discussed in this dissertation. The simplest one is the nearly free electron model, which

[2]This contribution is significant for considering the bulk of SmB_6. Of course, this is one of the many factors that make SmB_6 difficult.

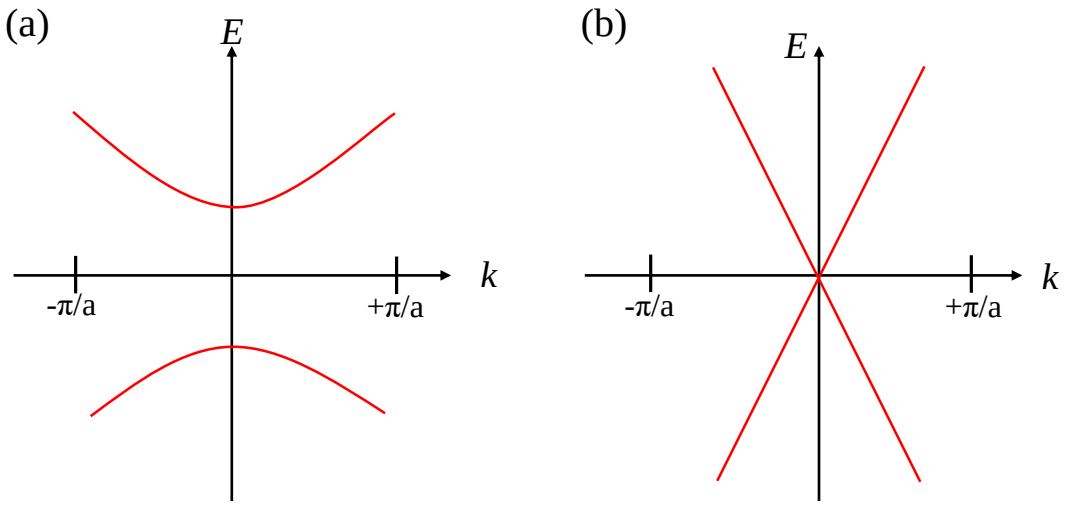

Figure 2.2: Example of bands. (a) Example of parabolic bands. (b) Example of linear bands.

starts with a plane wave and uses the time-independent perturbation theory by adding a weak periodic potential of the ions. Another one is the tight binding model, which assumes that the potential of the ions is strong. The model starts with a wave function that is superimposed with atomic orbitals and allows hopping to the neighboring atoms [52]. In both models, the lesson is that, in the BZ, there are bands of allowed energies that the electrons can occupy, and there is a forbidden gap between two bands, where there are no available states to be occupied. An example of energy vs. crystal momentum (E-k) diagram showing two such bands in the BZ is shown in Fig. (2.2) (a).

Another important feature is that the bands can be approximated as a parabola (quadratic k-dependence). Therefore, we can approximate the band into a form of kinetic energy: $E = \hbar^2 k^2 / 2m^*$, where m^* is the effective mass defined by:

$$\frac{1}{m^*} = \frac{1}{\hbar^2} \frac{\partial^2 E}{\partial k^2}. \tag{2.19}$$

Note that for the top band, $m^* > 0$, and for the bottom band, $m^* < 0$. These are the effective masses for electrons and holes, respectively.

Another example of a band in the E-k diagram is shown in Fig. (2.2) (b). The dispersion relation, in this case, is linear and the two bands touch at one point (called the Dirac point). This dispersion is important because it appears in graphene and on the surface of 3D topological insulators. Here, the bands can be approximated by a form of the massless Dirac equation, where instead of the speed of light we use the Fermi velocity, v_F, $E = \hbar v_F k$ (Dirac

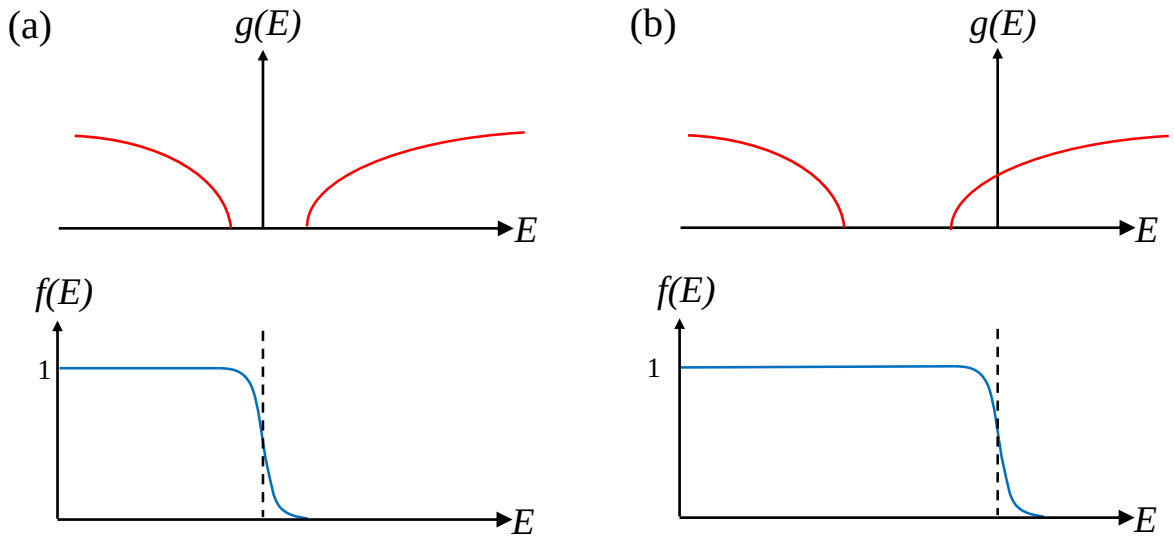

Figure 2.3: Example of density states of an insulator and a metal. (a) Example of the density of states of an insulator (top) and the Fermi-Dirac distribution (bottom) at finite temperatures. (b) Example of the density of states of a metal (top) and the Fermi-Dirac distribution (bottom) at finite temperatures.

dispersion). Because the band is linear, we cannot define the effective mass like Eq. (2.19). For a linear dispersion, the effective mass is typically defined as [53]:

$$\frac{1}{m^*} = \frac{1}{\hbar^2 k}\frac{\partial E}{\partial k}. \tag{2.20}$$

If the crystal momentum dependence is not of interest, and we only need to know the states at a given energy, the density of (energy) states is useful. From the band dispersions at a fixed energy, we can integrate over all k in the BZ to calculate the (total) density of states (in units of energy per unit volume):

$$g(E) = s\sum_n \int \frac{d^d k}{(2\pi)^d}\delta(E - E_n(k)), \tag{2.21}$$

where d is the dimension of the system (e.g, $d = 3$ for bulk and $d = 2$ for 2DEG) and s is the degeneracy of states by spins. $s = 2$ for normal materials where two opposite spins can occupy a state, whereas $s = 1$ for a 3D TI surface for the spins are split in opposite k-directions. The $1/(2\pi)^d$ comes from the periodic boundary condition (Born-von Karman boundary condition) of the wave function to describe a very large system (not the periodic

boundary condition of v_{ie}). Examples of density of states are shown in Fig. (2.3).

From bands, we know where the states can be occupied and where they cannot. Now we must know in what order they are occupied. Since electrons are fermions, they will fill from the lowest state and fill up the energy states following the Fermi-Dirac (F-D) distribution:

$$f^0(E) = \frac{1}{1 + \exp((E - E_F)/k_B T)}, \tag{2.22}$$

where E_F is the Fermi energy[3]. Here, we used the symbol $f^0(E)$ instead of $f(E)$ to emphasize that the system is in equilibrium. Therefore, the electrons will fill up the energy states from low to high energy.

Now we must know how high of energy the states will be occupied. If a total of N particles is present in a crystal, we must have the following relation:

$$n = \frac{N}{V} = \int dE g(E) f^0, \tag{2.23}$$

where n is the carrier density of the material.

With the bands (or density of states) and the F-D distribution, we can distinguish between insulators and metals. As shown in Fig. (2.3) (a), if the Fermi energy is positioned in the forbidden energy gap, the material is called an insulator. As shown in Fig. (2.3) (b), if the Fermi energy crosses a band, as shown in Fig. (2.3) (b), we call this material a metal. By convention, we call the highest occupied band by F-D distribution the valence band and call the lowest unoccupied band or partially filled band the conduction band. In the following section, we go back to transport. Now we will use the semiclassical approach, where the electrons obey the band structure (or density of states) and F-D statistics.

2.5 Conductivity from Semiclassical Transport Theory

Now we come back to transport and continue our discussion of current density, J. We will treat the current density semiclassically, meaning that we will use the occupation of states in bands with the F-D distribution. Also, we will use the Boltzmann transport equation from statistical mechanics, which describes the statistics in nonequilibrium.

To treat transport semiclassically, we first need some modifications of $\vec{J} = ne\vec{v}$ (Eq. (2.7), where we have treated all the electrons to move with the same velocity. A more reasonable definition of J is treating it as a flux density of charged particles with a statistical distribution

[3]Strictly speaking, it should be the chemical potential, and the Fermi energy is when T=0. We will use a more loose definition for simplicity.

of energy, $f(E)$:

$$\vec{J} = e \int dE g(E) f(E) \vec{v}(E). \tag{2.24}$$

Note that $f(E)$ is not the Fermi-Dirac distribution in equilibrium, but instead, it is the nonequilibrium distribution function when the system is perturbed by the electric field. To find $f(E)$, we use the Boltzmann transport equation [1,54]. The change in $f(E)$ by collisions, $(\partial f/\partial t)_{\text{coll}}$, includes the effect by perturbation from the external electric field:

$$\frac{\partial f}{\partial t} + \vec{v} \cdot \frac{\partial f}{\partial \vec{r}} - \frac{e\vec{\mathcal{E}}}{\hbar} \cdot \frac{\partial f}{\partial \vec{k}} = (\frac{\partial f}{\partial t})_{\text{coll}}, \tag{2.25}$$

where k is in the direction parallel to the applied electric field ($\mathcal{E}$) direction. On the left-hand side of Eq. (2.25), the first term is zero in DC transport because it is in steady state, and the second term also does not contribute when there is no spatial distribution. Next, we use the relaxation-time approximation to the first order of the Boltzmann equation:

$$(\frac{\partial f}{\partial t})_{\text{coll}} = -\frac{f - f^0}{\tau(E)}. \tag{2.26}$$

Then we can make the following approximation, which becomes a perturbed population from equilibrium [1,55,56]:

$$f \approx f^0 - \frac{e}{m}\tau(E)\frac{\partial f^0}{\partial v_x} \cdot \mathcal{E}_x = f^0 + \frac{e}{\hbar}\tau(E)(-\frac{\partial f^0}{\partial E})(\frac{\partial E(k)}{\partial k_x})\mathcal{E}_x, \tag{2.27}$$

where we have defined the x direction as the direction of the applied electric field. Therefore, the terms that involve the dot product with $\vec{\mathcal{E}}$ have a subscript of x. Also, v is the (group) velocity associated with the crystal momentum (k) direction.

Also, the relaxation time, τ, has a clear meaning. It is the scattering time of the electrons by some scattering potential. Formally, it is determined by [1]:

$$\frac{1}{\tau} = \int W(k, k')(1 - cos\theta_{k,k'})dk \tag{2.28}$$

where $W(k, k)$ is the scattering rate that depends on the scattering mechanism in the solid. To the first order, $W(k, k)$ is found by Fermi's golden rule, which is basically the time-dependent perturbation of the interaction term of the Hamiltonian. For example, for (dilute) impurities that are disordered in the crystal with a scattering potential, V_{imp}, the scattering rate is:

$$W(k, k') = \frac{2\pi}{\hbar} n_i \delta(E(k) - E(k'))| < k|V_{\text{imp}}|k' > |^2 \tag{2.29}$$

where n_i is the density of the impurities.

Since we have found f in Eq. (2.27), we insert it in Eq. (2.24). The first order term, which corresponds to the system at equilibrium, from the expansion in Eq. (2.27) does not contribute to current. The second term contributes to the current density, and we have:

$$J_x = \frac{e^2\mathcal{E}_x}{\hbar^2}\int dEg(E)\tau(E)(\frac{\partial E(k)}{\partial k_x})^2(-\frac{\partial f^0}{\partial E}). \tag{2.30}$$

Again, this is consistent with Ohm′s law (Eq. (2.3)) since $\vec{J}$ is proportional to $\vec{\mathcal{E}}$. We can further simplify Eq. (2.30) by making more assumptions. First, we assume that the equipartition theorem holds for the kinetic energy, just like for a free electron gas: $< v_x^2 >= 1/d < v^2 >$, where v_x is the velocity in the same direction as the electric field, v is the total velocity in all directions, and d is the dimension of the system. Also, we assume that τ is independent of energy. Then, the conductivity is:

$$\sigma = \frac{e^2\tau}{d}\int dEg(E)v^2(-\frac{\partial f^0}{\partial E}). \tag{2.31}$$

Now we have a conductivity that depends on the $g(E)$ of a solid (or roughly speaking, integrating the bands for each k at a given E), and the temperature dependence of the statistics contained in f^0.

With Eq. (2.31) derived from the semiclassical transport theory, let us examine the conductivity of metals and insulators we have defined in the previous section. Remember, we have defined them using band theory of solids, that a material is a metal if the Fermi energy crosses a band, and the material is an insulator if the Fermi energy is positioned within the forbidden gap (See Fig. (2.3) for example).

Let us consider a metal first. In Eq. (2.31), it involves $(-\frac{\partial f^0}{\partial E})$ inside the integral. This is a sharply peaked function at sufficiently low temperatures. Therefore, we can assume $(-\frac{\partial f^0}{\partial E}) \approx \delta(E - E_F)$ at low temperatures. Then, Eq. (2.31) is:

$$\sigma \approx \frac{e^2\tau}{d}\int dEg(E)v^2\delta(E - E_F) = \frac{v_F^2\tau}{d}e^2g_c(E_F). \tag{2.32}$$

where v_F is the Fermi velocity, and $g_c(E_F)$ is the density of states of the conduction band, specifically at the Fermi energy. Eq. (2.32) is known as the Einstein relation of conductivity.

We note that from Eq. (2.32), we do not need to completely abandon the Drude model if we interpret the carrier density and mobility properly. Comparing Eq. (2.32) to the conductivity from the Drude model (Eq. (2.11), the carrier density $n = \frac{2}{d}E_Fg(E_F)$, where we have used $E_F = 1/2m^*v_F^2$. We have shown that only the states in the vicinity of the Fermi

energy participate in carrier transport. Typically, for a metal, the temperature dependence of the carrier density is weak. Usually, the temperature dependence of the conductivity in a metal is mostly from the temperature dependence of the scattering time, τ.

Now let us consider the case of an insulator where the Fermi energy lies within the forbidden gap. For an insulator, there are no states available at the Fermi energy, $g(E_F) = 0$, so the approximation of conductivity in Eq. (2.32) results in zero conductivity for an insulator. This is, in fact, true when the temperature is at $T = 0$ K. At temperatures slightly above 0 K, there are higher order contributions from the tail of the F-D distribution. As a result, the bands that are near the Fermi energy (conduction and valence band) contribute. The following relation is useful to see this [56]:

$$-\frac{\partial f^0}{\partial E} = \frac{1}{k_B T} f^0(1 - f^0). \tag{2.33}$$

Then, Eq. (2.31) for an insulator becomes:

$$\sigma = \frac{e^2}{dk_B T} \int dE v^2 f^0(1 - f^0) g(E). \tag{2.34}$$

Remember, from the definition of density of states (Eq. (2.21)), the density of states sums all the nth bands ($g(E) = \sum_n g_n(E)$). When considering the conduction band, the lowest band above the Fermi energy, Eq. (2.33) can be approximated as, $f^0(1 - f^0) \approx \exp(-(E - E_F))/k_B T$). When considering the valence band, the highest band below the Fermi energy, Eq. (2.33) can be approximated as, $f^0(1 - f^0) \approx \exp(-(E_F - E))/k_B T$). The contribution of the rest of the bands is much smaller, so it can be neglected. Then Eq. (2.34) is:

$$\sigma \approx \frac{e^2}{dk_B T}\left(\int dE\ v_c^2 \tau_c \exp(-(E - E_F)) g_c(E) + \int dE\ v_v^2 \tau_v \exp(-(E_F - E)) g_v(E)\right), \tag{2.35}$$

where g_c is the density of states from the conduction band and g_v is the density of states from the valence band. This is the conductivity of an insulator in which the first term is generally regarded as electrons and the second term as holes. Since the velocity is related to the slope of the band, the conduction band (v_c) and valence band (v_v) must have different velocities. Also, in general, the scattering time associated with the conduction band (τ_c) and the valence band (τ_v) are different. From Eq. (2.35), we learn that although there are no states available near the Fermi energy, the tail of the Fermi energy at finite temperatures reaches to the nearby bands and contributes to transport.

We can also reinterpret the Drude conductivity for an insulator. To do this, we continue working with Eq. (2.35) a little further. First, we consider the contribution of the conduction

band, which is the first term on the left side of Eq. (2.35). Since the statistical average of v^2 can be estimated as[4]

$$< v >^2 = \frac{\int dE\ g(E)v^2 \exp(-(E-E_F)/k_BT)}{n} \approx \frac{k_BT}{m^*}, \tag{2.36}$$

we therefore can express the conductivity from the conduction band into the Drude conductivity form, $\sigma = ne^2\tau/m$, where [1]

$$n = \int dE\ g_c(E) \exp(-\frac{(E-E_F)}{k_BT}) = n_0 \exp(-\frac{(E_c-E_F)}{k_BT}), \tag{2.37}$$

and

$$n_0 = \int_{E_c}^{\infty} dE g_c(E) \exp(-\frac{(E-E_c)}{k_BT}). \tag{2.38}$$

Here, E_c is the bottom of the conduction band. n is the carrier density of electrons. The energy difference between the conduction band the Fermi energy is often called the activation energy, $E_a = E_c - E_F$. Similarly, when we consider the valence band, we have the carrier density of holes:

$$p = \int dE\ g_v(E) \exp(-\frac{(E_F-E)}{k_BT}) = p_0] \exp(-\frac{(E_F-E_v)}{k_BT}), \tag{2.39}$$

and

$$p_0 = \int_{-\infty}^{E_v} dE g_v(E) \exp(-\frac{(E_v-E)}{k_BT}), \tag{2.40}$$

where E_v is the top of the valence band.

If we assume that either the electrons or holes dominate the conductivity, we can see that the temperature dependence of the resistance is exponential, $R \propto 1/\sigma \propto \exp(E_a/k_BT)$.

In this section, we have found the conductivity from a semiclassical approach. One important lesson we have learned from this section is that we do not fully have to abandon the Drude formalism as long as we interpret the carrier density and mobility correctly. For a metal, the carrier density is interpreted as the sum of the occupied electron states near the Fermi energy. For an insulator, although there are no states available at the Fermi energy, the carrier density is determined by the contribution of the F-D distribution tail reaching the conduction band and the valence band. This explains why in transport, we have a temperature dependence of $\sigma \propto \exp(-E_a/T)$. For the mobility, $e\tau/m$, we replace m to m^*.

[4]There are two alternative ways to treat this equation. One is using a known density of states and doing an honest integral. However, this would not be general. Another is using the Einstein relation. But we try to not introduce additional material for simplicity.

We note that the sign can be negative if we consider holes[5]. τ is related to the relaxation time that is related to the scattering potential of the disorder potential.

In the following section, we will discuss how to separately determine the carrier density and mobility by applying magnetic fields.

2.6 Magnetotransport: Determining the Carrier Density and Mobility

By just finding the conductivity from measuring the resistance, we only know the product of the carrier density and mobility, and do not know their values individually. The carrier density and mobility can be separately determined by performing measurements in a magnetic field. To see how this magnetotransport works, we add the Lorentz force to the equation of motion in the steady state of Eq. (2.8) [1]:

$$0 = e(\vec{\mathcal{E}} \ + \ \vec{v} \times \vec{B}) \ - \ \frac{m^* \vec{v}}{\tau}, \tag{2.41}$$

Since the dissertation will only focus on the surface magnetotransport, we consider only the 2D case when the magnetic field is applied in the out-of-plane direction (z-direction). After we multiply $ne\tau/m^*$ with Eq. (2.41), and separate the vector components in the x and y direction, we have the following relations [1]:

$$\begin{aligned} (ne\mu)\mathcal{E}_x &= \mu B J_y \ + \ J_x, \\ (ne\mu)\mathcal{E}_y &= -\mu B J_x \ + \ J_y, \end{aligned} \tag{2.42}$$

We can change this into a matrix form after re-arranging:

$$\vec{J} = \frac{ne\mu}{1 + (\mu B)^2} \begin{pmatrix} 1 & \mu B \\ -\mu B & 1 \end{pmatrix} \vec{\mathcal{E}} \tag{2.43}$$

Therefore, in the presence of a perpendicular magnetic field, we can treat the conductivity as a tensor:

$$\sigma(B)_{xy} = \frac{ne\mu}{1 + (\mu B)^2} \begin{pmatrix} 1 & \mu B \\ -\mu B & 1 \end{pmatrix} \tag{2.44}$$

We note that this form can be particularly useful for numerical calculations. For example, numerical methods such as finite element analysis can solve the Laplace equation ($\nabla^2 V =$

[5] Alternatively, we can encode the sign of electrons and holes in the charge [52].

0) with the appropriate boundary conditions to solve for the potential and electric field throughout the geometry. Then, the current density can be found by multiplying the electric field vector with Eq. (2.44) without any further complications.

Next, we consider two examples in this section using Eq. (2.43): a sheet geometry and a Corbino disk geometry, as shown in Fig. (2.1) (b) and Fig. (2.1) (c), respectively. First for a sheet geometry, if we send current in the x-direction (through L), and measure the voltage vertically in the y-direction that is sufficiently far away from the current sources, we have $J_y = 0$, so that the current only flows in the x-direction. Applying this condition to Eq. (2.43), we find the Hall resistance[6]

$$R_{\text{Hall}} = \frac{V_y}{I_x} = \frac{\mathcal{E}_y W}{J_x W} = -\frac{B}{ne}. \tag{2.45}$$

Therefore, by measuring the Hall resistance, R_{Hall}, the carrier density can be estimated. Also, R_{Hall} depends on the sign of the carriers, so that we can also distinguish between electrons and holes. We note that the $J_y = 0$ condition must be strictly satisfied. If the Hall effect is measured on the surface of a thick a 3D TI with a slab geometry, satisfying $J_y = 0$ is difficult in practice because current can flow on all six surfaces. We later discuss in Chapter 3 that the Hall bar configuration for characterizing the surface of SmB_6 may cause incorrect estimations of the carrier density.

We next consider a Corbino disk both analytically and numerically. Because the annular region of the Corbino disk requires the equipotential to be circular by symmetry, this requires the electric field to be only in the radial direction ($\mathcal{E}_r$). Then, it is convenient to express the x and y components of $\mathcal{E}$ in terms of $\mathcal{E}_r$ by choosing the polar coordinates, (r, ϕ):

$$\begin{aligned} \mathcal{E}_x &= \mathcal{E}_r \cos\phi, \\ \mathcal{E}_y &= \mathcal{E}_r \sin\phi, \end{aligned} \tag{2.46}$$

Then, inserting Eq. (2.46) into Eq. (2.43), the current density becomes:

$$\vec{J} = \frac{ne\mu}{1 + (\mu B)^2} \begin{pmatrix} 1 & \mu B \\ -\mu B & 1 \end{pmatrix} \begin{pmatrix} \cos\phi\ \hat{x} \\ \sin\phi\ \hat{y} \end{pmatrix} \mathcal{E}_r. \tag{2.47}$$

We can calculate the current by integrating over a closed circle (red-dotted circle in Fig. (2.1) (c))

[6]Note that we distinguish R_{Hall} from R_H. R_H is the hybrid resistance, which will be introduced in Chapter 4.

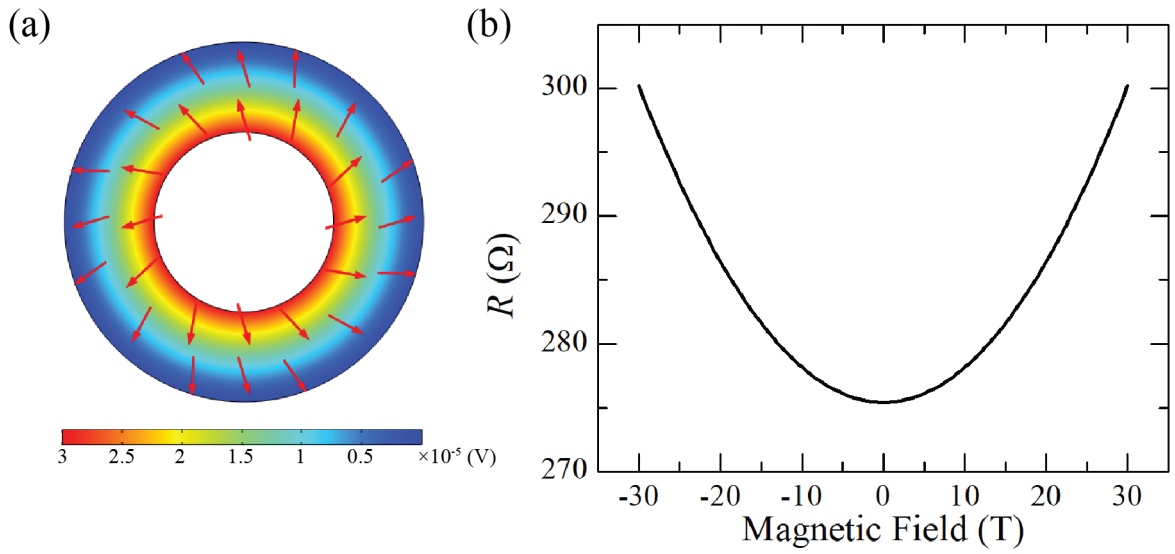

Figure 2.4: Numerical simulation results of a Corbino disk in the presence of the out-of-plane magnetic field. A commercial finite element analysis software (Comsol Multiphysics AC/DC module) is used for the simulations. The surface is set to μ=100 (cm^2/(V$\cdot$s)), n=2.5 $\times$ 10^{13} (1/cm^2). The applied current is set to I=10^{-6} (A). (a) Equipotential (in gradient color) and current (in red arrows) results at 30 T. (b) Simulated Resistance vs. Magnetic field of the Corbino from -30 T to +30 T.

somewhere in the annulus:

$$I = \oint \vec{J} \cdot d\vec{l} = \frac{ne\mu}{1+(\mu B)^2}(2\pi r \mathcal{E}_r). \tag{2.48}$$

We then integrate from the inner radius, r_{in}, to the outer radius, r_{out}, to calculate the potential difference (voltage). Then, the resistance of a Corbino disk in the presence of the magnetic field is:

$$R_{\text{Corbino}} = \frac{\ln(r_{\text{out}}/r_{\text{in}})}{2\pi}\frac{1+(\mu B)^2}{ne\mu}. \tag{2.49}$$

Notice that the resistance in Eq. (2.49) has a $1+\mu^2B^2$ factor. The resistance has a quadratic magnetic field dependence because of this factor.

As an instructive exercise, we also use Eq. (2.44) as the anisotropic conductivity tensor and simulate the Corbino disk numerically. The result of the potential distribution and the current density direction is shown in in Fig. (2.4) (a). Here, the equipotential lines are circular, consistent with Eq. (2.5), while the current direction spirals consistent with Eq. (2.47).

A simulated magnetic field sweep is shown in Fig. (2.4) (b). As we expect from Eq. (2.49), the numerical results also show a quadratic dependence that is consistent with the $1+\mu^2B^2$

factor. This extra quadratic-magnetic-field dependence factor in resistance allows us to find the mobility. From this mobility and the conductivity at zero magnetic field, we can also find the carrier density. Note that in the Corbino disk configuration, the sign of the carrier does not influence the resistance. In Chapter 3, we will go into more detail about using the Corbino disk to study the surface of SmB_6.

2.7 Shubnikov de-Haas Oscillations: Finding the Carrier Density and Mobility from Landau Levels

In the previous section, we have shown that the carrier density and mobility can be found when applying the magnetic field using the classical Drude formalism. In addition to this effect, there is a quantum mechanical effect that can be used to find the carrier density and mobility. When the magnetic field is strong enough, the density of states is quantized into discrete levels, called Landau levels, and they can be used to find the carrier density and mobility. This effect is called Shubnikov de-Haas (SdH) oscillations.

For a two-dimensional electron gas (2DEG) without any interactions, the Landau levels can be understood easily. In the Hamiltonian for a free electron, if we modify the momentum operator that includes minimal coupling, $\hat{p} \to \hat{p} + e\vec{A}$, and choose the Landau gauge for the vector potential, $\vec{A} = (0, Bx, 0)$. The eigenvalue solution becomes similar to the simple harmonic oscillation problem:

$$E_n = \hbar\omega_c(n + 1/2), \tag{2.50}$$

where ω_c is the cyclotron frequency defined as eB/m^*. Therefore, the energies are discretized with an energy width of $\hbar\omega_c$, which becomes wider at higher magnetic fields. This idea can be applied to a 2DEG that has very small v_{ee} (electron-electron interactions).

The Landau levels are manifested in conductivity with an oscillating behavior. Unfortunately, the semiclassical approach that we have used for understanding conductivity for metals and insulators is not suitable for explaining the quantum oscillation phenomena in conductivity. Still, by making a brave assumption, we will eventually arrive to the Lifshitz-Kosevich formula, which describes not only the oscillating behavior of conductivity but also the damping of the oscillations[7].

Inspired by the Boltzmann transport, which we have worked with so far, we assume that the conductivity is related to the density of states. The density of states are quantized into Landau levels. We assume that the conductivity is proportional to the sum of density of

[7]Most derivations found from textbooks require additional knowledge that is not covered in this chapter. But by accepting a simple assumption, the derivation works amazingly well.

states only near the Fermi energy with a thermal broadening ($\delta \approx -\frac{\partial f^0}{\partial E} dE$).

$$\sigma \propto \sum_{E_F-\delta/2}^{E_F+\delta/2} \mathrm{g(E)} \rightarrow \int g(E)(-\frac{\partial f^0}{\partial E})dE. \tag{2.51}$$

Note that this does not necessarily mean that the integral above is the carrier density that is associated with the drift caused by the electric field in the Boltzmann equation[8].

Now, let us construct the density of states. Without broadening of the Landau levels by disorder, we can use Eq. (2.21) with the Landau levels, Eq. (2.50). The density of states can be regarded as delta functions peaked at the eigenvalue of energies (Landau level peaks):

$$g(E) = C \sum_n \delta(E - (n + \frac{1}{2})\hbar\omega_c), \tag{2.52}$$

where we defined a constant, C, that absorbs all the constants that do not contribute in the rest of the calculation. We can express this density of states in a series of integers, p:

$$g(E) = \frac{C}{\hbar\omega_c}[1 + 2\sum_{p=1}^{\infty} \cos(2\pi(\frac{E}{\hbar\omega_c} - 1/2)p)], \tag{2.53}$$

where we have used the Poisson formula:

$$\sum_{n=-\infty}^{\infty} h(n+\phi) = \sum_p e^{2\pi i p\phi} \int_{-\infty}^{\infty} h(y) e^{2\pi i p y} dy. \tag{2.54}$$

Note that from changing Eq. (2.52) to Eq. (2.53), we have now expressed the density of states of Landau levels that results in a sum of oscillating terms (cosine terms).

Now we include the broadening of the peaks due to disorder. We assume the broadened peak is a Lorentzian shape associated with a (quantum) scattering time, τ_Q. Then, we use the convolution integral to modify the delta peaks to Lorentzian peaks to find the correction to density of states due to disorder broadening, g_d [58]:

$$\begin{aligned} g_d(E) &= \int_0^{\infty} g(E') \frac{\hbar/2\tau_Q}{(E-E')^2 + (\hbar/2\tau_Q)^2} dE' \\ &= \frac{C}{\hbar\omega_c}[1 + 2\sum_{p=1}^{\infty} e^{-\pi/\omega_c\tau_Q} \cos[2\pi(\frac{E}{\hbar\omega_c} - 1/2)p]], \end{aligned} \tag{2.55}$$

[8]Pippard, in his book, does a somewhat similar approach and discusses in greater detail. According to this interpretation, the integral in Eq. (2.51) is related to the scattering rate [57].

Inserting Eq. (2.55) into Eq. (2.51), the conductivity can be expressed as:

$$\sigma = \frac{C}{\hbar\omega_c}[1 + 2\sum_{p=1}^{\infty} e^{-\pi/\omega_c\tau_Q} \frac{(\frac{2\pi^2 k_B T}{\hbar\omega_c})p}{\sinh[(\frac{2\pi^2 k_B T}{\hbar\omega_c})p]} \cos[2\pi(\frac{E}{\hbar\omega_c} - 1/2)p], \tag{2.56}$$

where we have used the following integrals:

$$\begin{aligned} \int_{-\infty}^{+\infty} (-\frac{\partial f^0}{\partial E}) dE &= 1, \\ \int_{-\infty}^{+\infty} (-\frac{\partial f^0}{\partial E}) \cos(E/E_0) dE &= \frac{\pi k_B T/E_0}{\sinh(\pi k_B T/E_0)} \cos(E/E_0) \end{aligned} \tag{2.57}$$

Conveniently, we define the temperature damping factor, D_T, and the Dingle damping factor, D_D:

$$\begin{aligned} D_T &= \frac{\frac{2\pi^2 k_B T}{\hbar\omega_c}}{\sinh[\frac{2\pi^2 k_B T}{\hbar\omega_c}]}, \\ D_D &= \exp(-\frac{\pi}{\omega_c\tau_Q}) = \exp(-\frac{\pi}{\mu_Q B}). \end{aligned} \tag{2.58}$$

Keeping only $p = 1$ in Eq. (2.56), which is the dominating term, we express the magneto-conductivity as:

$$\frac{\Delta\sigma(B)}{\sigma(B=0)} = D_T D_D \cos[2\pi(\frac{E_F}{\hbar\omega_c} - \frac{1}{2})]. \tag{2.59}$$

Alternatively, we can write:

$$\frac{\Delta\sigma(B)}{\sigma(B=0)} = D_T D_D \cos[2\pi(\frac{F}{B} - \frac{1}{2})]. \tag{2.60}$$

where F is the frequency that oscillates with

$$F = \frac{\hbar}{2\pi e}(\pi k_F^2) = \frac{\hbar}{2\pi e} A_{FS}, \tag{2.61}$$

where A_{FS} is the area of the Fermi surface, which is πk_F^2 if a perfect circle. Eq. (2.61) is the Onsager relation.

Therefore, we see that if quantum oscillations are observed from applying a magnetic field, we can find the area of the Fermi surface from the frequency. In k space, there are a density of $sV^d/(2\pi)^d$ carriers since we are using the Born von-Karman boundary conditions [1] for the wave function. The total number of carriers is then $N = sV^d/(2\pi)^d \times A_{FS}$. In 2D, $d = 2$, and the V is the area, and thus the relation between the carrier density and the Fermi

surface area is:

$$n_{2D} = \frac{N}{\text{Area}} = \frac{s}{(2\pi)^2} A_{\text{FS}}. \tag{2.62}$$

From the magnetic field dependence at a fixed temperature, μ_Q can be found from D_D. If necessary, m^* can be found by the temperature dependence of the amplitude at a fixed magnetic field. Note that the quantum mobility, μ_Q, is not necessarily the same as the mobility that we find from classical transport.

2.8 Summary

In this chapter, we have briefly reviewed transport theory. An introduction to the classical and semiclassical transport theory was introduced to understand conductivity of a material. An introduction of band theory and its connection to transport was also reviewed. The role of magnetic field in classical transport and SdH quantum oscillations was introduced. In the following chapters, the actual experimental work on transport measurement of SmB_6 will be presented.

Chapter 3

Surface Studies of SmB_6: Cornering the Transport Parameter Space

3.1 Introduction

[1]Two years after the first prediction that SmB_6 is a topological Kondo insulator [41], Ç. Kurdak's group [40] from the University of Michigan and J. Xia's [59] group from the University of California-Irvine verified that the surface conduction is responsible for the resistance plateau below 3 – 4 K using electrical transport. The origin of this plateau has been a 40-year-old mystery, and finally, the topological insulator hypothesis together with the transport experiments offered a compelling explanation.

The next job for the researchers is to examine the properties of this surface conductor. This investigation is important for the following reasons. First, we must make sure that this surface conduction originates from the nontrivial topological nature of the bulk states. Second, if this surface is a two-dimensional electron gas system (2DEG), we must report what is different compared to other 2DEGs or the surface of 3D TIs. Third, we must quantify the quality of this 2DEG.

From an electrical transport perspective, the most powerful way to investigate the surface property is through Shubnikov de-Haas (SdH) quantum oscillations. SdH oscillations provide very accurate information about the Fermi surface. First, from the oscillation frequency, the area of the Fermi surface(s) can be estimated. Second, the magnetic-field-angle dependence of the oscillation frequency can distinguish if the Fermi surface is from the surface or bulk of the sample. If the origin of the oscillations is from the surface of the sample (2DEG), then the amplitude of the oscillations should be proportional to the inverse of the cosine

[1]The author and his collaborators are preparing a manuscript for submitting to a peer-reviewed journal that will contain contents in this chapter.

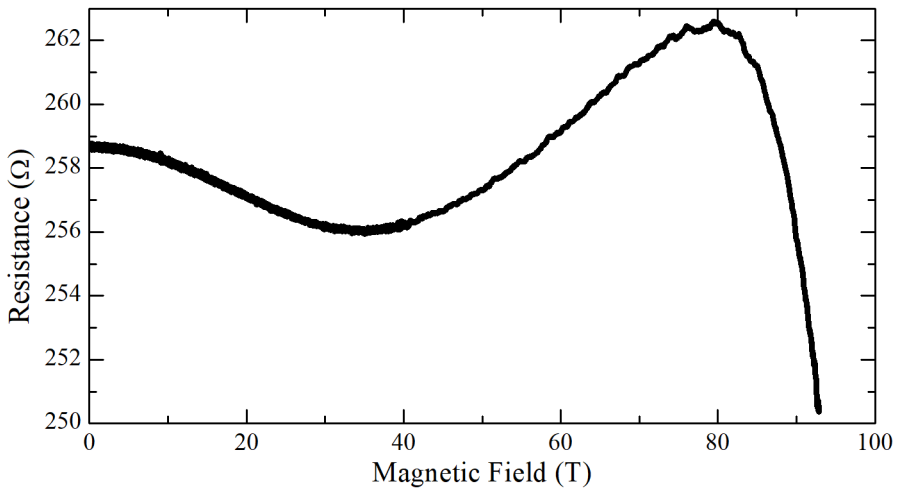

Figure 3.1: Absence of Shubnikov de-Haas oscillations in SmB_6 up to 93 T. Magnetotransport was measured using a Corbino disk on the (001) surface. The magnetic field was applied by a pulse field at the National Magnetic Field Laboratory at Los Alamos up to 93 T at 1.4 K. The negative magnetoresistance above 80 T is believed to be the surface-to-bulk crossover behavior at high fields. Figure courtesy of S. Wolgast.

angle. Third, by analyzing the damping of the oscillation amplitude, the scattering time and effective mass, and hence the mobility can be found. Lastly, in the Landau level index vs. inverse magnetic field plot (Landau fan diagram), if the linear connection of the Landau indices is extrapolated to the infinite magnetic field limit ($1/B \rightarrow 0$), the Berry phase can be found from the intercept. This Berry phase can be used to verify that the energy dispersion is Dirac-like. However, quantum oscillations in transport has not been observed to date. In 2013, in collaboration with L. Li's group, we tried to observe SdH while sweeping the magnetic field up to 45 T [60]. Later in 2015, from a study from our group, Wolgast *et al.* subsequently studied with a pulsed field magnet even up to 93 T, as shown in Fig. (3.1), and still failed to observe SdH oscillations.

Five years have passed since the two seminal reports by S. Wolgast *et al.* and D. J. Kim *et al.*, and many experimental reports on SmB_6 have been published. Many of the reports are exciting, but the situation, in whole, is problematic because many of them do not agree with each other. Unlike SdH oscillations, dHvA quantum oscillations have been observed, with an oscillation onset of ∼5 T, by G. Li *et al.* (L. Li's group), using a magneto-torque technique [60]. In this dHvA report, they see signatures of the 2D Fermi surface that is consistent with the 3D TI picture: the field-angle-dependence of the oscillation frequency has an inverse cosine angle dependence, three Fermi-pockets, and a half integer from the extrapolation of the Landau fan diagram to the infinite magnetic field limit. This is an exciting result in that

it verifies the 3D TI picture. However, it raises a mystery why quantum oscillations from magneto-torque (dHvA) can be seen, whereas quantum oscillations from magnetotransport (SdH) cannot. The reason for SdH and dHvA to exhibit quantum oscillations is because both conductivity and magnetization are both functions of the density of states that become quantized by Landau levels at high magnetic fields. Therefore, in principle, they should not be fundamentally different. Furthermore, about two years after the dHvA quantum oscillation report by G. Li *et al.* [60], the 2D Fermi surface picture has been challenged by Tan *et al.* [61] from the University of Cambridge. This group studied magnetization on two SmB_6 samples that were grown by the floating zone method, and they report that their dHvA quantum oscillations come from an exotic bulk state instead of the surface. First, Tan *et al.* observe quantum oscillations with a field-angle-dependence that does not follow an inverse-cosine-angle behavior, but rather more of a bulk Fermi surface behavior. In addition to the similar low-frequency oscillations that G. Li *et al.* observed, they observe high-frequency oscillations that G. Li *et al.* did not report. The Landau fan diagram extrapolates to an integer, which implies that the frequencies are not from a topological origin. Most surprisingly, they observe a temperature dependence that deviates from the typical Lifshitz-Kosevich damping factor. They also claim the high-frequency quantum oscillations cannot be coming from the surface based on the amplitude of their dHvA oscillations. They further supported this claim by looking at two samples with different crystalline surfaces.

In addition to transport and magneto-torque measurements, a large number of other experimental studies has been reported in this material system. Among these, recent high-resolution Angle-Resolved Photoemission Spectroscopy (ARPES) measurements have provided invaluable information about both bulk and surface states of SmB_6 [62–67]. From some of the studies, the three Fermi pockets that contribute to the surface states have been observed [64–66]. Even the helical spin structure, which is a unique surface TI property, has been claimed to be observed [67]. However, there are also some other ARPES reports that claim that the surface is from a trivial origin, and not from a topologically nontrivial origin [68, 69].

Returning to electrical transport, when we look at the 2D reports that are performed by many groups on SmB_6, we see a large variation of the quantitative values related to the 2D surface (2D resistance, carrier density, and mobility). This chapter is about understanding the reason for this large variation, and then finding the correct values (or the correct ranges). Only after finding the correct values, we can compare with other experimental reports such as ARPES and dHvA.

Because SdH oscillations cannot be observed in magnetotransport, researchers rely on the classical (Drude) transport to characterize the 2DEG of the SmB_6 surface. In principle,

the properties of the surface can still be found. For the early reports that used conventional transport methods, the large variation may be due to the following reasons. First, current flows on every surface (top, bottom, side surfaces, and even the edges) and an order-of-magnitude incorrect estimate of the sheet resistance can easily be made if the details of the surface geometry are not known accurately. It will be shown later in this chapter that even the simplest task of accurately measuring the 2D conductivity of this material turns out to be challenging. The sheet resistance is typically extracted from four-terminal resistance measurements performed on a Hall bar or a van der Pauw sample. The measured resistance and sheet resistance are proportional to a geometric factor (g) that is determined by the geometry of the sample. Unlike bulk materials or thin film topological insulators, knowing g is not a trivial task for SmB_6 unless the geometry is simplified. Second, the magnetoresistance can play a complicated role in a 3D TI surface. In addition to the complication of the current path, the complication from magnetoresistance can arise because the carriers on different surfaces experience a different Lorentz force. If the direction of the applied magnetic field is perpendicular to the top and bottom surface (out-of-plane direction), at the same time, this field direction is parallel to the side surfaces (in-plane direction). Also, a theoretical report discusses the possibility of electrons and hole pockets both existing on the surface Brillouin zone [70]. This raises the possibility that the Hall coefficient can further overestimate the carrier density when the species are not identified correctly. Therefore, we must choose a transport geometry that is free from these complications.

To this end, we study magnetotransport on a Corbino disk fabricated on a SmB_6 surface. The Corbino disk allows us to confine the transport region to a single surface, and the sheet resistance can be found easily since g, which converts from resistance to sheet resistance, is well-known. By applying the magnetic field, the Corbino disk is immune to the sign of the carriers and the mobility and carrier density can be found.

Throughout years of studies, we find another possibility that can complicate the surface transport study. We find that subsurface cracks can also conduct as well as the exposed crystalline surface of SmB_6. This implies that surface preparation such as thinning and polishing is extremely important. For example, rough polishing can create subsurface cracks and change g. Similarly, it is also possible that even small grain boundaries on the surface can serve as extra conducting paths, and can further change g. After noticing the subsurface crack conduction possibility, we carefully screened and prepared our surfaces to minimize the effect of these cracks, and re-investigated our magnetotransport studies.

From our results, we find the carrier density and mobility of the surface, but we do not have enough resolution to distinguish the contribution from each of the Fermi pockets. Instead, from our effective carrier density and mobility, we construct a transport parameter

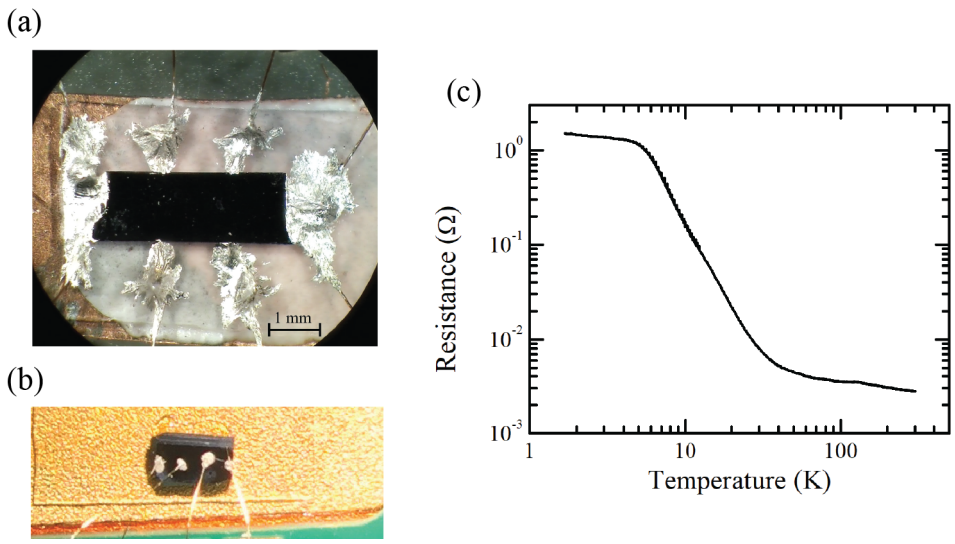

Figure 3.2: Incorrect transport geometries for measuring SmB_6. (a) Hall bar measurement on a polished SmB_6 sample with indium contacts. Reprinted figure with permission from [40], and also additional kind permission from the first author. Copyright (2013) by the American Physical Society. (b) Standard four-prong measurement on a raw disordered SmB_6 sample (9 % Sm-deficient). (c) Resistance vs. temperature measurement of the sample shown in (b).

space where each of those channels can be located. This parameter space allows us to compare with not only other transport reports but also with dHvA and ARPES reports. Our results are consistent with only the ARPES reports of the X-pocket.

3.2 Choosing the Improper Transport Geometry (Early Attempts)

In this section, we present some examples of our early transport experiments. In retrospect, the sheet resistance, surface carrier density, and mobility are wrong values. Nevertheless, we present them here because they provide a good lesson to understand how important it is to design the experiment properly.

Soon after the non-local transport was performed and the existence of the conducting surface was verified, Wolgast *et al.* performed magnetic field studies on a Hall bar sample, as shown in Fig. (3.2) (a). The sheet resistance was estimated as 9.1 Ω, and Hall coefficient is in the ∼10 – 4 Ω/T [40] range. A conversion to surface carrier density from this Hall coefficient results in the range of 10^{18} cm^{-2}. This is a very large carrier density that easily exceeds the highest known carrier densities of the 2DEG/thin film systems. For example, the oxide interface systems such as $GdTiO_3/SrTiO_3$ [71], which is known to have very high

carrier density, are reported in the low 10^{14} cm^{-2} range. We later show that this high carrier density estimation is not physical when we consider the area of the Brillouin zone.

Another instructive example that is shown in Fig. (3.2) (b) is the standard four-prong geometry, which many researchers use in their transport experiments. The resistance is typically measured by sending current from the two leads at the ends and measuring the voltage difference between the two leads. This is a standard method for bulk studies. When researchers perform use this method, since the geometric factor is complicated unless the sample is polished into a perfect slab shape, they avoid converting their resistance data to resistivity. Instead, they estimate the resistance ratio, which is the ratio of the resistivity at some temperature to the resistivity at room temperature. By taking the ratio of the resistances at the temperature and at 300 K, the geometric factor (g) is not involved, and therefore this ratio is the same as the resistivity ratio ($R(T)/R(300\text{K}) = \rho(T)/\ \rho(300\ \text{K})$). However, this does not work when a material allows the current to flow on the surface as well as the bulk. For SmB_6, the g at 300 K and temperatures below 3 – 4 K are not the same. For 300 K, the g is related to the bulk geometry, whereas at 0 K, g is related to the surface geometry. For the sample shown in Fig. (3.2) (b), the resistance vs. temperature is shown in Fig. (3.2) (c). Although we now know that the resistance plateau at temperatures below 4 K is from the surface, we do not know the geometric factor for converting the resistance to sheet resistance. Therefore, we must choose a simple transport geometry that allows us to easily predict how the current flows. In the following section, we introduce the Corbino disk geometry, which is eventually used for measuring the surface properties of SmB_6.

3.3 Choosing the Proper Geometry: Corbino Disk

In this section, we first introduce the Corbino disk geometry, including its magnetotransport, which we used in our SmB_6 transport studies. We then discuss our measurement, and how we interpret our data to find the surface carrier density and mobility.

To correctly find the geometric factor (g) of the transport geometries that are shown in Fig. (3.2) (a) and Fig. (3.2) (b), we must know where and how much the current flows through each surface. This can be difficult because every surface of SmB_6 conducts, including the top, bottom, side surfaces, and even the edges. To interpret the resistance to the sheet resistance easily, we must choose a simpler geometry. If we can confine the current path to flow on a single surface, we can ignore the surfaces where current does not flow. To this end, we choose a Corbino disk geometry, as shown in Fig. (3.3) (a) and Fig. (3.3) (b). The pattern is shaped by a highly conductive metal on the surface. We used gold in our studies. This metal can be used as terminals, and the current on the sample surface flows radially

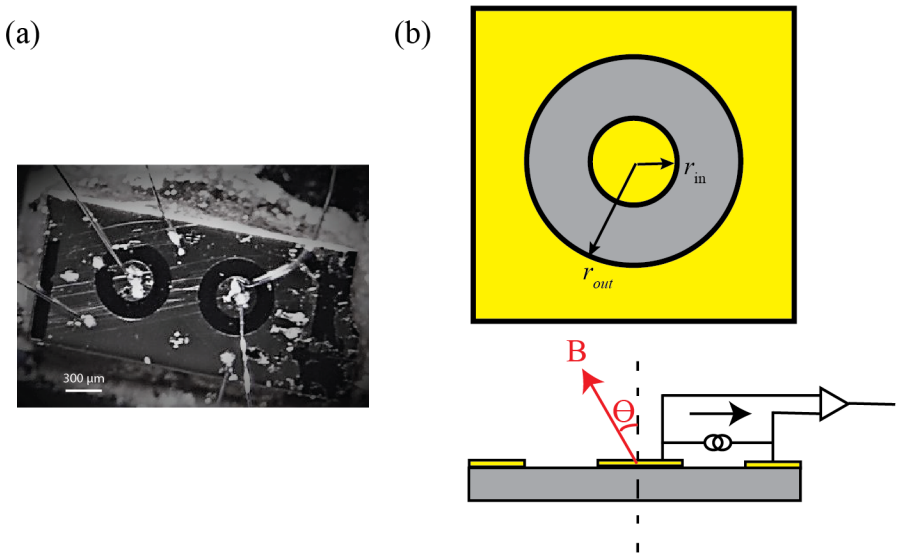

Figure 3.3: Corbino disk(s) for surface SmB_6 studies. (a) Picture of two Corbino disks fabricated on a polished SmB_6 (001) crystalline surface. (b) Top and Side view of the Corbino disk with the electrical configuration. The yellow indicates the highly conductive metal (gold) and the gray indicates the sample. The red arrow indicates the magnetic field direction applied to the sample. In preparation for submission to a journal.

only on the annular region where the sample surface is exposed. In this case, when there is only surface conduction, the measured resistance (R_{Corbino}) and the surface sheet resistance, $R_{\square}$, have the following relation (also derived in Chapter 2):

$$R_{\text{Corbino}} = \frac{1}{2\pi} \ln(r_{\text{out}}/r_{\text{in}}) R_{\square}, \tag{3.1}$$

Currently, our carefully prepared samples measured by a Corbino disk geometry result in a sheet resistance in the range of 2– 3 kΩ, consistently. Comparing to the early sheet resistance estimation from the Hall bar geometry, as shown in Fig. (3.2) (a), this is more than two orders of magnitude higher. In addition to choosing a geometry that confines the surface current path to properly convert the resistance to sheet resistance, surface polishing must also be carefully prepared. We show later in this chapter that hidden cracks in the subsurface region and domains in polycrystals can also conduct, and therefore must be eliminated (Sec. 3.4). In the presence of magnetic field that is in the out-of-plane direction to the surface, the carriers on the surface experience a Lorentz force, and the radial trajectory of the current (or carriers) deflect to form a spiral path in the annular region of the Corbino disk. This effect to the sheet resistance can be derived by the classical Drude picture, and

the result is (also derived in Chapter 2):

$$R_{\square}(B) = (1 + \mu^2 B^2)/ne\mu, \tag{3.2}$$

where μ is the mobility of the surface, n is the carrier density of the surface, and B is the applied magnetic field in the out-of-plane direction. When the magnetic field is tilted to an angle of θ about the out-of-plane direction, only a projection of the surface contributes to the Lorentz force on the carriers. Then, B is replaced to $B\cos\theta$ (where B is the total magnitude of the applied magnetic field), and therefore $R_{\text{Corbino}} \propto (1 + \mu^2 B^2 \cos\theta^2)$. Therefore, in a 2DEG, the resistance would change quadratically with the out-of-plane component of the magnetic field. If the magnetic field is in the in-plane direction, the resistance does not change. Also, when the magnetic field direction is changed at a fixed magnitude, the resistance is expected to follow a cosine square behavior.

Our magnetotransport measurement of SmB_6 employing a Corbino disk on the (001) surface is shown in Fig. (3.4) (a). The temperature is at 0.35 K, and the magnetic field is swept up to 34.5 T while the sample is fixed at certain angles. The trace at the out-of-plane direction (0-degree angle, shown in a black line) deviates from a quadratic behavior. Also, the in-plane direction (90-degree angle, shown in green line), does not show a constant line that is predicted by the Drude model, but rather shows a negative magnetoresistance. However, when dividing the resistances by the in-plane magnetic field resistance ($R(\theta)/R(\theta = 90°)$), the ratio shows a good agreement with the quadratic dependence, as shown in Fig. (3.4) (b). When rotating the angle of the sample while the magnetic field is fixed, the data follows the cosine square behavior, as shown in Fig. (3.4) (c). Fig. (3.4) (b) and Fig. (3.4) (c) show that the surface carriers are still experiencing the Lorentz force in two dimensions. However, from Fig. (3.4) (a), this implies that the surface is an unusual 2DEG in that the carrier density and mobility changes as the magnetic field increases [72]. Fitting a quadratic fit to Fig. (3.4) (b) results in a mobility of 104.5 (cm^2/V·sec) and the carrier density of 2.71×10^{13} ($1/cm^2$). From cosine square fits of Fig. (3.4) (c), the carrier density changes by about 10 %, and the mobility changes by about 3 %. We note that this is our most carefully prepared sample. Two years ago before this measurement shown in Fig. (3.4), we found a larger carrier density and a smaller mobility [72]. Along the journey of characterizing the surface transport of SmB_6, we later found that subsurface cracks that can exist beneath the surface can contribute to surface conduction, and therefore the sheet resistance and mobility can be estimated incorrectly. We discuss about this issue in the following section.

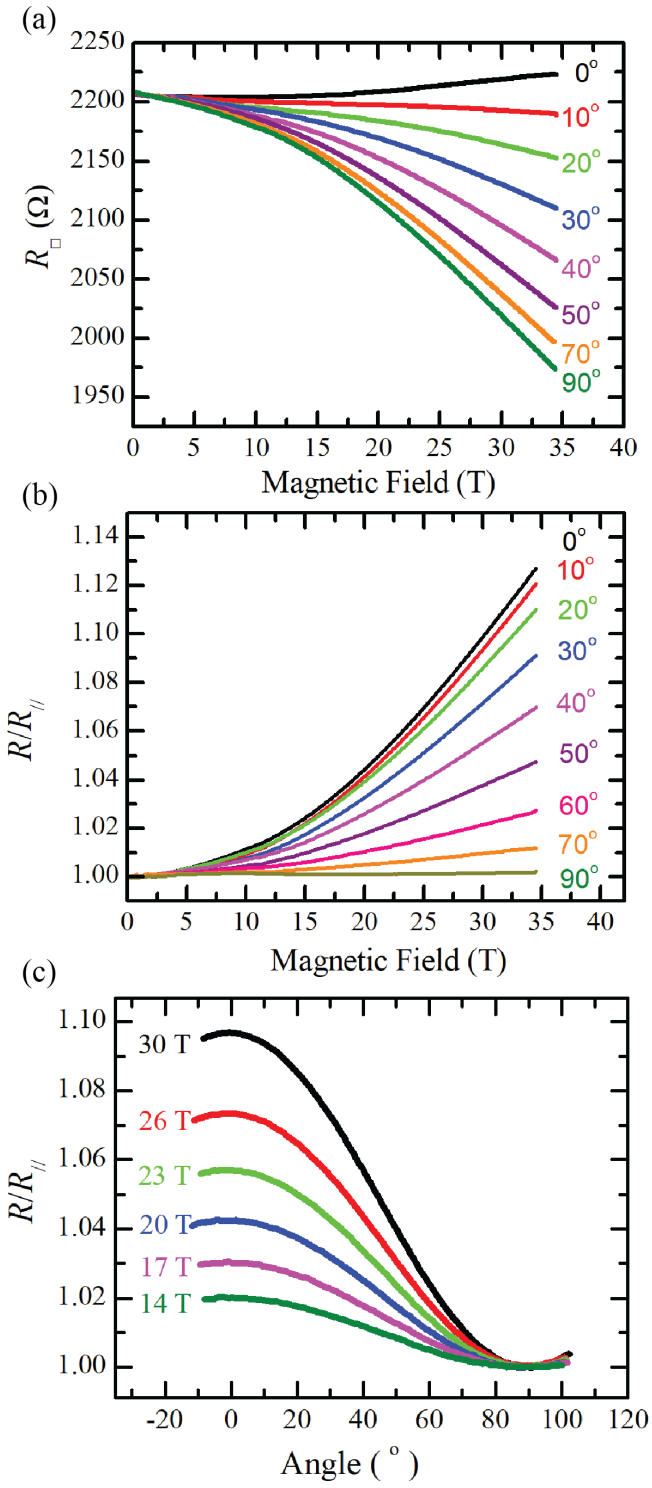

Figure 3.4: Surface magnetotransport results of the Corbino disk on SmB_6. The temperature is at 0.35 K, and the field is raised up to 34.5 T. (a) Sheet resistance vs. magnetic field at different angles of the surface respect to the field direction. (b) Resistance ratio (resistance divided by the resistance at $\theta = 90$ degrees) vs. magnetic field. (b) Resistance ratio vs. angle. In preparation for submission to a journal.

3.4 Conduction through Subsurface Cracks and Domain Boundaries

Within the SmB_6 community, there is a widespread perception that the surface sheet resistance estimated from the resistance plateau below $\sim$3 – 4 K varies from sample to sample. Of course, depending on the crystal growth, the leading order of defects can be different from one sample to another, and some samples can even be non-stoichiometric. While studying surface transport on multiple samples, we found a tendency that is even more disturbing. Sample surfaces that were prepared with rougher polishing tend to result in lower resistance plateau values than the ones that were more finely polished. In typical materials, we would expect the opposite. If the surface is rough, the surface roughness can contribute to extra scattering. Because this scattering will contribute to lowering the mobility, the resistance is expected to be higher.

We hypothesized in this study that subsurface cracks that are created by rough polishing can serve as additional surface conduction paths. If SmB_6 is truly a 3D TI, then since subsurface cracks are termination of the bulk, they must also be topologically protected surfaces. This hypothesis is consistent with the resistance plateau value trend that we observed for different polishing qualities because, in semiconductors, it is well known that rougher polishing creates subsurface cracks with larger length scales [74, 75].

To test the hypothesis that subsurface cracks contribute to surface conduction, we prepared an SmB_6 sample with two Corbino disks fabricated on a fine polished surface. The resistance vs. temperature was measured below $\sim$4.5 K, before and after the active region (annular ring) of one of the Corbino disk was scratched with a scriber, as shown in Fig. (3.5) (a). As shown in Fig. (3.5) (b), while the plateau resistance of the unscratched Corbino disk remains almost identical within a few percent, the plateau resistance of the scratched Corbino disk further lowered from 140 Ω to 110 Ω. After the second scratch, the resistance further lowers to 60 Ω. Indeed, the surface roughness increases after scratching the surface, but the resistance does not become higher, it rather becomes lower, consistent with our hypothesis that subsurface cracks conduct.

We further investigated if a scratched surface indeed harbors subsurface cracks. An ion-beam milling was performed on the scratched surface. The ion-milled wall profile is shown in Fig. (3.5) (c) through a SEM image. We indeed observed subsurface cracks that are several microns long and up to 100 nm wide. Normally, we would expect that the polishing grit particles would introduce a stress to the surface, and therefore create subsurface cracks. The length scales of these subsurface cracks would scale with the size of the grit particles. Therefore, the sample must be polished with the finest possible grit size and

thinned sufficiently to eliminate the subsurface cracks that are created from the rougher polishing grit introduced in the previous polishing step.

Next, we consider surfaces that are as-grown. In most of the crystals that we receive from the crystal growers with whom we collaborate, the area of the as-grown crystalline surfaces is too small to fit a Corbino disk pattern, and therefore the samples have to be thinned until a large enough surface is obtained. However, if thinning and polishing can potentially create cracks, a single crystal that begins with a large enough surface is desirable. We were fortunate to obtain a single crystal that had a large enough area to fabricate a Corbino disk, as shown in Fig. (3.6) (a). In comparison, we also fabricated a Corbino disk on a polycrystalline sample. The surface of this sample is large enough to fit a Corbino disk pattern but consists of many domains. Both samples did not undergo any thinning or polishing treatments. The samples were only cleaned in dilute HCl before and after the lithography process. We measured both the resistance vs. temperature using the standard Corbino disk measurement (shown in Fig. (3.3) (b)). The results are shown in Fig. (3.6) (c). The resistance curve of the single crystalline surface is shown in a blue line, and the polycrystalline surface is shown in the red line. The single crystal shows a resistance plateau of $\sim$260 Ω, which the corresponding sheet resistance is 2.3 kΩ. This value is consistent with the measurement of the sample that was most carefully polished, presented in the previous section (Sec. 3.3). On the other hand, the resistance plateau value of the polycrystalline sample is only 3.2 Ω. We believe that the domain boundaries serve as conduction paths, similar to that of the conduction through subsurface cracks.

In conclusion, we believe the true sheet resistance of the SmB_6 is 2 - 3 kΩ when the sample is free from cracks or domains. This is consistent with the minimum sheet resistance of 1kΩ for the surface to exist, according to the AC conductivity report from N. Laurita *et al* [76].

In this section, we have emphasized through the set of our experimental demonstrations that the surface of SmB_6 must be carefully prepared. To obtain the desired transport geometry, a widespread practice is thinning and polishing the crystal. However, we have shown that since SmB_6 is a surface conductor, particularly if the conducting surface is topologically protected from a true 3D TI, then subsurface cracks and even domain boundaries are termination regions of the bulk, and can provide extra conduction. After measuring multiple samples over several years, we consistently see a sheet resistance of 2 – 3 kΩ for carefully prepared surfaces. In the following section, we explain how the magnetotransport is influenced by the surface preparation. Also, we provide a summary of how our understanding of the transport parameters (sheet resistance, surface carrier density, and mobility) has evolved.

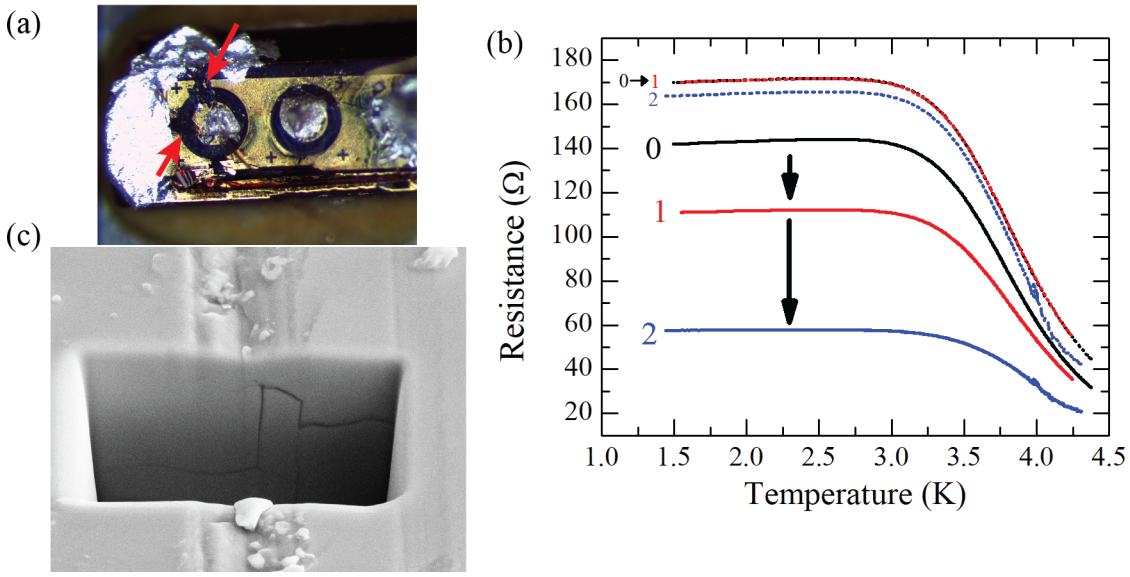

Figure 3.5: Conduction through subsurface cracks. (a) Picture of the scratched Corbino disk sample. The scratched parts are indicated in red arrows. (b) The resistance change after scratching the sample. (c) SEM picture of subsurface cracks after ion-milling a section beneath the scratched region [73]. In preparation for submission to a journal.

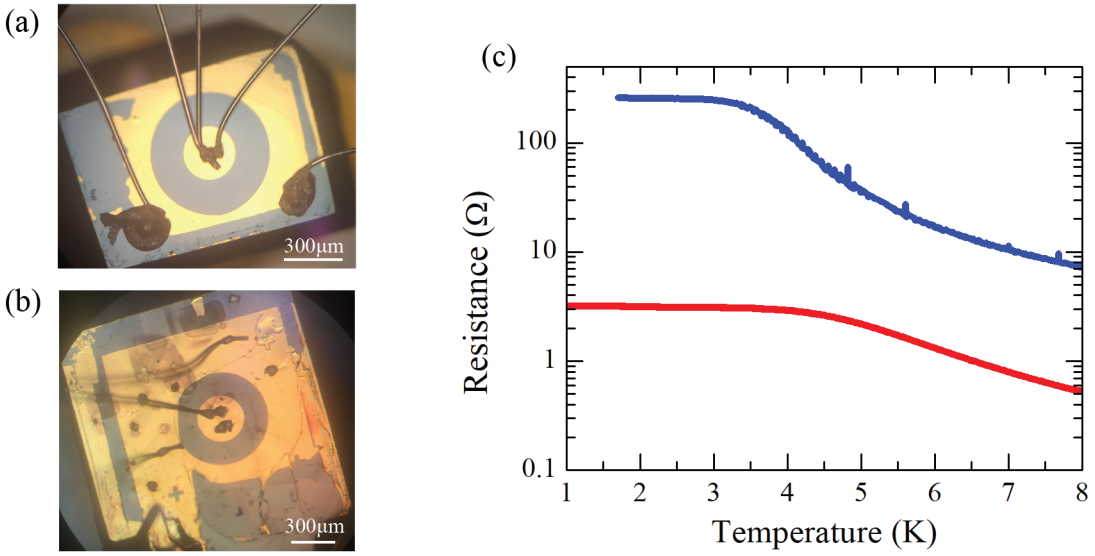

Figure 3.6: Comparison of resistance vs. temperature of a Corbino disk on unpolished single crystal vs. polycrystal. (a) Corbino disk on a clean single crystal surface in the (001) direction. (b) Corbino disk on a clean polycrystal surface with many domain boundaries. (c) Resistance vs. temperature of the two samples. The blue curve is measured from sample (a), and the red curve is measured from sample (b). In preparation for submission to a journal.

3.5 Evolution of our Understanding of the Surface Transport Parameters

In this section, we explain how the magnetotransport of a Corbino disk on a SmB_6 surface becomes influenced by the existence of subsurface cracks. This is important because the carrier density and mobility is found by magnetotransport. Throughout our several years of study of surface transport on SmB_6, our understanding of the transport parameters (sheet resistance, surface carrier density, and mobility) have evolved by first changing from the Hall bar geometry to the Corbino disk geometry, and then preparing the samples carefully without subsurface cracks. We will summarize at the end how our estimated transport parameters have changed.

As an instructive example, we consider two of our magnetotransport results that were taken before and after we were aware of subsurface crack conduction. In 2013, when we were not aware of subsurface crack conduction, the Corbino disk sample was prepared by final polishing with a SiC polishing pad with an average grit size of 2.5 μm [40]. In 2015, the Corbino disk sample was prepared by final polishing with an Al_2O_3 oxide with a particle size of 0.3 μm.

The resistance vs. magnetic field, fixed at different angles, is shown in Fig. (3.7). The 2015 data is identical to the result shown in Fig. (3.4). The extraction through fitting of this data results in mobility of 104.5 $cm^2/(V{\cdot}sec)$ and the carrier density of $2.71{\times}10^{13}$ cm^{-2}. Comparing to the 2015 experiment, the measurement taken in 2013 shows a smaller sheet resistance at zero magnetic field. This is consistent with the subsurface cracks existing in the samples that are not prepared carefully enough. In addition, the 2013 data set shows a weaker angle dependence. If we assume that the subsurface cracks are randomly oriented, the carriers in the subsurface cracks will feel a weaker Lorentz force on average than the surface carriers on the crystalline surface. This will effectively weaken the angle dependence of resistance at magnetic fields. The weaker angle dependence results in a smaller estimation of mobility, which is 61 $cm^2/(V{\cdot}sec)$, and because the sheet resistivity is smaller, a larger carrier density is estimated, which is $2{\times}10^{14}$ cm^{-2}.

We summarize in Table (3.1) how our transport parameter estimations have evolved. From Hall bar geometry to the Corbino disk geometry, and then further carefully preparing the surface, our estimation of transport-related values has changed. The sheet resistance and mobility became higher, and carrier density became lower. Although our most recent mobility estimation is higher than what we had originally estimated, this value is small compared to high-quality 2DEG systems. We believe this is why SdH oscillations are not yet observed. Just by relying on classical magnetotransport analysis, we did not observe

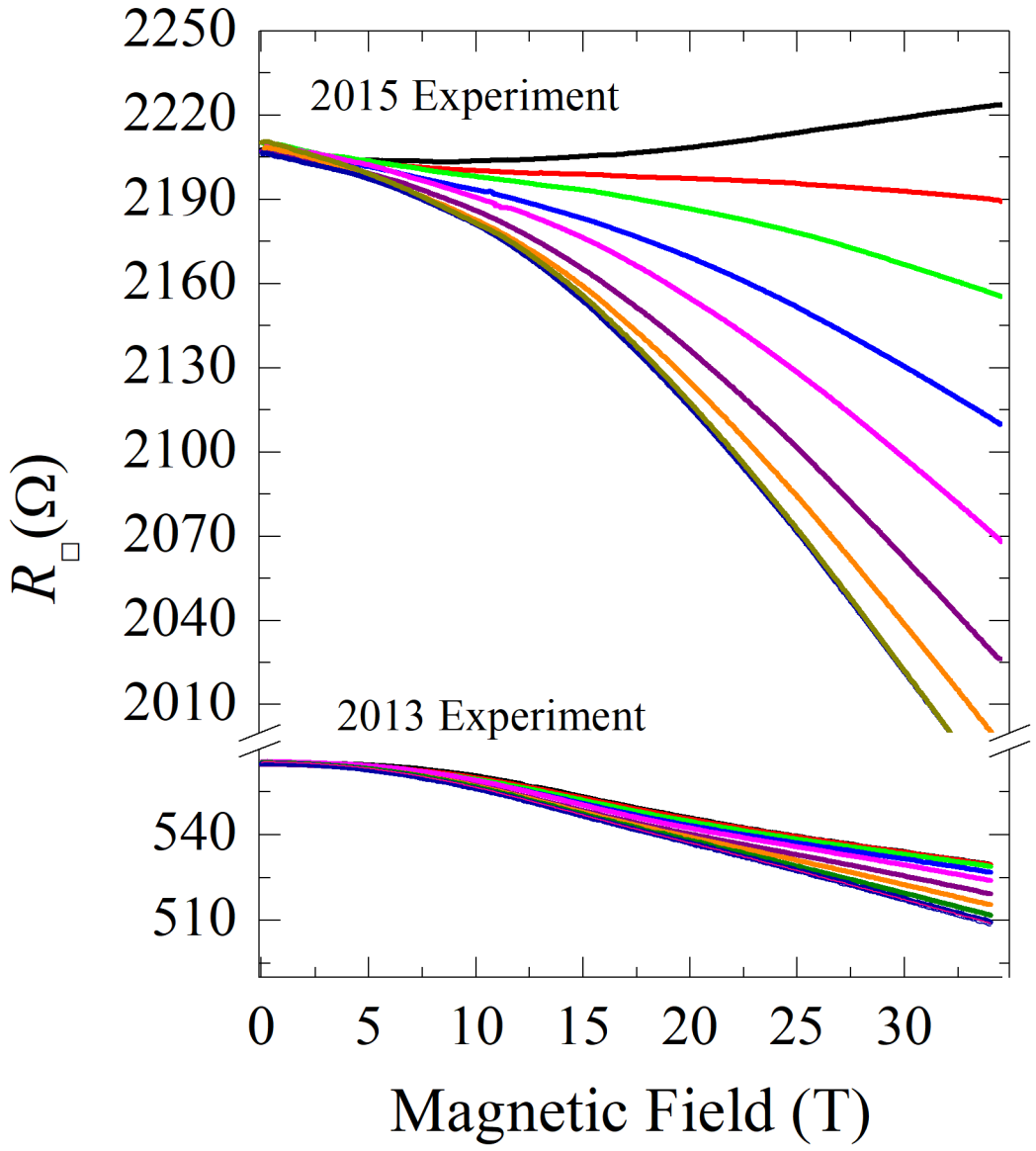

Figure 3.7: Comparing magnetotransport of Corbino disk on a (001) surface of SmB_6 from 2013 [72] and 2015. The temperature is at 0.35 K, and the magnetic field is swept while the angle of the magnetic field is kept fixed. In preparation for submission to a journal.

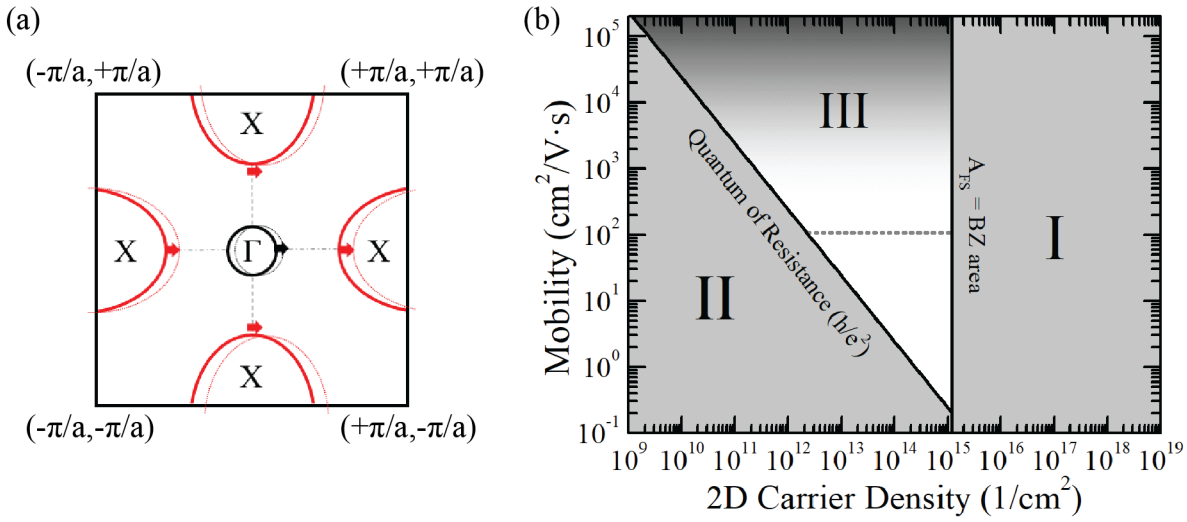

Figure 3.8: (001) surface of SmB_6. (a) The three Fermi pockets of the BZ on the (001) surface. The solid red lines indicate the X-pockets, and the solid black line indicates the Γ-pocket. The dotted lines indicate how the Fermi surfaces deform if the electric field is applied in the k_x-direction. (b) The surface transport parameter space of SmB_6 in the (001) direction. The gray area (region I and II) are the forbidden regions where the parameters cannot exist. The dotted line indicates the mobility of 1/(93 T). In region III, it is shown in a gradient color, and the darker area indicates that the transport parameters would be less likely to exist at higher mobilities. In preparation for submission to a journal.

clear signatures of the existence of multiple channels from magnetotransport in contrast to other experimental reports such as ARPES and dHvA that report on multiple pockets. In the following section, we discuss why our magnetotransport does not show signatures of multiple channels based on the low mobility of the surface carriers.

Year	Geometry	$R_\square$ (Ω)	n_{2D} (cm^{-2})	μ_{2D} (cm^2/V·sec)
2012	Hall bar [40]	9.1	1.0×10^{18}	6.90×10^{-1}
2013	Corbino Disk [72]	570	2.0×10^{14}	6.1×10
2015	Corbino Disk (in prep.)	2200	2.71×10^{13}	1.05×10^{2}

Table 3.1: Surface transport parameter estimation from measurements at different years.

3.6 Constructing the Transport Parameter Space of Each Channel

The 3D topological Kondo insulator theory predicts that three surface Fermi pockets exist, each surrounding a high symmetry point in the Brillouin zone (BZ) [70, 77]. In particular, on the (001) crystal surface, theory predicts that one of the Fermi pockets should surround the Γ-point (or Γ-pocket in short), and the other two should surround the X-point (or X-pocket in short), as shown in solid red in Fig. (3.8) (a). If SdH oscillations are observed, the verification of each pocket would have been possible. As mentioned previously, SdH was not observed up to 93 T, and therefore our analysis is based on classical transport. The quadratic fit of $R(B)/R_{/\!/}$ at a fixed angle and a cosine square fit of $R(\theta)/R_{/\!/}$ at a fixed magnetic field relying on Eq. (3.2) assumes that only a single channel (or Fermi pocket) exists in the BZ.

In our magnetotransport results shown in Fig. (3.4), the reason we were not able to observe distinct signatures of multiple channels can be explained if the mobilities of each channel are small. Being consistent with the picture of Fig. (3.8) (a), if an electric field is applied in the $+k_x$ direction in the BZ, the Fermi surfaces will change such as the dotted lines. We can treat each pocket with the relaxation-time approximation in the Boltzmann equation, as introduced in Chapter 2. We simplify the case that the top and bottom X-pockets contribute equally as the left and right X-pockets by assuming that the associated scattering time does not depend on the direction of crystal momentum. Then the total conductivity (σ_t) corresponding to two channels, σ_Γ and σ_{2X}, add together as the total conductivity:

$$\sigma_t = \sigma_\Gamma + \sigma_{2X}. \tag{3.3}$$

Furthermore, when a magnetic field is applied, we assume the carrier density and mobility that we find from experiment is an effective parameter (n_{eff} and μ_{eff}) from the two pockets, i.e., $\sigma_t = n_{\text{eff}} e \mu_{\text{eff}}$. The magnetoconductivity can also be expressed in terms of the transport parameters of the two pockets:

$$\frac{n_{\text{eff}} e \mu_{\text{eff}}}{1 + \mu_{\text{eff}}^2 B^2 \cos^2\theta} = \frac{n_\Gamma e \mu_\Gamma}{1 + \mu_\Gamma^2 B^2 \cos^2\theta} + \frac{n_{2X} e \mu_{2X}}{1 + \mu_{2X}^2 B^2 \cos^2\theta}, \tag{3.4}$$

where n_Γ (n_{2X}) is the surface carrier density of the Γ-pocket (two X-pockets), and μ_Γ (μ_{2X}) is the mobility of the Γ-pocket (two X-pockets). $R(B)/R_{/\!/}$ at a fixed angle or $R(\theta)/R_{/\!/}$ at a fixed magnetic field would be inversely proportional to Eq. (3.4). The inverse of Eq. (3.4)

can be expanded in a series, and dividing by $R_{/\!/}$ ($= 1/\sigma_t$) is:

$$\frac{R(B,\theta)}{R_{/\!/}} = 1 + \mu_{\text{eff}}^2 B^2 \cos^2\theta + (\frac{\sigma_\Gamma}{\sigma_t} - (\frac{\sigma_\Gamma}{\sigma_t})^2)(\mu_\Gamma^2 - \mu_{2X}^2)^2 B^4 \cos^4\theta + \cdots, \tag{3.5}$$

where,

$$\mu_{\text{eff}} = \sqrt{(\mu_\Gamma^2 - \mu_{2X}^2)(\frac{\sigma_\Gamma}{\sigma_t}) + \mu_{2X}^2}. \tag{3.6}$$

From Eq. (3.5), we can see that as long as any of the mobilities (μ_Γ and μ_{2X}) from the channels are much smaller than $1/B$, the third order term or higher in Eq. (3.5) will be overwhelmed by the second order term, and Eq. (3.5) will be indistinguishable from the magnetotransport for the single channel equation, Eq. (3.2). Therefore, we will not be able to tell if there are two channels from magnetotransport. Also, Eq. (3.6) is the effective mobility from fitting our data. Furthermore, the effective carrier density is:

$$n_{\text{eff}} = \frac{\sigma_t}{e\mu_{\text{eff}}} = \frac{(n_\Gamma\mu_\Gamma + n_{2X}\mu_{2X})^{3/2}}{(n_\Gamma\mu_\Gamma^3 + n_{2X}\mu_{2X}^3)^{1/2}}. \tag{3.7}$$

We have so far explained why our magnetotransport of a Corbino disk fails to resolve signatures of multiple pockets. In the following subsections, we will show that the transport parameters from each pocket can only be existing in a constrained space. Furthermore, together with our (effective) surface carrier density and mobility results, we will further corner the range (or area) of the parameter spaces, where each pocket should exist. This result will be used to compare with other experimental reports.

3.6.1 Forbidden Parameter Space

In a 2D transport, there are two fundamental limits that constrain the parameter space. First, the size of the Fermi pocket cannot be larger than the defined surface Brillouin zone of the material. When a periodic boundary condition (Born-von Karman) is chosen to describe the system of interest in quantum mechanics, there is a relation of occupied area (or volume) in k-space to the associated density of particles (carriers). In a two-dimensional system, this relation is:

$$n_{2D} = \frac{s}{(2\pi)^2} A_{\text{FS}}, \tag{3.8}$$

where A_{FS} is the area of the Fermi pocket, and s is the spin degeneracy ($s = 2$ for typical materials, $s = 1$ when the spin degeneracy is split). The maximum allowed surface carrier density is then, of course, related to the total area of the BZ. The maximum carrier density allowed on the (100) surface of SmB_6 is $n_{\text{max}} = 5.86\times10^{14}$ cm^{-2} when there is no spin

degeneracy (in a true 3D TI case). Therefore, any carrier density larger than this value is forbidden. In Fig. (3.8) (b), the surface transport parameter space, which we plot the mobility and surface carrier density in a log-log graph, this forbidden region indicated as region I, shaded in gray color.

Next, in 2D transport, it is well known that a system undergoes a metal-to-insulator transition when $R_\square$ becomes larger than the quantum of resistance, h/e^2 (Ioffe-Regel criterion). Therefore, $R_\square$ larger than the quantum of resistance must be forbidden. The diagonal line in Fig. (3.8) (b) represents $R_\square = h/e^2$ (or quantum conductivity: $\sigma_s = e^2/h$), and region II, the gray shaded region that is below the diagonal line is the forbidden region.

The absence of SdH oscillation up to 93 T, as shown in Fig. (3.1), also provides a constraint to the pockets in the parameter space. First, we revisit the Lifshitz-Kosevich (LK) formalism very briefly. The conductivity oscillates with a damping factor that is related to the scattering of the carriers. This is the Dingle damping factor (D_D), and it is related to the mobility. The Dingle damping factor is:

$$D_D = \exp(-\frac{\pi}{\mu_Q B}), \tag{3.9}$$

where $\mu_Q = e\tau_Q/m^*$ is the quantum mobility. In the semi-classical approach, τ is estimated by the Fermi-golden rule where the scattering potential is multiplied by an extra factor, $(1 - \cos\theta)$, so that it does not include the forward scattering [78, 79]. This factor is not included in the τ_Q (quantum scattering time) in quantum oscillations and can differ from τ found from our classical (or semiclassical) transport approach. We will re-visit the LK formalism when comparing our transport to the dHvA results [60].

From the dingle factor (D_D), we see that the onset of quantum oscillations would be at higher magnetic fields if the mobility of the carrier is lower. Of course, the exact onset magnetic field estimation would depend on the sensitivity of the measurement, how we model the broadening of the Landau levels due to disorder, and the prefactor of the quantum scattering time, etc. A crude estimate of the onset of quantum oscillations is when $\mu B \approx 1$, or $B \approx 1/\mu$. Therefore, the absence of SdH up to 93 T, which is the highest magnetic field ever applied on the SmB_6 (001) surface, tells us that the magnetic field requirement for the onset of SdH oscillations must be higher, and therefore the mobility would be in the vicinity of 1/(93 T) or less. In Fig. (3.8) (b), the mobility of 1/(93 T) is shown as a horizontal dotted line, and the area above is indicated in region III. The transport parameters would be less likely to exist at a higher mobility, although strictly not forbidden. To graphically show this in the figure, region III is shown in a gradient color that becomes darker at higher mobility ranges.

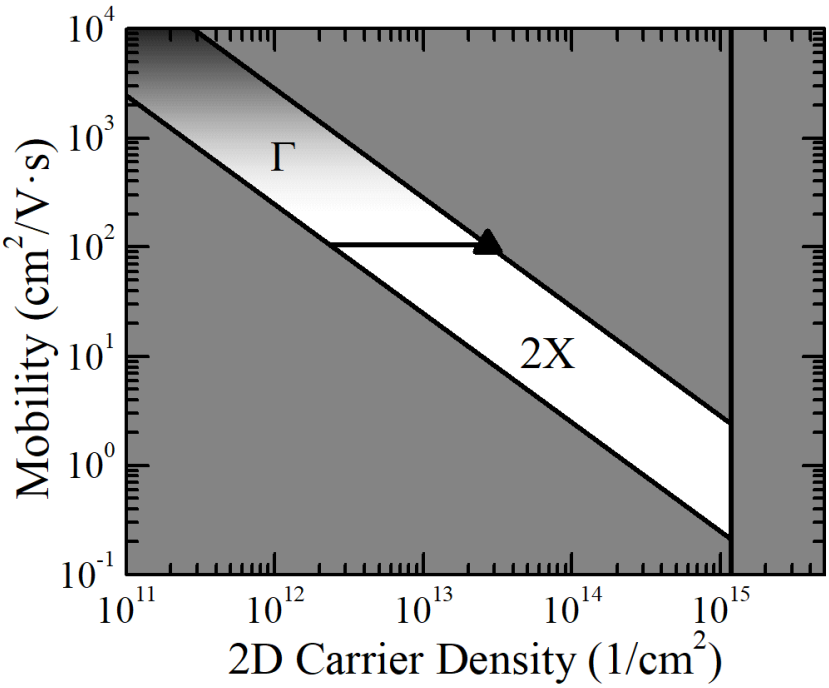

Figure 3.9: The surface transport parameter space of SmB_6 on the (001) surface. In preparation for submission to a journal.

Excluding the regions of I and II, and since the high mobility far above 1/(93 T) is less likely, the Fermi pockets must be in or near the white triangular region in Fig. (3.8) (b). Next, we continue with the effective mobility and carrier density found from our Corbino disk magnetotransport, we constrain the parameter space regions where each pocket can be allowed.

3.6.2 Cornering the Transport Parameter Space Region for Each Pockets from Corbino Magnetotransport

In this subsection, we construct a parameter space region where each channel (Γ and $2X$) can be located in the (001) surface from our magnetotransport result. The magnetotransport result of surface carrier density and mobility ($n_{\text{eff}} = 2.71\times10^{13}$ cm^{-2} and $\mu_{\text{eff}} = 104.5$ cm^2/(V·s)) from the Corbino disk is shown in the transport parameter space as a black triangular symbol in Fig. (3.9). If we assume that our magnetotransport is a result of two channels, we use Eq. (3.3):

$$\sigma_t = \sigma_t = n_{\text{eff}} e \mu_{\text{eff}} = \sigma_\Gamma + \sigma_{2X}. \tag{3.10}$$

In the transport parameter space, carrier density and mobility pair of each channel should be represented as a point. The corresponding conductivities of each two points must add up and result in the conductivity corresponding to the triangular point (effective parameters). The two points that represent the transport of each channel is somewhere in the triangular region of Fig. (3.8) (b) or the allowed parameter space. Also, to be consistent with Eq. (3.3) – Eq. (3.7), one of the mobilities must be larger while the other mobility must be smaller than μ_{eff} (detailed justification is in Appendix A). Then, the allowed parameter space of the channel with the small carrier density (Γ-pocket), and the channel with the large carrier density ($2X$-pocket) should be in the regions that are indicated in Fig. (3.9). Although we cannot specify the exact carrier density and mobility values, the small carrier density channel must be in region Γ, and the large carrier density channel must be in region $2X$. In the following section, we compare our constructed parameter space to other experimental reports such as Hall, dHvA, and ARPES.

3.7 Comparison with other Experiments

In this section, we compare our constructed transport parameter space from the previous section to other experimental reports on the SmB_6 (001) surface.

Before we compare our transport parameters space to other experiments, we must know how to estimate the carrier density and mobility from non-transport experiments. In the following subsections, we briefly review how.

3.7.1 Quantum Oscillation (dHvA) Interpretation

When the area of the Fermi surface in the BZ has a size of A_{FS}, the associated frequency of quantum oscillations, F, follow the Onsager relation:

$$F(T) = \frac{\hbar}{2\pi e} A_{\text{FS}}. \tag{3.11}$$

Also, since the carrier density (n) and A_{FS} are related (Eq. (3.8)), the relation between n and F can be found as:

$$n_{2D} = s\frac{e}{h}F(T), \tag{3.12}$$

where s is the spin degeneracy ($s = 2$ for typical materials, $s = 1$ when the spin degeneracy is split).

According to the LK formula, the amplitude of the oscillations is damped by two factors. The temperature damping factor (D_T), and the Dingle damping factor (D_D), which was

introduced previously (Eq. (3.9)). The two damping factors are given by:

$$D_D = \exp(-\frac{\pi}{\mu_Q B}), \tag{3.13}$$

$$D_T = \frac{2\pi^2(k_B T/\hbar\omega_c)}{\sinh(2\pi^2(k_B T/\hbar\omega_c))}, \tag{3.14}$$

where ω_c ($=eB/m^*$) is the cyclotron frequency. From the temperature dependence of the amplitude of quantum oscillations, the effective mass, m^*, can be found. From the magnetic field dependence of the amplitude at a fixed temperature, the dingle damping factor (D_D) can be used to find μ_Q.

3.7.2 ARPES Interpretation

In ARPES, the momentum and energy resolved intensity data ($I(k,\omega)$) is measured and is understood by the spectral density function, $S(k,\omega)$, associated with removal of electrons from photons, with energy ω [80, 81]:

$$I(k,\omega) = f(E)S(k,\omega), \tag{3.15}$$

where $f(E)$ is the Fermi-Dirac distribution and $S(k,\omega)$ is given by:

$$S(k,\omega) = -\frac{1}{\pi}\frac{\mathrm{Im}(\Sigma)}{[\omega - E(k) - \mathrm{Re}(\Sigma)]^2 + \mathrm{Im}(\Sigma)^2}. \tag{3.16}$$

where Σ is the self energy. Notice from Eq. (3.15) that $I(k,\omega)$ becomes weak above the Fermi energy because of $f(E)$. Also notice that when the photon energy approaches to, $\omega \to E(k) - \mathrm{Re}(\Sigma)$, the magnitude of $I(k,\omega)$ enhances. Therefore, ARPES can measure the energy dispersion below the Fermi energy and slightly above at finite temperatures, with the momentum dependence. By resolving different momentum directions at the Fermi energy, $E_F(k)$, the size(s) and shape(s) of the Fermi pocket(s) can be found. The size of the Fermi pockets can be converted to carrier density from Eq. (3.8). From the slope or curvature of the dispersion $E(k)$ below the Fermi energy, the effective mass (m^*) can be found. Furthermore, the spectral broadening is related to the momentum relaxation, and the associated scattering time, τ_p, is:

$$\frac{1}{\tau_p} = -2\mathrm{Im}(\Sigma). \tag{3.17}$$

Therefore, the mobility can be found by $\mu = e\tau_p/m^*$.

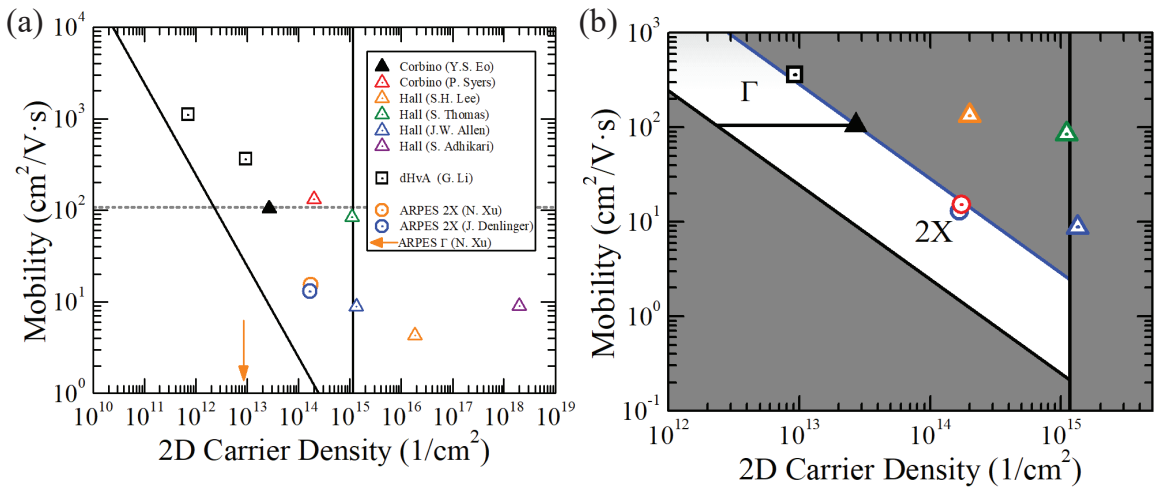

Figure 3.10: Comparison of surface transport parameters of SmB_6 on the (001) surface. (a) Comparison in a large transport range. (b) Comparison near the cornered parameter space. The triangular points are the transport reports. The square points are from the dHvA quantum oscillation. The circular points are from the ARPES X-pockets. The arrow is the carrier density estimation of the Γ-pocket from ARPES. In preparation for submission to a journal.

3.7.3 Comparison Studies in the Parameter Space and Discussion

Now with these conversion relations that we have reviewed, we plot the reported transport, ARPES, and dHvA studies on the (001) surface of SmB_6 in the transport parameter space, as shown in Fig. (3.10). We note that because it is too crowded to plot all of the transport parameters in this figure, we also provide a table of the transport, as shown in Table (3.2), and the table of APRES, as shown in Table (3.3), that also includes the data points that are omitted in the graph. The transport reports, including our Corbino magneto-transport, is shown in triangular symbols. The early Hall effect data shows very high surface carrier density, which some of them even exceed the maximum carrier density associated with the BZ area. The very large carrier density tendency of these data points is consistent with our old estimation from the Hall geometry measurement. The dHvA quantum oscillations by G. Li *et al.* [60] report two Fermi pockets that originate from the (001) surface, plotted in hollow-square symbols. The dHvA results show the highest mobility and lowest carrier density in the transport parameter space. We note that the mobility estimated from the dHvA oscillations is the quantum mobility (μ_Q). Typically, μ_Q and μ differ slightly. Next, the ARPES reports of the X-pockets are plotted in circular points. All the ARPES reports that agree with the existence of the surface states, see a very large X-pocket. Among these reports, two of them from J. Denlinger *et al.* [62], and N. Xu *et al.* [64] report the Im(Σ),

and therefore the mobility of the X-pocket can be estimated. There are three groups who report the existence of the Γ-pocket [64–66], but none of them have reported corresponding Im(Σ). Since we can only estimate the surface carrier density from the area of the pocket, we show one of the conversion from N. Xu *et al.* [64] as an (orange) arrow pointing to the corresponding carrier density.

When we compare with our constructed parameter space that is shown in Fig. (3.9) to the data sets shown in Fig. (3.10), only the ARPES reports from the X-pocket are within the constructed parameter space ($2X$ region). The dHvA reports do not agree with our constructed parameter space because both carrier densities of the two pockets cannot have higher mobilities than the effective mobility we find from magnetotransport(See Appendix A for reasoning).

Finally we briefly mention the Cambridge results, although our study does not aim to re-interpret the bulk origin claim to the surface. There has been a study that re-considers the quantum oscillations from the Cambridge group by Tan *et al.* [61] as a surface origin instead of a bulk origin [63]. The corresponding Fermi surface area of the high frequencies is consistent with the X-pocket observed by ARPES. When comparing the Cambridge quantum oscillations with our transport, the corresponding carrier density is also consistent with the 2X parameter space that we constructed. However, the associated mobility for the onset of those high-frequency quantum oscillations is far too high to be consistent with our transport parameter space and the ARPES reports.

Report	Geometry	n_{2D} (cm^{-2})	μ_{2D}(cm^2/V·sec)
Y.S. Eo *et al.* (2015) (in prep.)	Corbino	2.71×10^{13}	104.5
S. Wolgast *et al.* (2013) [72]	Corbino	2.0×10^{14}	6.1×10
P. Syers *et al.*(2015) [82]	Corbino	1.0×10^{18}	6.8×10^{3}
S. Thomas *et al.* (2013) [83]	Hall*	2.0×10^{14}	133
S.H. Lee *et al.* (2013) [84]	Thin Film Hall	1.86×10^{16}	4.27
S. Adhikari *et al.* (2015) [85]	Hall	2.0×10^{18}	9
J.W. Allen *et al.*(1979) [25]	Hall*	1.34×10^{15}	8.82

Table 3.2: Summary of the transport parameters from transport experiments. *The carrier density and mobility are estimated naively by the Hall coefficient, thickness, and resistivity without the exact geometry information

3.7.4 Estimation of Mobility of ARPES Fermi Pockets

In this subsection, by comparing our effective transport parameters from the Corbino disk magnetotransport with the ARPES reports, we can further estimate what the mobility

Report	Pocket	n_{2D} (cm^{-2})	μ_{2D}(cm^2/V·sec)
J. Denlinger *et al.* (2013) [62, 63]	$2X$	1.67×10^{14}	13
N. Xu *et al.* (2013) [64]	$2X$	1.74×10^{14}	15.2
N. Xu *et al.*(2013) [64]	Γ	8.61×10^{12}	N/A
J. Jiang *et al.* (2013) [65]	$2X$	1.92×10^{14}	N/A
J. Jiang *et al.* (2013) [65]	Γ	6.45×10^{12}	N/A
M. Neupane *et al.* (2013) [66]	$2X$	3.01×10^{14}	N/A
M. Neupane *et al.*(2013 [66])	Γ	9.39×10^{12}	N/A

Table 3.3: The transport parameters estimated from ARPES.

value of each pocket should be. Here we review two equations, Eq. (3.3) and Eq. (3.4).

$$\sigma_t = \sigma_\Gamma + \sigma_{2X}, \tag{3.18}$$

Furthermore, when a magnetic field is applied, we assume the carrier density and mobilty we find from experiment is an effective parameter (n_{eff} and μ_{eff}) from the two pockets, i.e., $\sigma_t = n_{\text{eff}} e \mu_{\text{eff}}$. The magnetoconductivity is then:

$$\frac{n_{\text{eff}} e \mu_{\text{eff}}}{1 + \mu_{\text{eff}}^2 B^2 \cos^2\theta} = \frac{n_\Gamma e \mu_\Gamma}{1 + \mu_\Gamma^2 B^2 \cos^2\theta} + \frac{n_{2X} e \mu_{2X}}{1 + \mu_{2X}^2 B^2 \cos^2\theta}. \tag{3.19}$$

Here the known parameters are n_{eff} and μ_{eff}, where we use our magnetotransport results, and n_Γ and n_{2X} from the ARPES reports in Table (3.3). Using the two equations above, we can solve for μ_Γ and μ_{2X}. We report the results in Table (3.4).

Our results predict that the μ_Γ to be in the $\sim$150 cm^2/V·s range. A smaller Γ-pocket area requires a larger μ_Γ to be consistent with our magnetotransport report.

Report	μ_Γ (cm^2/V·sec)	μ_{2X}(cm^2/V·sec)
N. Xu *et al.* (2014) [64]	168.36	9.11
J. Jiang *et al.* (2013) [65]	148.73	4.78
M. Neupane *et al.*(2013) [66]	152.96	8.71

Table 3.4: Estimation of mobility of the Fermi pockets ARPES after comparing with the Corbino magnetotransport.

3.8 Conclusion

In this chapter, we have studied the surface transport of SmB_6 using high-field magneto-transport at low temperatures. We have not been able to observe SdH quantum oscillations

in our studies, and therefore we were not able to see signatures of multiple Fermi pockets. To properly characterize the surface without SdH oscillations, we have discussed the importance of employing the proper transport geometry and the surface preparation for the surface transport studies. From our estimated carrier density and mobility, we were able to corner the parameter space of the possible carrier density and mobility values of each Fermi pocket (each channel). Our constructed parameter space is consistent with only the ARPES X-pocket reports.

Chapter 4

Inverted Resistance Measurement

4.1 Introduction

[1]In the previous chapter, we presented our surface transport studies of SmB_6 at temperatures below 3 – 4 K (bulk-to-surface crossover temperature). We were able to study the surface because the bulk was truly insulating. For a truly bulk insulator, the conductivity of the bulk becomes smaller at lower temperatures because there are fewer thermally activated carriers in the conduction band. At temperatures above 3 – 4 K, the current flows mostly through the bulk because the bulk conductivity is much higher than the surface conductivity. Below 3 – 4 K, this is no longer true, and the current flows mostly through the surface.

This truly insulating bulk is already fascinating, especially when it is compared to the bulk of weakly correlated 3D TIs such as $Bi_{1-x}Sb_x$, Bi_2Se_3, and Bi_2Te_3. In these 3D TIs, the bulk conduction by unintentional impurities is large enough to overwhelm the surface conduction at all temperature ranges. Therefore, surface studies of these materials are commonly done on ultrathin films and rely on quantum oscillations.

Therefore we raise the question: Why is the bulk of SmB_6 so immune to impurities and disorder in the first place? In addition to this question, the truly insulating bulk behavior itself needs to be investigated in more depth. There are many bulk studies on the thermally activated bulk behavior of SmB_6 above the crossover temperature, but not below. The activation energy is reported in the range of 3 – 4 meV. However, it is not clear whether this thermally activated bulk behavior will continue below this temperature. Measuring the bulk property below the crossover temperature seems almost impossible because the current flows mostly on the surface and almost no current flows through the bulk.

When there is a challenging experiment, sometimes a new method must be invented

[1]This work has been posted on ArXiv [86]. The author and his collaborators are preparing a manuscript for submitting to a peer-reviewed journal that will contain contents in this chapter.

first. To that end, we invented a new transport strategy, called the *inverted resistance measurement*. This chapter is devoted to explaining our new invention of transport geometries and measurement techniques that employ this inverted resistance measurement. An actual demonstration and further bulk studies on SmB_6 and its systematically-grown disordered samples (SmB_6 grown with less Sm) will be presented in the following chapters.

4.2 Resistivity Ratio and its Limitations

In the case of isotropic three-dimensional crystals, the conductivity can be found using four-terminal resistance measurements. The measured resistance is inversely proportional to the conductivity of the material with a prefactor that depends on the geometry of the sample and the position of the contacts. Except for special cases such as a long wire or a thin film, this geometric prefactor can only be determined by numerical calculations. Researchers, especially in the correlated electron community, sometimes perform transport measurements on raw crystals that have irregular shapes. Commonly they do not supplement the transport measurements with numerical calculations needed to determine the geometric prefactor because of the complicated details of the geometry. Instead, they report the bulk resistivity normalized to the room temperature resistivity, $\rho(T)/\rho(300K)$, because this can be found easily by the measured resistance ratio, $R(T)/R(300K)$. In most cases, the material can be identified as either a conductor or an insulator by extrapolating $\rho(T)/\rho(300K)$ to $T = 0$ K. When the material under investigation is purely a bulk conductor, the reporting of the resistance ratio is a useful practice. On the other hand, resistance ratios are meaningless for a 3D TI when the material has both surface and bulk conduction.

Electrical characterization of 3D TIs is challenging, as they are expected to have both bulk and surface conduction at finite temperatures. Resistance measurements from standard transport geometries do not provide information about the fraction of current flow through surface and bulk of the material. Furthermore, in situations where the surface conduction is significant, the bulk resistivity ratio, $\rho(T)/\rho(300K)$, cannot be obtained from using $R(T)/R(300K)$ because the prefactor now also changes with temperature. Therefore, the physics community should stop the practice of using resistance ratios in characterizing such materials.

4.3 Formalism for Resistance

In this section, we introduce a general formalism for understanding resistance measurements in an isotropic 3D material with both bulk and surface conduction, such as a 3D

topological insulator. In this formalism, any four-terminal resistance can be expressed in a suitable dimensionless function that depends on the ratio of the bulk and surface conductivities. We further consider this dimensionless function in two extreme regimes, $\sigma_b l \gg \sigma_s$ and $\sigma_b l \ll \sigma_s$, using a series expansion, where l is the characteristic length parameter. We will propose a generic transport geometry with a four-terminal resistance configuration that allows us to access the bulk conductivity even while the surface dominates the conduction.

4.3.1 Perturbative Approach of Scalable Resistance

In general, any resistance measurement, say R, of a 3D material is a function of the bulk (σ_b) and surface conductivity (σ_s) for a given transport geometry, i.e., $R = R(\sigma_b, \sigma_s)$. The bulk and surface conductivity have different units of $1/(\Omega \cdot \mathrm{m})$ and $1/\Omega$, respectively. The resistance can be rewritten in the following form:

$$R = \frac{1}{\sigma_s} f(x) \quad \text{and} \quad x = \frac{\sigma_b l}{\sigma_s}, \tag{4.1}$$

where $f(x)$ is a dimensionless function that depends on the current distribution for the transport geometry, and l is some characteristic length that depends on the transport geometry. The parameter, x, is also dimensionless, and it is defined by the ratio between σ_b and σ_s multiplied by l. Resistance is determined by the spatial dependence of the current or electrical potential of the transport geometry. This spatial dependence is uniquely determined by the boundaries, i.e., bulk/surface interface, and therefore the ratio between the surface and bulk conductivity determines $f(x)$. When x remains constant, R scales with either $1/\sigma_b$ or $1/\sigma_s$. In Eq. (4.1), we choose $1/\sigma_s$ so that the function $f(x)$ becomes a dimensionless function.

We have now expressed the resistance in a form that depends on σ_s and x, instead of on σ_b and σ_s. Expressing the resistance in the form of Eq. (4.1) is powerful when we consider a 3D topological insulator in two extremes: the bulk-dominated regime ($\sigma_b l \gg \sigma_s$) and the surface-dominated regime ($\sigma_b l \ll \sigma_s$). Both regimes can also be considered in the asymptotic limits of the dimensionless function, $f(x)$: the bulk-dominated regime can be studied in the $x \to \infty$ limit, and the surface-dominated regime can be studied in the $x \to 0$ limit.

In the bulk-dominated regime, the case when current flows mostly in the bulk, we can expand the function $f(x)$ in powers of $1/x$, $f(x) = C_{-1}(1/x) + C_{-2}(1/x)^2 + \cdots$, where C_{-1}, C_{-2}, ... are coefficients that depend on the geometry of the transport. The resistance is therefore:

$$R = \frac{C_{-1}}{\sigma_b l} + \frac{C_{-2}}{(\sigma_b l)^2}\sigma_s + \cdots . \tag{4.2}$$

The first order term in Eq. (4.2) only depends on the bulk properties, and this term usually

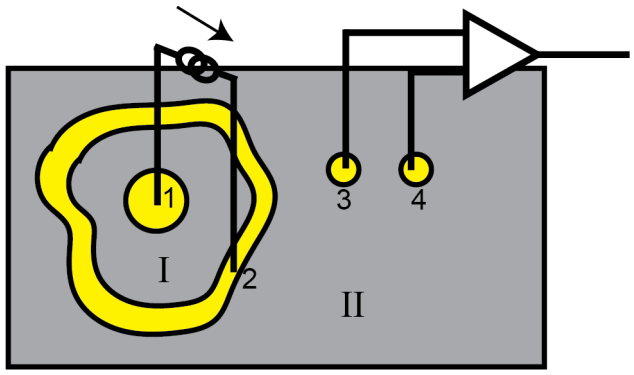

Figure 4.1: Schematic diagram of a generic inverted resistance measurement. In such a measurement, $R_{1,2;3,4}$, current lead 2 must fully enclose lead 1, and the voltage leads must be placed outside of the loop defined by lead 2. In preparation for submission to a journal [86].

overwhelms the higher order terms in resistance measurements of conventional transport geometries. The higher order terms, which contain σ_s, are therefore difficult to measure.

In the surface-dominated regime, the case when the current flows mostly on the surface, we can use the following asymptotic form $f(x) = C_0 + C_1 x + C_2 x^2 + \cdots$, where C_0, C_1, C_2, ... are coefficients. Thus, the resistance is:

$$R = \frac{C_0}{\sigma_s} + \frac{C_1}{\sigma_s^2}\sigma_b l + \cdots . \tag{4.3}$$

In Eq. (4.3), the first order term depends only on surface properties, and this term usually overwhelms the higher order terms in conventional transport measurements. Note that the bulk conductivity only arises in higher order terms. Although measuring the higher order terms is desirable for accessing the bulk conductivity, this is usually not possible in conventional transport measurements since the first term dominates.

Note that both asymptotic equations, Eq. (4.2) and Eq. (4.3), fail to cover the range near $x \approx 1$, which is the bulk-to-surface crossover regime, where the bulk and surface conduction are comparable. However, if the temperature dependence of σ_s is weak compared to σ_b, we can make use of the standard two-channel model that experimentalists conventionally use to cover this range. When the sample is sufficiently thin, the following relation holds for most conventional resistance geometries: $R \propto 1/(\sigma_s + \sigma_b l)$. This relation is useful in connecting the bulk and surface dominated regimes when extracting the bulk conductivity.

4.3.2 Inverted Resistance Measurement

In this subsection, we introduce a new non-local transport measurement that is extremely powerful for characterizing a 3D TI with a small bulk conductivity. The bulk conductivity can be extracted in the surface-dominated regime, $\sigma_b t \ll \sigma_s$ (for convenience we choose $l = t$, t is thickness), by totally suppressing the first order term (surface term) in Eq. (4.3).

This new transport measurement configuration consists of two current leads, one fully enclosing the other as shown in Fig. (4.1). Since the current contact 2 forms a closed loop, it separates the surface into two regions: I and II. Terminal 1 is in region I, terminal 2 is on the loop, and the other two terminals are in region II. We consider a resistance measurement in this transport geometry as the following: while passing current between terminal 1 and 2, the voltage is measured between terminals 3 and 4 (i.e., $R_{1,2;3,4} = V_{3,4}/I_{1,2}$). This defines the inverted resistance measurement.

Let us first consider what happens if we employ this geometry to characterize a two-dimensional electron gas or a thin film. When we connect leads 1 and 2 to the current source as shown in Fig. (4.1), current will flow only in region I. Here, the metallic loop (contact 2) would act like a two-dimensional Faraday cage blocking all the electric field from inside and thus there would be no current flow or electric field in region II. If the voltage leads are placed in region II, then $V_{3,4} = 0$. Because of this, such an inverted resistance measurement is not useful as $R_{1,2;3,4}$, would always be zero, regardless of the surface conductivity, and thus cannot be used to characterize a two-dimensional electron gas or thin film.

Because lead 2 acts as a Faraday cage only for the surface, if one employs this inverted resistance measurement on a bulk conductor, current will flow everywhere in the sample. Thus, one would expect a small but a measurable $V_{3,4}$. However, this geometry would not be used to measure bulk conductivity, since it would require numerical calculations of fringe fields and would not offer any benefits over conventional transport measurements.

On the other hand, in the case of a 3D TI, where one needs to characterize both surface and bulk conductivities, this type of inverted resistance measurement can provide information that cannot be accessed by conventional resistance measurements. To illustrate the power of this method when applied to a 3D TI, let us consider this measurement using the formalism introduced in the previous subsection. If the bulk conductivity is sufficiently low that the 3D TI is in the surface-dominated regime ($\sigma_b l \ll \sigma_s$), even for a sample with finite thickness, $R_{1,2;3,4}$ suppresses the leading order (surface term) term of Eq. (4.3), and therefore the second term dominates ($R \propto \sigma_b t/\sigma_s^2$). Notice that the second order term in Eq. (4.3) is proportional to the bulk conductivity.

To justify why the first term vanishes, let us first consider the case when $\sigma_b = 0$. In $\sigma_b = 0$, every term vanishes except the first term in Eq. (4.3). In Fig. (4.1), the loop

(terminal 2) must capture the entire current from terminal 1, since the surface is the only current path available. Inside region I, the electric potential drop is proportional to $1/\sigma_s$, whereas the entire region II must be equipotential to terminal 2 ($V = 0$ when grounded). Then, $V_{3,4} = 0$. Therefore, we find that $C_0 = 0$ in Eq. (4.3). When $\sigma_b \neq 0$, this resistance measurement, R_{Inv} (inverted resistance) can be written as:

$$R_{\text{Inv}} = 0 + \frac{C_1}{\sigma_s^2}\sigma_b t + \cdots . \tag{4.4}$$

Thus, we conclude that whenever a transport geometry on a 3D TI utilizes a closed loop on the surface, and the voltage is measured outside of that loop, then the highest order term (surface term) in Eq. (4.3) is suppressed and the next leading order term, which contains the bulk conductivity, dominates. Therefore, the inverted resistance measurement can be used to access the bulk conductivity in situations where the surface conduction dominates the bulk.

In this subsection, we have introduced the inverted resistance measurement, which provides the bulk conductivity information even in the presence of strong surface conduction. When we combine this inverted resistance measurement with conventional transport experiments, we can extract bulk and surface conductivities. In the following section, we introduce specific sample geometries and present the geometric factors that are found by numerical calculations. We also introduce strategies to implement the inverted resistance and the numerical results in experiment to extract the conductivities.

4.4 Transport Geometries for Inverted Resistance Measurements

Before we introduce transport geometries that allow inverted resistance measurements, we discuss a simple geometry, the Corbino disk, which employs a closed circular current loop shown in Fig (4.2) (a). To remind the reader of the standard Corbino disk measurement, the current flows from the center to the outer loop radially, and the voltages are measured either at the two current terminals (two-terminal resistance) or at two points within the transport region whose radii are r_{in} (inner radius) and r_{out} (outer radius) (four-terminal resistance). The two-terminal Corbino resistance measurement configuration is shown in Fig (4.2) (b). In a perfect 2D transport case, where current only flows on the surface ($\sigma_b = 0$ and $\sigma_s \neq 0$),

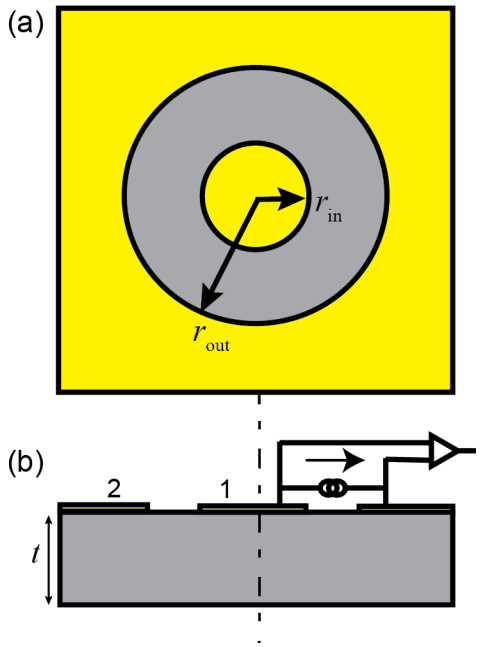

Figure 4.2: A standard two-terminal Corbino disk on a sample. (a) Top view: the sample is shown in gray and the highly conductive contacts are shown in yellow. (b) Side view: the current and voltage amplifier that is needed to perform the resistance measurements are connected to terminals 1 and 2. In preparation for submission to a journal [86].

the functional form of this standard resistance is well known:

$$R_{\text{Corbino}} = \frac{1}{2\pi} \ln(\frac{r_{\text{out}}}{r_{\text{in}}}) \frac{1}{\sigma_s}. \tag{4.5}$$

In the presence of both bulk and surface conduction ($\sigma_b \neq 0$ and $\sigma_s \neq 0$), the two-channel model is a good approximation for the standard Corbino resistance:

$$R_{\text{Corbino}} \approx \frac{1}{2\pi} \ln(\frac{r_{\text{out}}}{r_{\text{in}}}) \frac{1}{\sigma_s + \sigma_b \gamma}, \tag{4.6}$$

where γ is the effective thickness of the sample. γ depends on how the current flows in the defined geometry. We study numerically how the effective thickness changes as a function of true sample thickness by performing finite element analysis calculations using Comsol Multiphysics AC/DC module. The results from the bulk-dominated regime are shown in a solid blue line in Fig (4.3). In the thin sample limit, where the thickness of the sample is much smaller than both the inner radius and the annular region (surface transport region) of the Corbino disk ($r_{\text{in}} \gg t$ and $r_{\text{out}} - r_{\text{in}} \gg t$), γ approximates to the true thickness of the sample, t. In the very thick limit ($r_{\text{in}} \ll t$ and $r_{\text{out}} - r_{\text{in}} \ll t$), γ is independent of t.

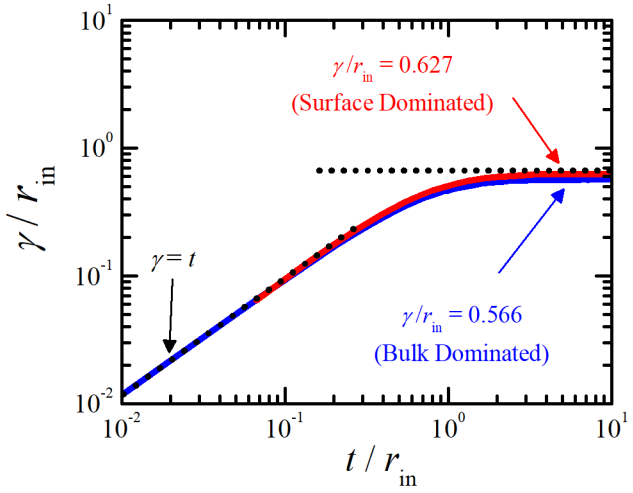

Figure 4.3: Effective thickness, γ, in the two-channel model vs. real sample thickness, t, for a standard Corbino disk. Both axes are divided by the inner radius ($r_{\text{in}} = 150$ μm). The solid red line is the numerical calculation in the surface-dominated regime when only the top surface contributes. When the thickness is very large, γ/r_{in} asymptotically approaches 0.627. The solid blue line is the numerical calculation in the bulk-dominated regime. At large thickness, γ/r_{in} asymptotically approaches 0.566. The effective thickness approaches to the true thickness of the sample when the sample thickness is sufficiently thin ($\gamma = t$). In preparation for submission to a journal [86].

It is important to note that for a given sample, the effective thickness can be slightly different in the bulk- or surface-dominated transport regimes. To illustrate this, we have performed a series of numerical calculations by adding a surface channel with a broad range of conductivity on the top surface of the sample. The result is shown in a solid red line, which is similar, but not identical, to the results of the bulk-dominated regime. In the very thick limit, the effective thickness is again independent of t, but with a value that is about 10% larger than that of the bulk-dominated regime. In the following subsections, continuing to use finite element analysis numerical calculations, we will consider different extensions of Corbino disk geometries that are suitable for inverted resistance measurements.

4.4.1 Single-Sided Four-Terminal Corbino disk

In this subsection, we consider a transport geometry consisting of a Corbino disk with two metallic rings in the annular region, as shown in Fig. (4.4). This transport geometry can be realized by a single step of lithography. The top view of the sample, the surface where the Corbino disk is patterned, is shown in Fig. (4.4) (a). On top of the sample surface (shown in gray), the transport geometry pattern is defined by highly conductive metal contacts such

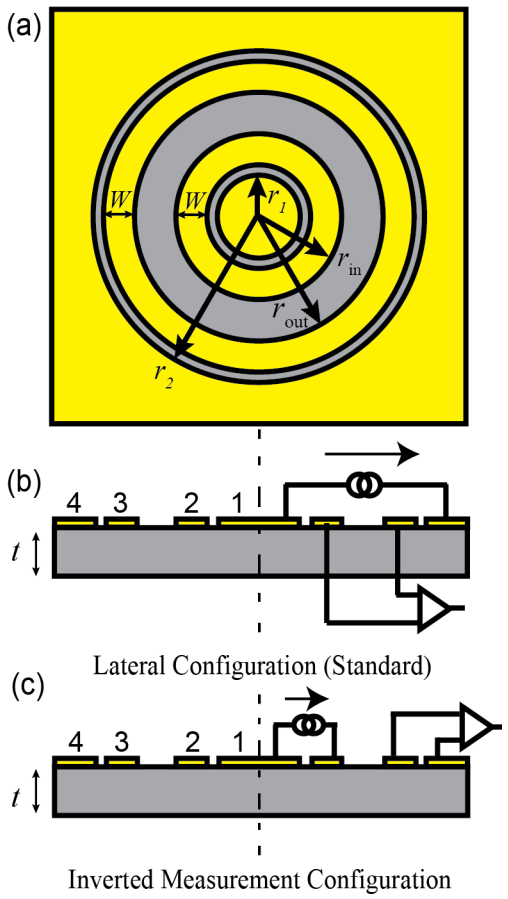

Figure 4.4: Four-terminal single-sided Corbino disk. The sample is shown in gray and the highly conductive contacts are shown in yellow. (a) Top view. (b) Side view and resistance configuration of the lateral configuration. (c) Side view and the resistance configuration of the inverted measurement configuration. We choose the dimensions: $r_1 = 100$ μm, $r_2 = 800$ μm, $r_{\text{in}} = 200$ μm, $r_{\text{out}} = 300$ μm, and $W = 75$ μm. In preparation for submission to a journal [86].

as gold (shown in yellow). In addition to the inner- (terminal 1) and outer- (terminal 4) circular metallic regions, there are two metallic rings (terminals 2 and 3), each with width, W. The side views of two different measurement configurations are shown in Fig. (4.4) (b) and Fig. (4.4) (c). In the lateral configuration shown in Fig. (4.4) (b), the resistance is measured by passing current between terminals 1 and 4 and measuring the voltage between terminals 2 and 3, i.e., $R_L = V_{2,3}/I_{1,4}$. This measurement is equivalent to the standard measurement of a conventional Corbino disk. In the inverted configuration shown in Fig. (4.4) (c), the resistance is measured by passing current between terminals 1 and 2 and measuring the voltage between terminals 3 and 4, i.e., $R_{\text{Inv}} = V_{3,4}/I_{1,2}$. Recall that $C_0 = 0$ in Eq. (4.4) in this inverted resistance measurement, and therefore $R_{\text{Inv}} = (C_1 t/\sigma_s^2)\sigma_b$.

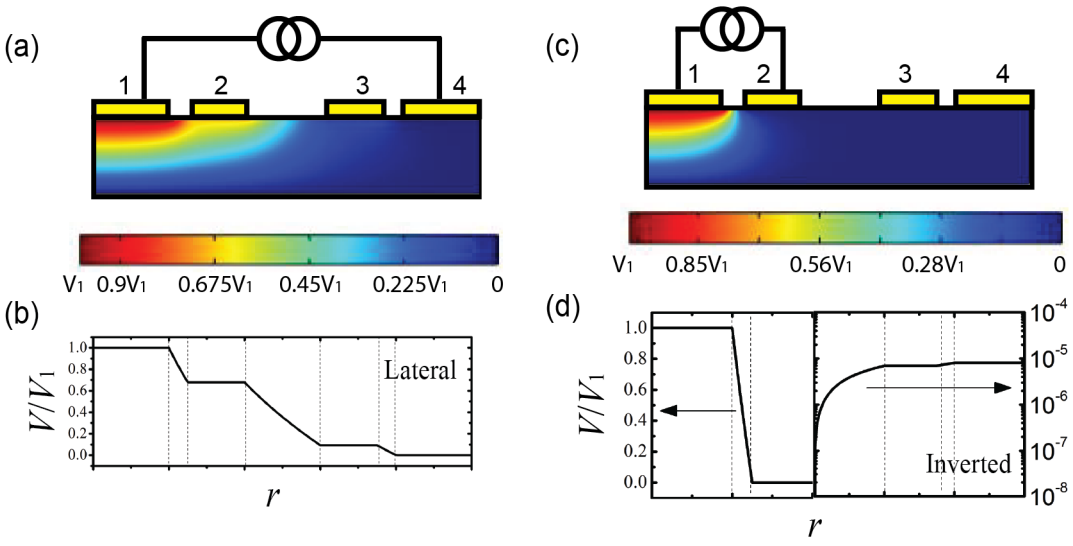

Figure 4.5: The potential distributions of the single-sided four-terminal Corbino disk. The bulk and on the surface is calculated in the surface-dominated transport regime ($\sigma_s \gg \sigma_b t$); t = 100 μm, σ_b=0.0013 1/(Ω·m), and σ_s = 0.005 1/Ω. The equipotential values are normalized by the potential at the current source (V_1). (a) Potential distribution in the bulk when the current is connected to the lateral configuration. (b) Potential distribution on the surface as a function of radial position when the current is connected to the lateral configuration. (c) Potential distribution in the bulk when the current is connected to the inverted configuration. (d) Potential distribution on the surface as a function of radial position when the current is connected to the inverted configuration. The surface region in $r < r_{\text{in}}$ is plotted in a linear scale, and $r > r_{\text{in}}$ is plotted in a logarithmic scale. In preparation for submission to a journal [86].

When the current flows only on the surface, the lateral resistance, R_L, is identical to Eq. (4.5). We rely on the numerical studies, using a finite element analysis software (Comsol Multiphysics AC/DC module), for the case when the current also flows in the bulk ($\sigma_b \neq 0$ and $\sigma_s \neq 0$). The numerical calculations are performed for a 100 μm thick sample for both resistance configurations (R_L and R_{Inv}). The solution of electrical potential resulting from the current flow in the lateral configuration is shown for the bulk and surface in Fig. (4.5) (a) and Fig. (4.5) (b), respectively. In Fig. (4.5) (a), the equipotential lines are coded in color. The bulk current flows normal to those equipotential lines. In Fig. (4.5) (b), on the surface, the potential drops from the source to the ground on the surface logarithmically, except for in the metallic ring region, where the potential remains constant.

For the inverted resistance measurement, the electrical potential that is calculated numerically is shown for the bulk and surface in Fig. (4.5) (c) and Fig. (4.5) (d), respectively. The inverted resistance is expected to be much smaller than the lateral resistance as it results

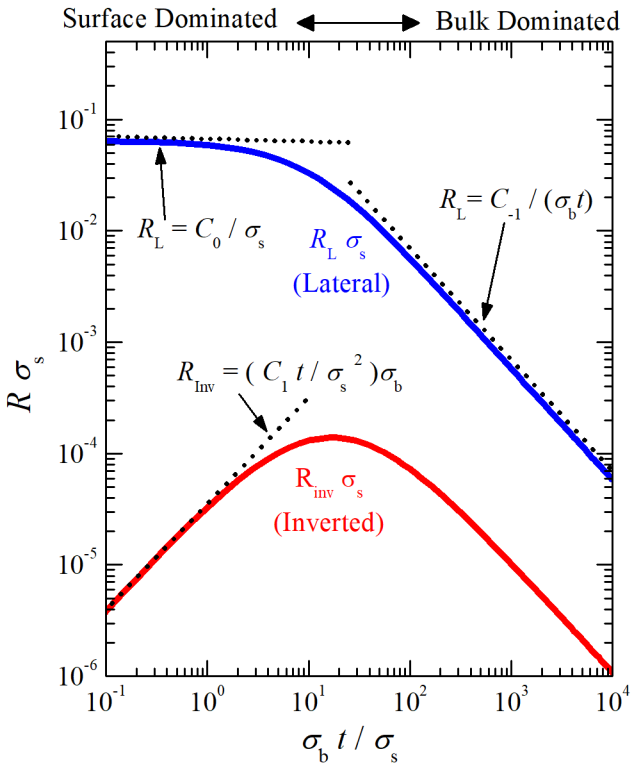

Figure 4.6: Example of numerical results of a single-sided Corbino disk. $R_L\sigma_s$ (blue) and $R_{\rm Inv}\sigma_s$ (red) as a function of x $(= \sigma_b t/\sigma_s)$ when $t = 1000$ μm. The dotted lines represent the asymptotic values from the first order term from Eq. (4.2), Eq. (4.3), and Eq. (4.4). In preparation for submission to a journal [86].

from the fringe field created near the outer part of the enclosed loop. The fringe fields are difficult to visualize in Fig. (4.5) (c). However, the effect from the fringes can be seen when the potential on the surface is plotted on a logarithmic scale, as shown in Fig. (4.5) (d). The plot indicates that the potential is gradually increasing as the distance from the terminal 2 ring increases.

We have performed these numerical calculations for different ratios of bulk to surface conductivity. In Fig. (4.6), we plot the dimensionless function, $f(x) = R\sigma_s$, for both the inverted $(R_{\rm Inv}\sigma_s)$ and the lateral resistance $(R_L\sigma_s)$ as a function of x $(= \sigma_b t/\sigma_s)$. Most importantly, we find that $R_L\sigma_s \propto 1/x$ when $x \to \infty$, and $R_{\rm Inv}\sigma_s \propto x$ when $x \to 0$. Therefore, in those two limits, the leading order terms in Eq. (4.2) and Eq. (4.4) dominate. Furthermore, the flat line in $R_L\sigma_s$ when $x \to 0$ agrees with Eq. (4.5) and the leading order term of Eq. (4.3) ($C_0 = 0.0645$ and $C_0 \gg C_1, C_2, \dots$).

By iterating the numerical calculations for different thicknesses, the transport coefficients, C_{-1} and C_1, are found as a function of thickness. Fig. (4.7) (a) shows the coefficient, C_{-1},

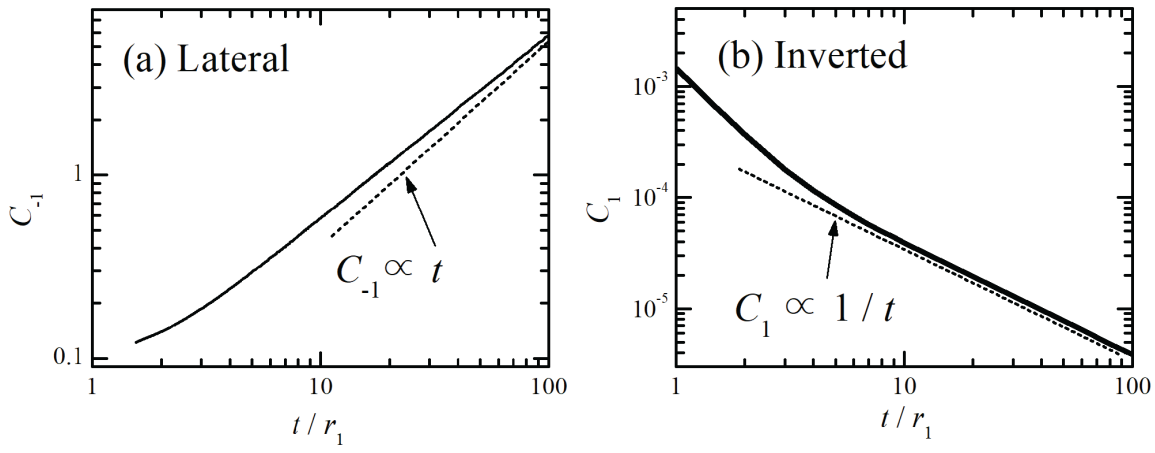

Figure 4.7: The transport coefficients for the single-sided four-terminal Corbino disk geometry as a function of sample thickness. (a) C_{-1} of the lateral resistance R_L in the bulk-dominated regime ($\sigma_b t \gg \sigma_s$). (b) C_1 of the inverted resistance R_{Inv} in the surface-dominated regime ($\sigma_s \gg \sigma_b t$). The thickness is dividing by r_1 ($= 100$ μm). The dotted lines indicate the transport coefficients when they are independent of thickness. In preparation for submission to a journal [86].

for the lateral measurement (R_L) in the bulk-dominated regime ($\sigma_b t \gg \sigma_s$) plotted as a function of dimensionless thickness (t/r_1). Fig. (4.7) (b) shows the coefficient, C_1, for the inverted measurement (R_{Inv}) in the surface-dominated regime ($\sigma_b t \ll \sigma_s$). Note that at very large thicknesses, $C_1 \propto 1/t$, and $C_{-1} \propto t$, which means the resistances become independent of thickness. In the following chapter, we will demonstrate this transport geometry on a SmB_6 sample, and use the results in Fig. (4.7) to find the bulk conductivity. In the following subsection, we consider a more advanced transport geometry design that results in a larger C_1 value and better confines the transport region.

4.4.2 Double-Sided Two-Terminal Corbino disks

In the previous subsection, we have considered a transport geometry defined on a single surface, and showed that the inverted resistance originates from the small fringe effects created near the enclosed loop. In this subsection, we consider a more advanced transport geometry, where we employ two coaxially aligned Corbino disks on opposite surfaces. We show that in this case, there is an inverted resistance measurement configuration that measures the current reaching the opposite surface, and this contribution can be much larger than the fringe effects on a single surface. Furthermore, since there are two Corbino disks placed on opposite surfaces, this geometry would allow us to measure the conductivity of

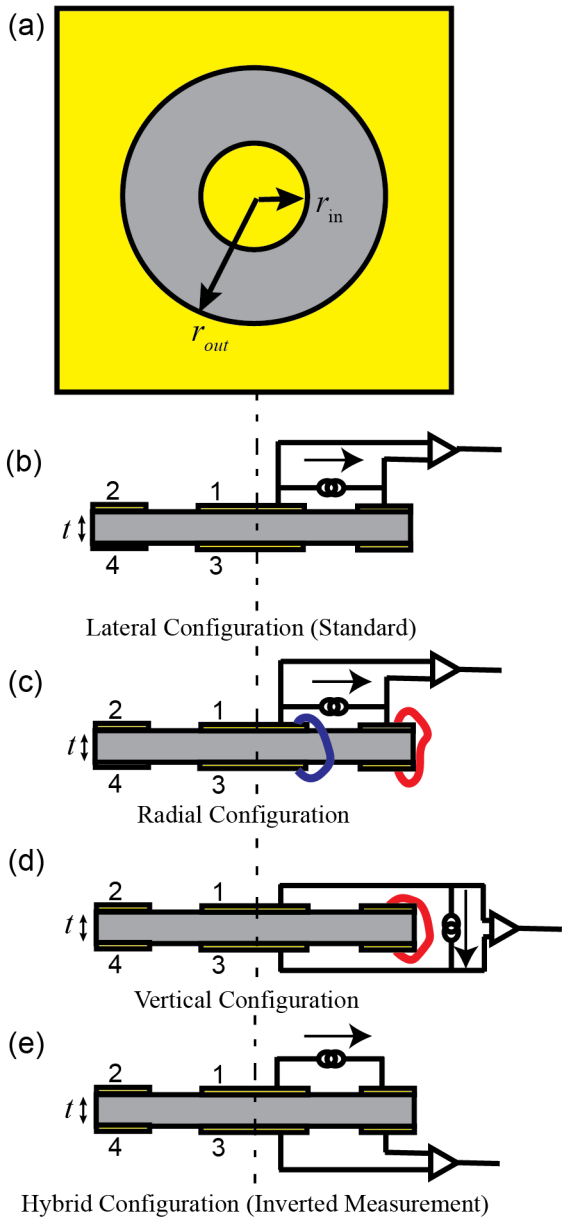

Figure 4.8: Double-sided two-terminal Corbino disk. The sample is shown in gray, and the highly conductive contacts are shown in yellow. (a) Top and bottom surface view. (b) Side view and the lateral resistance configuration. (c) Side view and the radial resistance configuration. The blue and red lines are jumper wires. (d) Side view and the vertical resistance configuration. (e) Side view and the hybrid resistance configuration. The hybrid measurement is an inverted resistance measurement in the surface-dominated regime ($\sigma_s \gg \sigma_b t$). We choose the Corbino dimensions as $r_1 = 150$ μm and $r_2 = 300$ μm. In preparation for submission to a journal [86].

both surfaces. This can also be a powerful geometry for characterizing a wide range of 3D topological insulators in which the contribution of conducting surface states has not been studied yet.

A schematic diagram of the coaxially-aligned double Corbino disk geometry is shown in Fig. (4.8). This transport geometry can be realized by two steps of lithography performed on opposite sides of the sample. One surface (since both surfaces are identical) of the sample is shown in Fig. (4.8) (a). The disk shapes are defined by highly conductive metal contacts (shown in yellow) used as terminals for resistance measurements. We note that the measurement configurations that will be discussed in the following will include both two- and four-terminal resistance measurements.

The two-terminal resistance measurements where the current and voltage leads share the same terminal should only be used when the contact resistances are negligible. One example of the two-terminal resistance measurement is shown in Fig. (4.8) (b), where resistance is measured between the inner-metallic circle (terminal 1) and the outer-metallic region (terminal 2), or $R_L = V_{1,2}/I_{1,2}$. When the current flows only on the surface ($\sigma_b = 0$ and $\sigma_s \neq 0$), this is identical to Eq. (4.5): $R_L = R_{\text{Corbino}}$.

The two-terminal resistance can also be measured using both the top and bottom Corbino disks in parallel using the radial configuration as shown in Fig. (4.8) (c). In the radial configuration, terminals 1 (2) and 3 (4) are connected with a low resistance jumper wire shown in blue (red). These jumper wire connections ensure that the top and bottom surfaces have identical electric potential profiles. In addition, the wire that connects terminals 2 and 4 (shown in red) prevents the current from flowing on the side surfaces of the sample. When $\sigma_b = 0$ and $\sigma_s \neq 0$, the radial resistance is equivalent to two resistors, corresponding to each Corbino lateral resistance measurement, connected in parallel:

$$R_R = \frac{1}{2} \times \frac{1}{2\pi} \ln(\frac{r_{\text{out}}}{r_{\text{in}}}) \frac{1}{\sigma_s}. \tag{4.7}$$

Another two-terminal resistance measurement, which we will call the vertical configuration, can be performed on such a device as shown in Fig. (4.8) (d). This configuration also shorts terminals 2 and 4 with a low resistance jumper wire (shown in red), which eliminates the current flow on the side surfaces. The vertical resistance is measured between the two inner-metallic circles, or $R_V = V_{1,3}/I_{1,3}$. In the bulk-dominated regime ($\sigma_b t \gg \sigma_s$), the current chooses a vertical path through the bulk between the two circular plates 1 and 3. In the surface-dominated regime ($\sigma_b t \ll \sigma_s$), the current flows first radially on the surface through the top Corbino disk, then passes through the jumper wire, and finally converges radially through the bottom Corbino disk. The approximate functional forms of resistance can be

found in those two limits. In the $\sigma_b t \gg \sigma_s$ case, R_V can be found by a derivation analogous to finding the capacitance between two parallel plates. If the sample is thin, we can assume the current density is in the vertical direction and uniform in the region of center contacts, so the resistance is:

$$R_V \approx \frac{t}{\pi r_1^2}\frac{1}{\sigma_b}, \tag{4.8}$$

where t is the thickness of the sample. In the other extreme, $\sigma_b t \ll \sigma_s$, we can regard each Corbino disks as resistors that are connected in series:

$$R_V = 2 \times \frac{1}{2\pi}\ln(\frac{r_{\text{out}}}{r_{\text{in}}})\frac{1}{\sigma_s}. \tag{4.9}$$

Especially in the vertical measurement, because R_V can be dramatically different in the two extremes, $\sigma_b t \gg \sigma_s$ and $\sigma_b t \ll \sigma_s$, and can be evaluated without numerical simulations, this configuration can provide strong evidence for experiments that are in the stage of verifying the existence of the surface states.

The last configuration that we consider is a four-terminal measurement, which we will call it the hybrid resistance measurement, as shown in Fig. (4.8) (e). In the hybrid configuration, the current flows between terminals 1 and 2, and the voltage is measured using terminals 3 and 4, which are on the opposite side, i.e., $R_H = V_{3,4}/I_{1,2}$. Since current lead 2 fully encloses lead 1, the hybrid resistance is an inverted resistance measurement. Because of the proximity of the voltage and current contacts, the inverted resistance signal in this double-sided device is expected to be much larger than that of the single-sided inverted resistance measurement discussed previously.

We have solved this geometry numerically for different resistance configurations using finite element analysis (Comsol Multiphysics AC/DC module). In Fig. (4.9), we plot the dimensionless resistance f $(= R\sigma_s)$ for all four resistances as a function of x $(= \sigma_b t/\sigma_s)$. Indeed, as we expect, our hybrid resistance results in, $R_H\sigma_s \propto x$ when $x \to 0$ in the inverted resistance measurement. In the opposite limit when $x \to \infty$, $R\sigma_s \propto 1/x$ for all four resistances as expected. In particular, $R_V\sigma_s$ approaches to Eq. (4.9). Furthermore, the asymptotic flat lines in $R_L\sigma_s$, $R_R\sigma_s$, and $R_V\sigma_s$ when $x \to 0$ agrees with Eq. (4.5) ($C_0 = 0.0645$), Eq. (4.7) ($C_0 = 0.032$), and Eq. (4.9) ($C_0 = 0.129$), respectively.

We have also solved C_{-1} and C_1 iteratively for different thicknesses. In Fig. (4.10), we present our results for C_{-1} and C_1 as a function of dimensionless thickness (t/r_1). In experiments, R_L, R_R, and R_V may suffer from the presence of contact resistances. To address this potential problem, we present C_{-1} from the R_H, which is a four-terminal measurement. Comparing to Fig. (4.10) (a) and Fig (4.7) (a), when the sample is thin ($t < r_1$), C_1 from the hybrid measurement is a few orders of magnitude larger than the inverted measurement

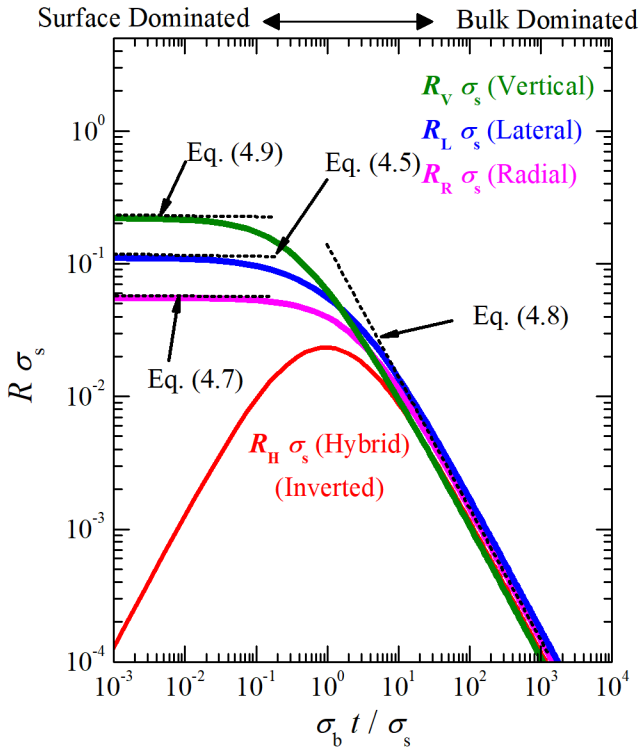

Figure 4.9: Example of numerical results for a two-terminal double-sided Corbino disk. Numerical result of $R_L\sigma_s$ (blue), $R_R\sigma_s$ (magenta), $R_V\sigma_s$ (green) and $R_{\mathrm{Inv}}\sigma_s$ (red) vs. x $(= \sigma_b t/\sigma_s)$ when the thickness is $t = 100$ μm. The dotted lines indicate the asymptotic values from the equations. In preparation for submission to a journal [86].

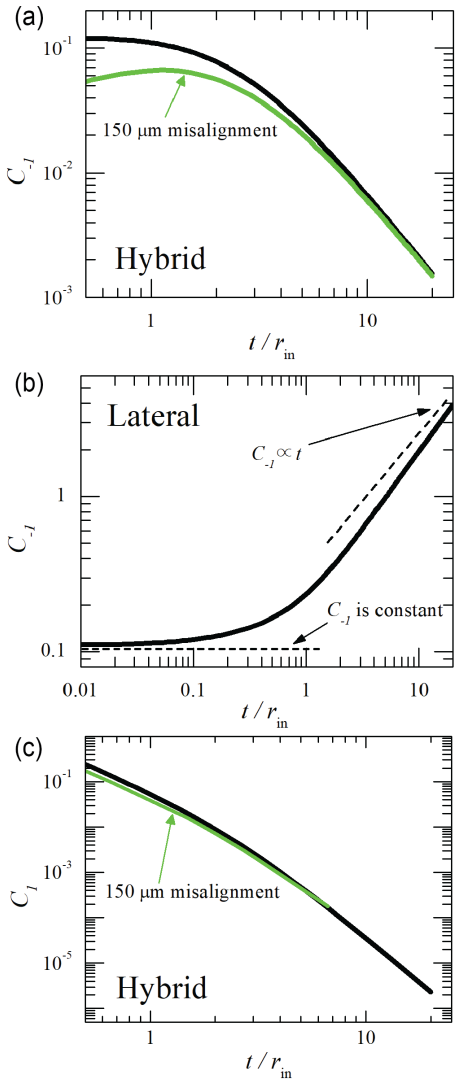

Figure 4.10: The transport coefficients for the double-sided two-terminal Corbino disk geometry by varying the sample thickness. The solid black line shows the transport coefficient when the two Corbino disks are coaxially aligned, and the solid green line shows the transport coefficients when the two Corbino disks are misaligned by 150 μm. The thickness is expressed in a dimensionless form by dividing by r_{in} (= 150 μm). (a) C_{-1} of the hybrid resistance, R_H, in the bulk-dominated regime ($\sigma_b t \gg \sigma_s$). (b) C_{-1} of the lateral resistance, R_L, in the bulk-dominated regime ($\sigma_b t \gg \sigma_s$). (c) C_1 of the hybrid resistance, R_H, in the surface-dominated regime ($\sigma_s \gg \sigma_b t$). In preparation for submission to a journal [86].

from the single-sided 4-terminal Corbino disk case. Therefore, this transport geometry can be better in extracting a smaller bulk conductivity.

However, there can be a practical difficulty when preparing a double-sided transport geometry: the two Corbino disks may be misaligned. This type of misalignment would be expected to change the values of C_{-1} and C_1. To understand how the misalignment impacts the resistance measurements, we have repeated the calculations for the case where there is a 150 μm misalignment between the top and bottom Corbino disks. The coefficients C_{-1} and C_1 calculated with such a misalignment are shown in green. Our numerical calculations indicate that the hybrid resistance measurement is most vulnerable to misalignment. In the following subsection, we consider a transport geometry that allows similar measurements, but all four measurements are in a 4-terminal configuration.

4.4.3 Double-Sided Four-terminal Double Corbino Disk

The single-sided four-terminal Corbino disk geometry (in subsec. 4.4.1) has the limitation in that the R_{Inv} may be too small to measure in the surface-dominated regime ($\sigma_b t \ll \sigma_s$). The coaxially aligned double Corbino disk geometry (in subsec. 4.4.2) can give a larger magnitude from the R_H if the sample is thin, but the other three resistances (R_L, R_R, and R_V) may suffer from contact resistances in the bulk-dominated regime ($\sigma_b t \gg \sigma_s$). In this subsection, we consider a transport geometry that incorporates advantages of the two geometries, so that both issues can be eliminated. The configuration consists of two coaxially aligned four-terminal Corbino disks placed on both sides of the sample as illustrated in Fig. (4.11). The advantages of having multiple leads on both sides should be clear: we now have more than enough 4-terminal resistance configurations, including inverted measurements, that can be used to extract the bulk conductivity. Even without using any jumper wires, such an 8-terminal transport geometry would allow us to perform a total of 70 independent inverted resistance measurements. We will only discuss a few that are similar to what was discussed in the previous sections. In addition, we will provide an example of how to apply a ratio method to extract the two conductivities.

A schematic diagram of the sample is shown in Fig. (4.11) (a). The disk shapes are defined by highly conductive metal contacts (shown in yellow). This type of sample can be realized by two separate steps of lithography. The conductive metal regions are used as terminals for resistance measurements. We choose the dimensions of the Corbino disks with two rings to be identical to the earlier Corbino disk structure shown in Fig. (4.4). Therefore, the single-sided 4-terminal Corbino disk results can be used for this geometry as well. Because of this, we will omit the resistance configurations that uses contacts from a

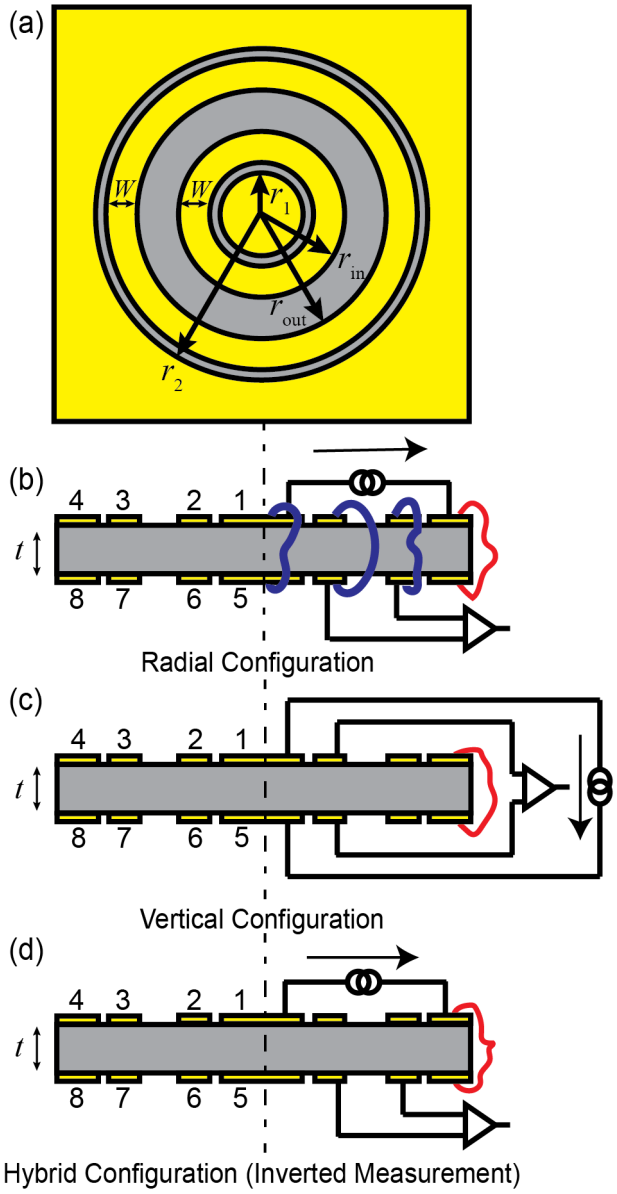

Figure 4.11: Four-terminal double-sided Corbino disk. The sample is shown in gray and the highly conductive contacts are shown in yellow. (a) Top and bottom view of the sample. (b) Side view of the sample and the radial configuration. (c) Side view of the sample and the vertical configuration. We choose the Corbino disk dimensions identical to the single-sided four-terminal Corbino disk shown in Fig. (4.4): $r_1 = 100$ μm, $r_2 = 800$ μm, $r_{in} = 200$ μm, $r_{out} = 300$ μm, $W = 75$ μm. In preparation for submission to a journal [86].

single side, and instead, we will discuss three new measurement configurations that require the contacts from both top and bottom surfaces.

We first discuss the radial measurement configuration (R_R) shown in Fig. (4.11) (b). Terminal pairs of (1, 5), (2, 6), and (3, 7) are connected with a low-resistance jumper wire shown in blue. These jumper wire connections help to enhance the radial flow of current in the bulk. In addition, the wire that connects terminals 4 and 8 (shown in red) prevents the current from flowing on the side surfaces of the sample. When the current only flows on the surface ($\sigma_s \neq 0$ and $\sigma_b = 0$), the radial resistance is:

$$R_R = \frac{1}{2}R_L = \frac{1}{2} \times \frac{1}{2\pi} \ln(\frac{r_{\text{out}}}{r_{\text{in}}})\frac{1}{\sigma_b}, \tag{4.10}$$

where R_L is the lateral resistance that was introduced in Eq. (4.5).

Next, we consider the vertical configuration shown in Fig. (4.11) (c). Similar to the radial configuration, terminals 4 and 8 are connected with a low resistance jumper wire shown in red in order to eliminate the current flowing on the side surfaces. In the bulk-dominated regime ($\sigma_b t \gg \sigma_s$), current flows mostly vertically through the bulk. The resistance is thickness dependent and can be expressed in the form of $R_V \sigma_s \approx C_{-1}(\sigma_b t/\sigma_s)^{-1}$, which is the leading order term of Eq. (4.2). In the surface-dominated regime ($\sigma_b t \ll \sigma_s$), where the current flows mostly on the surfaces, first the current flows radially outwards on the top surface, and then the current flows to the other surface through the jumper wire and converges radially inwards. In this case, we can regard every possible conduction path of the Corbino disks as a resistor and add them in series:

$$R_V = 2 \times \frac{1}{2\pi} \ln(\frac{r_{\text{out}}}{r_{\text{in}}}\frac{r_2}{r_1}\frac{r_{\text{in}} - W}{r_{\text{out}} + W})\frac{1}{\sigma_s}. \tag{4.11}$$

For the hybrid configuration, as shown in Fig. (4.11) (d), while terminals 4 and 8 are connected with a low resistance jumper wire (shown in red) to ensure that the side surface contribution is eliminated, the current leads are connected to terminals 1 and 4, and the voltage leads are connected to terminals 6 and 7, i.e., $R_H = V_{6,7}/I_{1,4}$. When the current chooses its path mostly on the surface ($\sigma_b t \ll \sigma_s$), this is indeed the inverted measurement in that the Corbino disk on the top surface corresponds to the enclosed loop that captures the current flowing on the surface and the bottom Corbino disk corresponds to the voltage measurement external to that loop and measures the current path contributing from the bulk.

Similar to the previous transport geometries discussed above, we calculated the relevant transport coefficients for this sample geometry numerically using finite element analysis

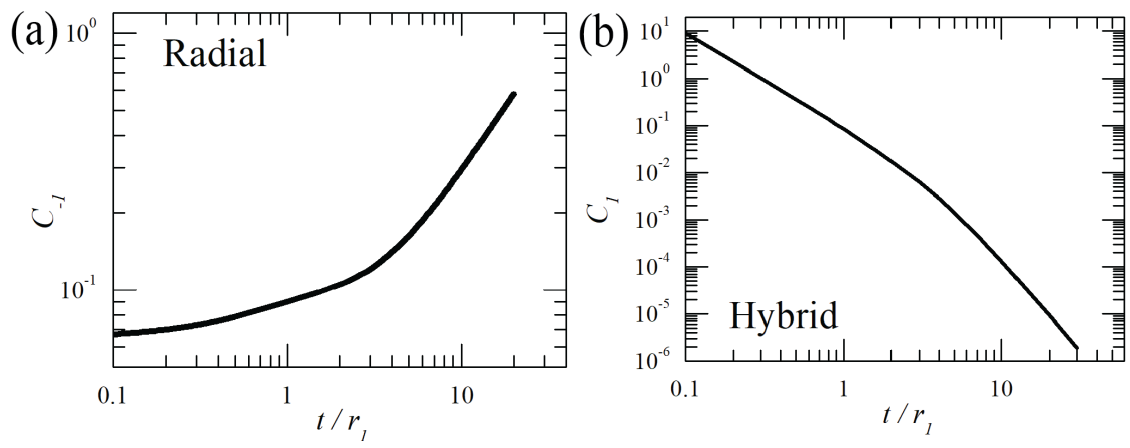

Figure 4.12: Transport coefficients for the four-terminal double Corbino disk geometry at different thicknesses. (a) C_{-1} for the radial resistance, R_R, in the bulk-dominated regime ($\sigma_b t \gg \sigma_s$). (b) C_{-1} for the hybrid resistance, R_H, in the surface-dominated regime ($\sigma_b t \gg \sigma_s$). The thickness is expressed in a dimensionless form by dividing by r_1 (= 100 μm). In preparation for submission to a journal [86].

(Comsol Multiphysics AC/DC module). We present C_1 for the hybrid measurements and C_{-1} for radial measurements as a function of thickness in Fig. (4.12). If the top and bottom Corbino rings are significantly coaxially misaligned, we recommend using C_{-1} from the lateral measurements (Fig. (4.7) (a)) instead of using C_{-1} from the radial measurement.

4.5 Solution for Anisotropic Bulk

The work in this chapter so far has been done under the assumption that the bulk conductivity is isotropic. Although not related to SmB_6, which is a cubic crystal and can be regarded as having an isotropic bulk conductivity, we will discuss the possibility of expanding this study on materials with anisotropic bulk conductivity. We know that many 3D topological insulators are in fact anisotropic in such a way that the material has a different conductivity in one specific crystal direction. If we prepare a double-sided Corbino disk sample where the axis is aligned with that specific direction, then in principle, we can use the bulk conductivity measurement strategies developed in the previous sections by theoretically mapping the anisotropic sample to an isotropic sample with a different thickness.

For a material with anisotropic bulk conductivity, we define the direction that is tangential to the surface as r, and normal to the surface as z. We also define σ_{tn} as the bulk conductivity tangential to the surface, and σ_n as the bulk conductivity normal to the surface.

Then, the potential in the bulk is determined by

$$\sigma_{tn}\frac{\partial^2 V}{\partial r^2}+\sigma_n\frac{\partial^2 V}{\partial z^2}=0, \tag{4.12}$$

with the appropriate boundary conditions at the interface of bulk and surface. By redefining the normal direction, z, to $\zeta=\sqrt{\sigma_{tn}/\sigma_n}z$, we can re-write Eq. (4.12) as:

$$\frac{\partial^2 V}{\partial r^2}+\frac{\partial^2 V}{\partial \zeta^2}=0, \tag{4.13}$$

Thus, we have mapped our problem into an isotropic bulk conductivity case. When we map the problem as above, the thickness of the sample, t, is also mapped to a different thickness, τ, with the relation: $\tau=\sqrt{\sigma_{tn}/\sigma_n}t$.

σ_{tn} can be found if we know the correct $C_1(\tau)$ and $C_{-1}(\tau)$ values. If τ is not found correctly, σ_{tn} in the surface-dominated regime and the bulk-dominated regime will be mismatched. If we start with the bulk conductivity from $C_1(t)$ and $C_{-1}(t)$, which is mismatched initially, and change those values to $C_1(\tau)$ and $C_{-1}(\tau)$, where the bulk conductivity in two regimes are continuous, this corresponds to σ_{tn}. Finally, σ_{tn} and τ can be used to find the bulk conductivity in the normal direction:

$$\sigma_{tn}=\sigma_n(\frac{t}{\tau})^2. \tag{4.14}$$

However, we should warn the reader that this strategy for anisotropic conductivities can only be useful for samples that are prepared with extremely high precision. As we have learned from our transport measurements on SmB_6 samples, a mismatch between the bulk conductivity extracted from bulk- and surface-dominated regimes using different 4-terminal resistance measurements can easily occur because of small imperfections in the transport geometries.

4.6 Conclusion

In this chapter, we have introduced our newly invented transport method, the inverted resistance measurement, that can measure the bulk conductivity below the bulk-to-surface crossover temperature. After explaining how the inverted resistance works with the resistance formalism for two conducting channels, we have also introduced various transport geometries that utilize the inverted resistance. In the following chapter, we realize this new measurement on SmB_6 samples experimentally. Also, with this new transport method, we will report some

of our systematic studies on disordered SmB_6 samples to understand the bulk behavior.

Chapter 5

Realizing the Inverted Resistance Experimentally

5.1 Introduction

[1]In the previous chapter, we showed how the inverted resistance method works based on our resistance formalism for a 3D TI (Eq. (4.1)). We also discussed several transport geometries that utilize this inverted resistance measurement.

In this chapter, we will realize some of the transport geometries on SmB_6, and verify usefulness and strength of our new invention. Previous transport experiments indicate that the bulk resistivity of SmB_6 is activated in the form of $R \propto \exp(E_a/k_BT)$, with an activation energy, E_a, of about 3 – 4 meV. The activated behavior of the bulk transport is difficult to study using standard transport experiments below 4 K because at that temperature, current starts to flow mostly through the surface. In contrast, inverted resistance measurements can be used to measure the bulk conductivity of SmB_6 at temperatures below 4 K. Our demonstrations, which will be presented in this chapter, show that the activated behavior continues below 4 K. In the following chapter, we will use this new method for further studies of the bulk of SmB_6.

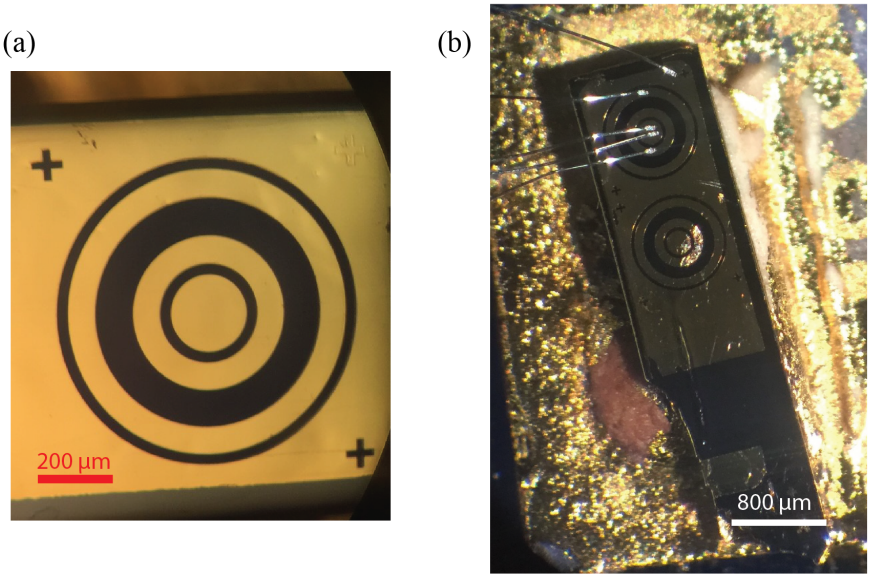

Figure 5.1: Pictures of the single-sided four-terminal Corbino disk on SmB_6. (a) Focused view of Corbino disk before wires are connected. (b) Entire view of the sample. In preparation for submission to a journal [86].

5.2 Single-Sided Four-Terminal Corbino Disk on SmB_6

5.2.1 Sample Preparation

We prepared a transport geometry on a polished SmB_6 surface using the dimensions shown in Fig. (4.4). The SmB_6 crystal used in this study was grown in an aluminum flux. The grown crystal was first thinned with a SiC polishing pad that has grit size of 15.3 μm. It was then polished with a SiC polishing pad of 2.5 μm. Fine polishing was performed on polishing cloth (TexMet C) using an aluminum oxide slurry with a particle size of 0.3 μm. After cleaning the surface with diluted HCl, we performed photolithography on the polished surface with a mask design of the 4-terminal Corbino disk pattern. We exposed the surface where we wanted to evaporate a highly conductive metal and covered it with photoresist on the regions that we want to expose later. We then evaporated Ti/Au 20 Å/1500 Å, and lifted off the photoresist in acetone. The sample was cleaned again with diluted HCl and then attached to a silicon piece with an insulating SiO_2 layer using Torrseal. We used a wire bonder to attach aluminum wires (1 mil) to the terminals. We performed low-frequency resistance measurements at temperatures ranging from 16 to 1.7 K using the quantum design

[1]This work has been posted on ArXiv [86]. The author and his collaborators are preparing a manuscript for submitting to a peer-reviewed journal that will contain contents in this chapter.

PPMS system connected to an external lock-in amplifier (SR830). The prepared sample is shown in Fig. (5.1)

5.2.2 Experimental Results

The experimental results, plotted as resistance vs. temperature, are shown in Fig. (5.2) (a). As temperature is decreased from 16 K, both the lateral resistance, R_L (shown in blue), and the inverted resistance, R_{Inv} (shown in red), increases. In this temperature range, the sample is in the bulk-dominated regime ($\sigma_b t \gg \sigma_s$). Then around 3.5 K, R_{Inv} reaches a peak and starts to decrease, while R_L plateaus. The sample at this low temperature is in the surface-dominated regime ($\sigma_b t \ll \sigma_s$). According to Eq. (4.5), the surface conductivity is $\sigma_s = 3.3 \times 10^{-4}$ S. Meanwhile, R_{Inv} continuously drops toward 0 until it is too noisy to measure. The resolution of our electronics allowed us to measure R_{Inv} down to ~2.5 K.

To extract the bulk conductivity from the data in Fig. (5.2) (a), we use leading order terms in the series expansion in the surface- and bulk-dominated regimes (Eq. (4.2) – Eq. (4.4)), and the two-channel model (Eq. (4.6)). For each temperature range, we converted the resistance measurements to bulk conductivity as described in the following.

High temperature range (bulk-dominated regime): At temperatures above ~3.6 K, the lateral resistance can be used to find the bulk conductivity. In this bulk-dominated regime ($\sigma_b l \gg \sigma_s$), Eq. (4.2) can be used to understand the resistance behavior (we replaced l with thickness, t). The contribution of the current that flows on the surface is extremely small, so we keep only the first order term. With this first order term, and using C_{-1} found in Fig. (4.7) (a), the bulk conductivity is:

$$\sigma_b(T) = \frac{C_{-1}}{t}\frac{1}{R_L(T)}. \tag{5.1}$$

The result is shown in Fig. (5.2) (b) as a solid blue line.

Intermediate temperature range (bulk-to-surface crossover regime): In the temperature range, 3.3 - 3.6 K, the sample undergoes a bulk-to-surface crossover, so the bulk and surface conductions are comparable. This regime is where the expansion of the $f(x)$, cannot be expanded in series in either extremes of x because $x \approx 1$. Instead, we make use of Eq. (4.6) from the two-channel model to convert R_L to bulk conductivity. This can be re-formulated as:

$$\sigma_b(T) = \frac{1}{\gamma}\left(\frac{C_0}{R_L(T)} - \sigma_s\right). \tag{5.2}$$

The result is shown in Fig. (5.2) (b) as a solid green line. We have shown in Fig. (4.3) that the calculated effective thickness is slightly different for the bulk-dominated and the surface-

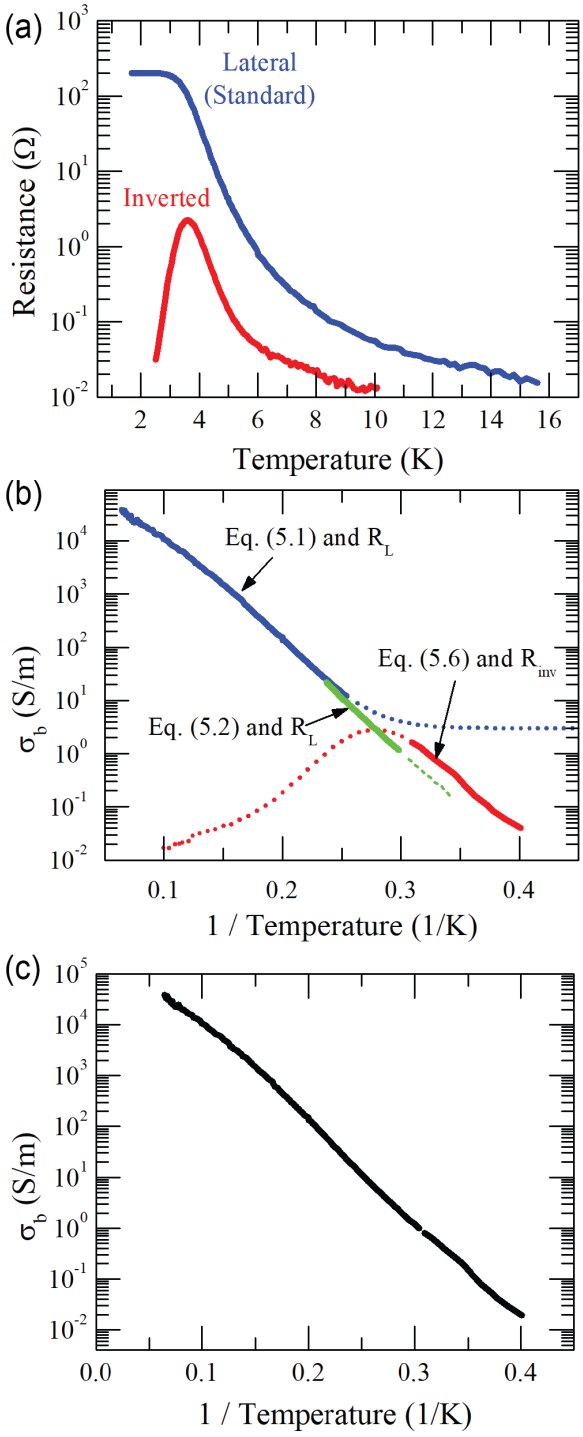

Figure 5.2: Experimental results and bulk conductivity analysis on a single-sided 4-terminal Corbino disk on a SmB_6 sample with thickness, $t = 300$ μm. (a) Resistance vs. temperature of the lateral and inverted measurements. (b) The bulk conductivity converted from the measured resistance. The dotted lines indicate the bulk conductivity conversion applied beyond the appropriate regime. (c) The result of the extracted bulk conductivity after adjustment of mismatch. In preparation for submission to a journal [86].

dominated regimes. In this particular experiment, we estimate the effective thickness from $\gamma = C_0 t/C_{-1}$. It is fortunate that the temperature dependence of the surface conductivity in SmB_6 is weak enough that it can be approximated as constant.

We warn the reader that Eq. (5.2) should not be used alone in samples with a surface conductivity that is strongly temperature dependent. For characterizing such a material, in this intermediate temperature range, it is important to use multiple four-terminal resistance measurements that put different emphasis on surface and bulk conductivity, Luckily the double-sided Corbino geometry allows one to perform a vertical measurement (R_V), which would put greater emphasis on bulk conductivity. Thus, the combination of lateral and vertical measurements may provide a better strategy for extracting the bulk conductivity in this temperature regime.

We expect that the process of extracting the conductivities from the measured resistances would have been much more challenging if the surface conductivity was also strongly temperature dependent. In such a case, the full numerical simulation must be done and then compared to the measured resistances.

According to Eq. (4.1), one can measure the resistance, R, easily, but not $f(x)$ if σ_s has a strong temperature dependence. One may implement an approach that would rely on the ratios of the two different resistance measurements. For example, if we take the ratio of the conventional resistance, R_C, to the inverted resistance, R_{Inv}, we can directly compare to the ratios of the dimensionless functions, $f(x)$, of the corresponding resistances, $f_C(x)$ and $f_{\text{Inv}}(x)$:

$$\frac{R_C}{R_{\text{Inv}}} = \frac{f_C}{f_{\text{Inv}}} = h(x). \tag{5.3}$$

where the $f_C(x)$ is the dimensionless resistance for R_C, $f_{\text{Inv}}(x)$ is the dimensionless resistance for R_{Inv}, and we define the ratio as $h(x)$. From Eq. (5.3), we can compare the experimental data and numerical results directly, and find x. The surface conductivity can then be found by:

$$\frac{R_C}{f_C} = \frac{1}{\sigma_s} \quad \text{or} \quad \frac{R_{\text{Inv}}}{f_{\text{Inv}}} = \frac{1}{\sigma_s}. \tag{5.4}$$

After σ_s is found, σ_b can be found from x that was found from Eq. (5.3):

$$\sigma_b = \frac{\sigma_s x}{t}. \tag{5.5}$$

Low temperature range (surface-dominated regime): For temperatures below ~3.3 K, the sample is in the surface-dominated regime. The inverted resistance measurement can be used at this temperature range to extract the bulk conductivity. In the surface-dominated regime, the inverted resistance can be expressed by Eq. (4.4). C_1 can be found from Fig. (4.7) (b), and

σ_s can be found from Eq. (4.5) and the plateau value of $R_L(T)$. Then the bulk conductivity is:

$$\sigma_b(T) = \frac{\sigma_s(T)^2}{t}\frac{R_{\text{Inv}}}{C_1}. \tag{5.6}$$

The result is shown in Fig. (5.2) (b) as a solid red line.

Notice that there is a noticeable mismatch of about a factor of ∼3 between the two plots (solid blue line and the solid red line) near the bulk-to-surface crossover in Fig. (5.2) (b). We have also tested five other SmB_6 samples, and found mismatch factors ranging from 0.85– 3.5. The mismatch indicates that the geometric coefficients (C_{-1}, C_1, etc.) do not correspond to the actual sample geometry. There are numerous possibilities that may have caused this mismatch. For SmB_6, one should worry about the quality difference between the top and bottom surface. This can greatly influence the inverted resistance measurement since the $R_{\text{Inv}} \propto 1/\sigma_s^2$. Aluminum inclusions that are known to be possibly present in flux grown samples can influence the current path in the bulk, and result in a different geometric coefficient.

Even in the case where the top and bottom surfaces have identical transport properties and the sample is free from inclusions, a slight difference of dimensions between the realized sample geometry and the numerically-simulated geometry can result in a large mismatch as above, especially for the inverted resistance measurement. The inverted resistance measurement depends greatly on the fringe currents in the bulk, and measurements that involve these current paths are highly sensitive to the details of the geometry. For example, a similar discrepancy also occurs in conventional transport geometries such as van der Pauw measurements. In van der Pauw measurements performed on cleaved square samples, they typically result in different 4-terminal resistance values depending on the direction of the current paths as in vertical and horizontal resistance measurements. The significant difference of these two measurements arises from small deviations from a perfect square shape of the sample. In fact, to obtain the true resistivity of the material, one needs to take the average value of the two measurements.

The discrepancy of the bulk conductivity obtained from the inverted and lateral resistance measurements is similar to the discrepancy that occurs from the horizontal and vertical resistance measurements obtained from a van der Pauw measurement. Since the inverted resistance measurement is much more vulnerable to imperfections of the sample geometry, we recommend adjusting the C_1 value in such a way that inverted measurement matches the lateral measurement at around 3.3 K.

After adjusting and combining the three plots in Fig. (5.2) (b), we obtain the bulk conductivity that covers the entire temperature range shown in Fig. (5.2) (c). From this

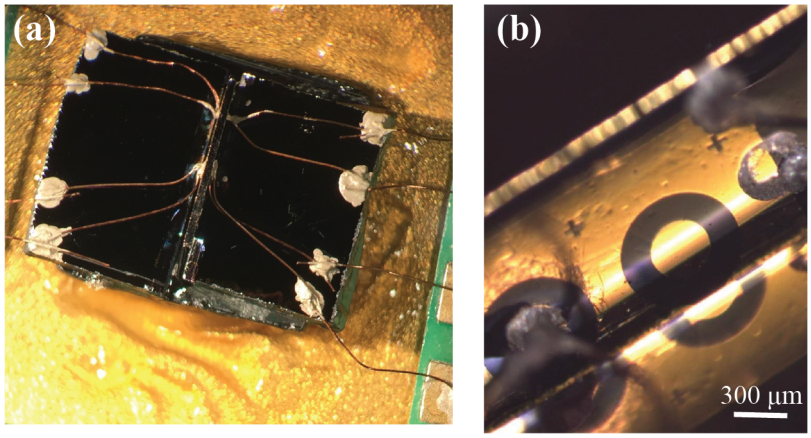

Figure 5.3: Double-sided two-terminal Corbino disk. (a) Top view. (b) Side view. In preparation for submission to a journal [86].

exercise, we have demonstrated that the bulk conductivity can be found even in the surface-dominated regime. Also, we have shown that the bulk conductivity of SmB_6 continues to exhibit a thermally excited behavior according to $\sigma_b \propto \exp(-E_a/k_BT)$, where we find the activation behavior of $E_a = 3.84$ meV.

5.3 Double-Sided Two-Terminal Corbino Disk on SmB_6

In the previous subsection, we measured the inverted resistance, R_{Inv}, successfully down to 2.5 K. According to Eq. (4.6), the magnitude of the R_{Inv} is inversely proportional to σ_s^2. For samples that have a higher surface conductivity, the magnitude of R_{Inv} will be smaller in general, and therefore the measurement may fail at higher temperatures. To overcome these limitations, we instead use a transport geometry that allows larger C_1 values.

5.3.1 Sample Preparation

In this subsection, we demonstrate the bulk conductivity extraction from the coaxially aligned two-terminal double Corbino disk geometry that is shown in Fig. (4.8). We use SmB_6 crystals from the same batch to make this double-sided sample. The top and bottom surfaces of the sample were first polished by using a SiC polishing pad of 15.3 μm. Then, the surfaces were polished by finer grit sizes of SiC pads: 5.5 μm and 2.5 μm. The polishing was finalized by using a polishing cloth (TexMet C) with 0.3 μm Al_2O_3 slurry. We performed photolithography on each of the polished surfaces with a mask design with identical dimensions to the two-terminal Corbino disks shown in Fig. (4.8) (a). We evaporate Ti/Au (20 Å

/1500 Å), and then lifted off the photoresist on the regions where we intend to expose the surface. We attached the sample with GE varnish on a silicon piece with native oxide so that both surfaces were exposed. We used copper wires (2 mils), and attached them with silver paste. The sample that is prepared is shown in Fig. (5.3).

5.3.2 Experimental Results

The sample was characterized using standard low frequency lock-in measurements from room temperature to cryogenic temperatures (300 K – 2.5 K). We measured the resistances of the four different configurations shown in Fig. (4.8) (b) – (e) (R_L, R_R, R_V, and R_H). The experimental results of resistance vs temperature for all four measurements are shown in Fig. (5.4) (a). At temperatures below 3.6 K, in the surface-dominated regime, resistance plateaus are observed in R_L, R_R, and R_V. By comparing the magnitudes, the relations $R_R = 1/2R_L$ (Eq. (4.7)) and $R_V \approx 2R_L$ (Eq. (4.9) holds, which verifies the existence of the conducting surface. From, R_R, we find the surface conductivity, $\sigma_s = 1.1 \times 10^{-3}$ S. This value is more than three times higher than the SmB_6 sample in the previous demonstration ($\sigma_s = 3.3 \times 10^{-4}$ S). In the hybrid measurement, R_H, drops toward 0 Ω as the temperature is lowered below 3.6 K.

To extract the bulk conductivity from Fig (5.4) (a), we converted the resistance measurements to bulk conductivity by the following, similar to the single-sided 4-terminal Corbino disk case in the previous section.

High temperature range (bulk-dominated regime): At high temperatures, above 5.2 K, the lateral resistance data is used to extract the bulk conductivity. Using C_{-1} found in Fig. (4.10) (b) and Eq. (5.1), the bulk conductivity is found, as shown in the solid blue line in Fig. (5.4) (b).

Intermediate temperature range (bulk-to-surface crossover regime): At intermediate temperatures, ranging from 3.5 K – 5.2 K, we again use the lateral resistance measurement and use Eq. (5.2) with $\gamma = C_0 t/C_{-1}$, which was derived from the two-channel model. The result is shown in the solid green line in Fig. (5.4) (b).

Low temperature range (surface-dominated regime): At low temperatures, below ∼3.5 K, the sample is in the surface-dominated regime. Here, we use the hybrid resistance measurement to find the bulk conductivity. Eq. (5.6) can be used to convert the hybrid resistance to bulk conductivity. σ_s can be found from the plateau value of R_L, and C_1 can be found from Fig. (4.10). We used both the C_1 values when the top and bottom Corbino disks are perfectly aligned and when the two disks are misaligned by 150 μm. The solid black line is the bulk conductivity when the two disks are perfectly aligned, the solid red line is the bulk

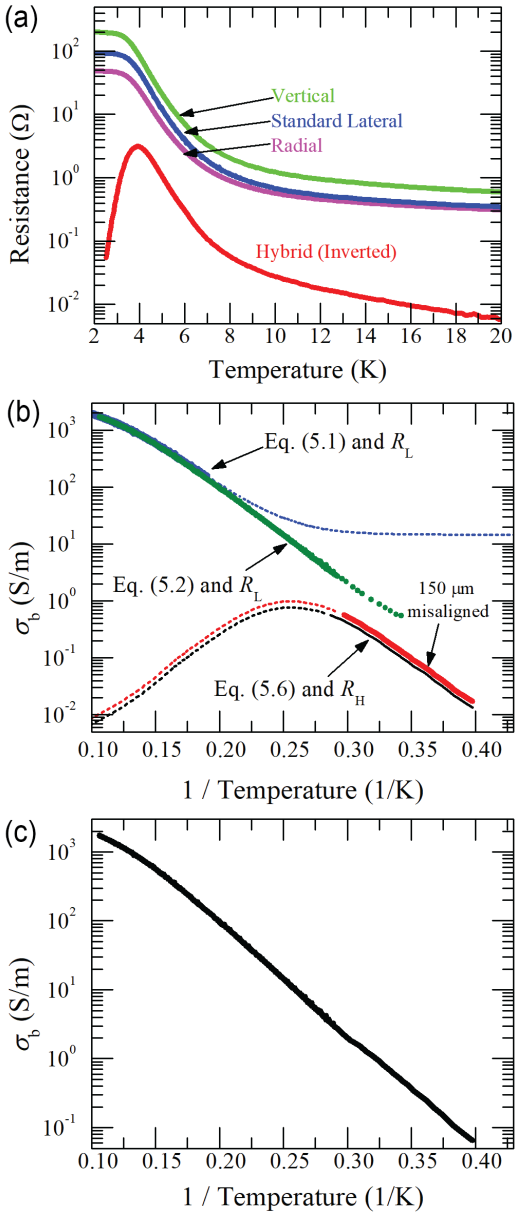

Figure 5.4: Experimental results and bulk conductivity analysis of the double-sided 2-terminal Corbino disk on a SmB_6 sample with thickness, $t = 210$ μm. (a) Resistance vs. temperature of the lateral, vertical, radial, and the hybrid measurement (inverted measurement). (b) The bulk conductivity converted from the measured resistance shown in (a). The dotted lines indicate the bulk conductivity conversion applied beyond the appropriate regime. (c) The result of the bulk conductivity after adjustment of mismatch. In preparation for submission to a journal [86].

conductivity when the two are misaligned by 150 μm.

Similar to the previous example, there is a mismatch between the bulk conductivity at low temperatures and the bulk conductivity at intermediate temperatures. The reason for this mismatch is identical to the reason for the mismatch present in the single-sided four-terminal demonstration in that the geometric coefficients may not correspond to the actual sample geometry. In addition to the reasons mentioned in the previous subsection, the misalignment of the top and bottom Corbino disks must also be considered. After the fabrication process, we find an unintentional misalignment of $\sim$150 μm; however, even if we consider this misalignment, the corrected bulk conductivity still does not account the matching of the bulk conductivity found from the lateral resistance measurement at intermediate temperatures.

Again, we adjust the bulk conductivity curve at low temperatures (solid red line) to match the conductivity at intermediate temperatures (solid green line). The result of bulk conductivity is shown in Fig. (5.4) (c). We note that in this particular sample the inverted resistance measurements allowed us to measure bulk conductivity down to 2.5 K when 99.9% of the current was flowing on the surface of the sample. We plan to present the bulk transport properties of SmB_6 and related materials and the implications of these measurements within the context of topological Kondo insulators in Chapter 6.

5.4 Discussion and Conclusion

We have introduced a new type of transport measurement, which we call the inverted resistance measurement. Together with a conventional transport measurement, it allows us to characterize materials that have both bulk and surface conduction, such as TIs. The inverted resistance measurement is powerful in the regime where the surface conduction dominates the bulk. The inverted resistance is proportional to σ_b/σ_s^2, and therefore the bulk conductivity, σ_b, is accessible even in the regime where surface conduction is dominant, making this measurement powerful. This inverted resistance measurement requires a loop as a current lead that encloses the other current lead, and two voltage leads placed outside of the current loop. We have analyzed different transport geometries that utilize this inverted measurement. The most ideal transport geometry for this inverted measurement is when two Corbino disks are coaxially aligned on two opposite surfaces. If the sample is thick, the inverted measurement can also be performed using a single-sided four-terminal Corbino disk geometry. We note that this type of measurement is not suitable for characterizing purely 2D systems or thin films as we expect the inverted resistance would be zero, regardless of the conductivities of the material.

The geometric prefactors (C_{-1} and C_1), which are used for converting from resistances to conductivities, were found using finite element analysis simulations. Experimentally, we have successfully realized the transport geometries on SmB_6 samples, and measured the resistances at different temperatures. SmB_6 turns out to be an ideal material for testing our transport method because the bulk has a thermally activated behavior and nearly temperature-independent surface conductivity. By performing the experiments from 2 – 20 K, we extracted the bulk conductivity, which includes both the bulk-dominated and surface-dominated regimes. We note that the numerically found geometric prefactors were used to extract the bulk conductivity, and a noticeable discontinuity between the results from the bulk-dominated regime and the surface-dominated regime existed, suggesting there is likely a discrepancy in the dimensions between the ideally suggested transport geometry and the realized samples. However, the activation energy, or the slope of the bulk conductivity vs. $1/T$, are consistent in the two regimes, suggesting that they can be patched together by adjusting the prefactors. We recommend adjusting the prefactor corresponding for the inverted resistance measurement. Using these methods, we have found the bulk conductivity of SmB_6, extending about two extra orders of magnitude compared to the conventional resistance measurement.

We expect our newly proposed method of transport can be used in a broad range of materials beyond SmB_6. For these new materials, we hope that the community does not rely on the conventional transport methods such as residual-resistance ratios that can be problematic in the presence of two-channels, and instead, employ our transport methods.

In the following chapter, we will employ this inverted resistance measurement to further study the bulk of SmB_6.

Chapter 6

Bulk Studies of SmB_6: Role of Disorder

6.1 Introduction

[1]In the previous chapter, we have demonstrated that the inverted resistance measurement indeed works well for finding the bulk conductivity below the bulk-to-surface crossover temperature. Now we are equipped to study the bulk of SmB_6 and related materials in a wider temperature range.

SmB_6 is known as a Kondo insulator, a material in which a small band gap forms by the hybridization between the $5d$-conduction electrons and the $4f$-localized electrons, and the Fermi energy is located in this gap. To be more precise, SmB_6 is a mixed valence system in that the samarium ions exist both in the $Sm^{2+}(4f^6)$ and the $Sm^{3+}(4f^5 5d)$ states with a 3:7 ratio [10].

The role of the valence states in the insulating bulk gap has been an important question to the researchers. In particular, to understand this role, researchers have studied transport on SmB_6 by systematically changing the doping level (including the level of Sm vacancies) [27, 87–91].

Recently, doped SmB_6 has also been studied for understanding the surface. One important study is transport on magnetically doped SmB_6 samples. This is important for verifying the topological Kondo insulator (TKI). TKI predicts that the topologically-protected surface states can only exist if the system preserves time-reversal symmetry. Since magnetic impurities can break the time reversal symmetry of the material system, experimental studies have tested if the surface states disappear in magnetically doped SmB_6 samples [90, 91].

[1]The author and his collaborators are preparing a manuscript for submitting to a peer-reviewed journal that will contain contents in this chapter.

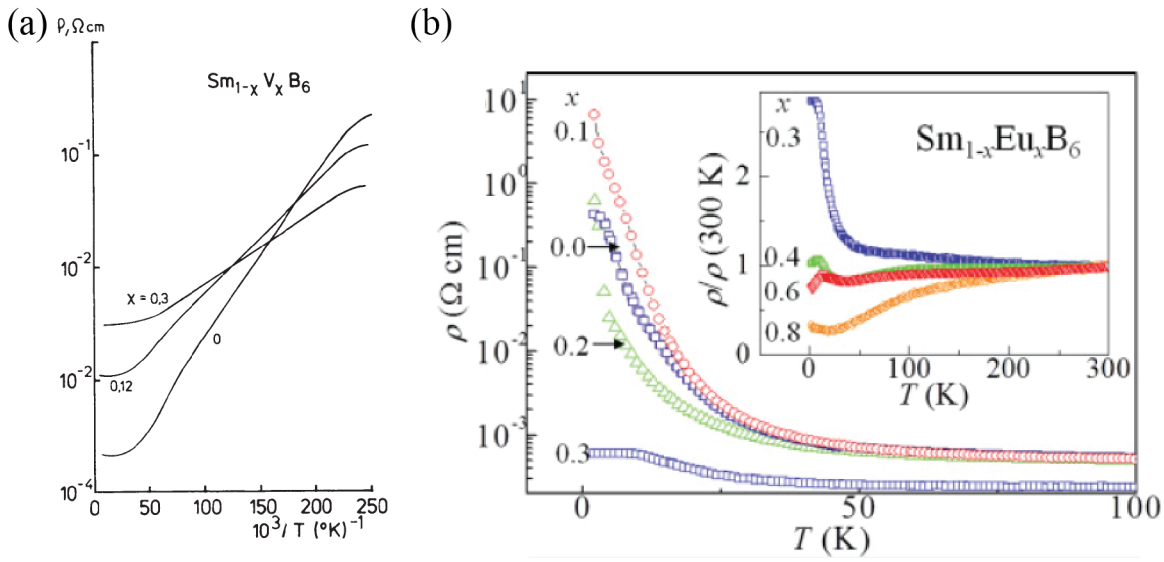

Figure 6.1: Previous transport reports on vacancy and Eu-doped SmB_6 Samples (a) Resistivity data by T. Kasuya *et al.* reported in 1977. With permission of Springer [27]. (b) Resistivity data reported by S. Yeo *et al.* in 2012. Reprinted figure with permission from [88], and also additional kind permission from the first author. Copyright (2012) by the American Physical Society.

To fully understand the role of substitution of atoms for such doped SmB_6 studies, one must also take into account the role of disorder. However, this aspect remains quite elusive. Some early Sm vacancy SmB_6 studies, such as the one from T. Kasuya *et al.* [27], do attempt to interpret their data in terms of disorder, but the researchers at the time were attempting to interpret the resistivity plateau that is now believed to originate from the surface. In fact, the Sm-vacant SmB_6 report by T. Kasuya *et al.* challenges the existence of the conducting surface state picture. Their data is shown in Fig. (6.1) (a). At high temperatures, the slope of the resistivity (or resistance ratio) changes at different Sm vacancy levels. In addition, the magnitude of the resistance plateau at low temperatures becomes lower when the Sm vacancy concentration increases. This is the opposite behavior of what we would expect with the conducting surface state in mind. We would expect the surface conductivity to be independent of the bulk resistivity rise. More importantly, when disorder increases, we would expect the mobility to be smaller, and therefore the surface resistance to increase. In other reports, this trend is different. For example, Yeo *et al.* [88], report ρ(bulk resistivity) vs. T on Eu-doped SmB_6 samples, shown in Fig. (6.1) (b). The data shows that the resistivity magnitude does not follow consistently with the doping level. Unfortunately, many of the other transport reports on doped SmB_6 report the resistance ratio ($R(T)/R(300\ \mathrm{K})$) that

make it impossible to compare this trend.

For the resistivity at the high temperatures, where the bulk is dominating, we would also expect significant consequences due to the change of disorder. For example, a large concentration of impurities that are positioned randomly can result in in-gap impurity states with hopping conduction that follows a resistivity behavior of, $\rho \propto \exp(T_0/T)^{(1/4)}$ [92]. To distinguish the thermally activated behavior from hopping conduction through random impurities, a large extension of resistivity magnitude for a wide temperature range must be measured. Also, if the role of disorder is significant, this can have consequences at low energy scales (at low temperatures). Because the surface state dominates at low temperatures, this was believed to be impossible to explore by transport in the past. But now, thanks to our newly invented inverted resistance measurement, this is now possible.

In this chapter, before we present our experimental work, a theory work done by our group will be introduced that does not involve the existence of the impurity states in the gap. This will be related to the experimental studies in this chapter. Within the in-gap impurity state picture, if the impurities are dilute, one may expect a hydrogen-like impurity state in the standard semiconductor picture. We point out that these hydrogenic impurities cannot be justified because the effective Bohr radius is too small. Next, we review a model that we recently proposed (A. Rakoski *et al.* [93]), as a possible alternative scenario for the bulk of SmB_6, where the gap is clean, and the bulk bands bend due to the existence of the surface states. This model can explain the difference between the transport and the spectroscopy gap. In addition, the model is able to explain a small hump feature in resistance and Hall resistance that exist around 10 K, which is observed very commonly by many researchers.

After the introduction of our clean gap model, we present our experimental work. First, we point out that even the bulk transport studies can be wrongly studied if the sample is not prepared carefully enough. Then, we use our inverted resistance measurement, which allows us to study the bulk of SmB_6 at temperatures below the bulk-to-surface crossover. We use the double-sided transport geometry that is similar to the ones that we used in the previous chapter. By additionally using an instrumentation amplifier during our transport measurement, we were able to measure the pure SmB_6 to even lower temperatures (down to around 1.9 K). To study the role of disorder, we also measure the inverted resistance on systematically disordered SmB_6 samples. These samples are intentionally grown with less samarium, expecting the disorder to be introduced. We find that the bulk resistivity changes by 10 orders of magnitude with a consistent thermal activation energy of $\sim$4 meV. This large magnitude verification provides evidence of the clean bulk gap. Inconsistent with the previous studies, we also find that the disordered samples show an almost identical thermal activation energy, with also a large resistivity magnitude change. Surprisingly, SmB_6

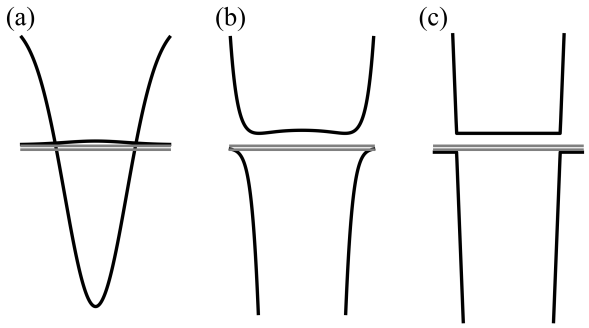

Figure 6.2: Dispersion of the bulk bands of SmB_6 along the Γ-X-Γ direction. (a) Band structure before hybridization. (b) Band structure after hybridization of the d band with one of the f bands. (c) Simplified band structure that is used in the model. Reprinted figure with permission from [93], and additional kind permission from the first author. Copyright (2017) by the American Physical Society.

samples grown with more than 25 % percent Sm deficiency show a mysterious plateau of bulk resistivity.

6.2 Clean Gap Model

In this section, a new bulk gap model based on the recent work of A. Rakoski *et al.* from our group will be introduced. Most importantly, this model does not involve the in-gap impurity states. Only a summary of this model and its consequences are explained in this section. A more detailed description can be found in the published work [93].

The original motivation for introducing this clean gap model for SmB_6 is to explain the difference between the transport gap and the spectroscopy gap, which was a big mystery to the SmB_6 community. Photoemission and tunneling spectroscopy measurements show a gap of 16 – 20 meV. On the other hand, many transport experiments report the activation energy from resistivity or Hall resistance as a function of temperature in the range of 3 – 4 meV. This difference is puzzling, because if the Fermi energy is at the middle, the transport gap should be measuring $\sim$10 meV instead. Various scenarios have been proposed to resolve this energy-difference issue. One popular scenario is the possibility of the existence of the impurity states in the gap [94]. Another possibility is the presence of an indirect band gap, resulting from the standard Kondo gap formation [81].

Before introducing the new clean gap model, the standard formalism that describes the localized impurity states, especially for semiconductors, will be reviewed. It turns out that

this formalism is problematic when it is applied to SmB_6. The standard way to understand the impurity states is by using the effective mass approximation. When an impurity is present in the material, we can normally treat this problem by adding an impurity potential to the single electron Hamiltonian. We then further simplify the Hamiltonian by assuming that the lattice potential felt by the electron can be treated as a background. This lattice potential information can be absorbed into the kinetic energy part of the electron by replacing the electron mass (m) with the effective mass (m^*). Specifically for an ionized impurity potential, we can treat it as a Coulomb potential in a dielectric material. Then, the problem is identical to a hydrogen atom Hamiltonian, except that the electron mass is replaced with m^*, and the Coulomb potential is modified for the material by replacing the vacuum permittivity with the dielectric constant (κ). However, in SmB_6, there is a danger in using this approach. Even after the f- and d- orbitals hybridize and form a gap, as shown in Fig. (6.2) (a) to Fig. (6.2) (b), the hybridized bands still have almost flat f-like characteristics near the Fermi energy. For the ionized impurity case, the effective mass approximation indeed fails, and it can be seen explicitly by calculating the effective Bohr radius,

$$a_B^* = \frac{4\pi\kappa\epsilon_0\hbar^2}{m^* e^2} = \frac{\kappa}{m^*/m}(0.53\ \text{Å}), \tag{6.1}$$

To treat the lattice potential as a background, a_B must be much larger than the lattice constant, which is $a = 4.13$ Å for SmB_6. The estimation of a_B results in a range of 0.5 – 4 Å, which is comparable to the lattice constant or even smaller. Therefore, our initial assumption that the impurity potential is slowly varying compared to the lattice potential is not valid, and the in-gap states cannot be treated as a hydrogenic-like problem in SmB_6.

While still relying on the standard gap physics, we find an alternative way to explain the discrepancy between the spectroscopy and the transport gap magnitude. Instead, we introduce a gap model that does not involve any in-gap impurity states. We assume the gap is clean, and this full gap magnitude is ∼20 meV. Without any impurity states in the gap, the Fermi energy will be positioned exactly at the middle of this gap. What is special about this model is that, because the material is presumed to be intrinsic, the bands can bend by the existence of the surface states[2] easily with an associated pinning energy (E_{pin}).

This band bending effect has been calculated numerically across a sample by solving the Poisson equation self consistently. The result is shown in Fig. (6.3) (a) at 8 K, when the $E_{\text{pin}} = 5.5$ meV. The bands bend near the boundaries (surface) remain almost unbent at the middle of the sample. Because the band bending of the conduction band and the valence band is identical, only the conduction band bending at different temperatures is shown in

[2]The origin does not necessarily have to be TI surface states to result in the band bending effect.

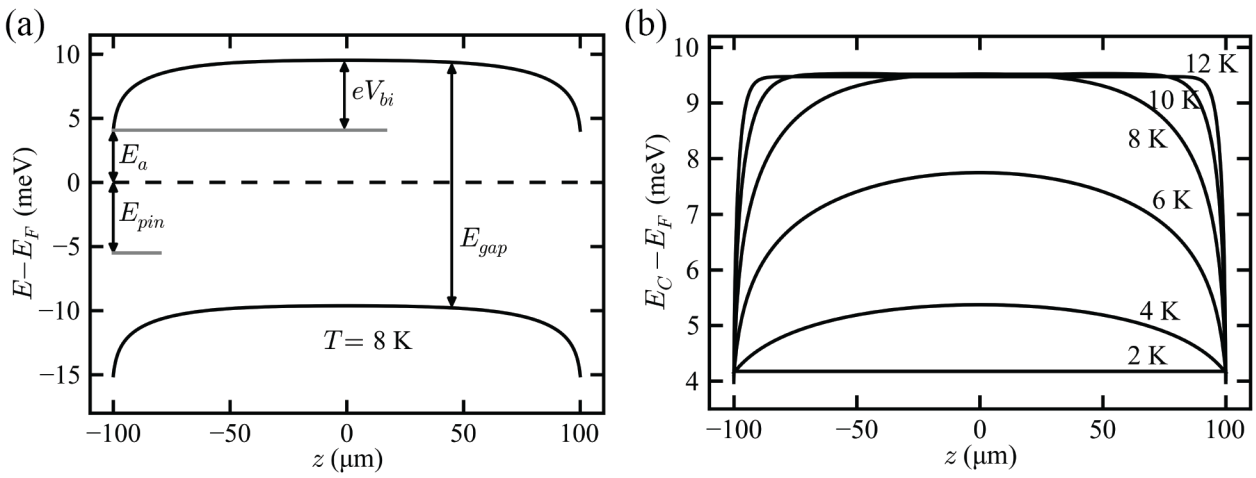

Figure 6.3: The numerical result of band bending in the clean gap of SmB_6. $E_{\text{pin}} = 5.5$meV and the sample thickness is 200 μm(a)Band structure result at $T = 8$ K. The relationship among the activation energy E_a, the built-in potential eV_{bi}, the pinning energy E_{pin}, and the gap E_{gap} are all shown. (b) Calculated bulk conduction band at different temperatures. Reprinted from [93] with kind permission from the first author. Copyright (2017) by the American Physical Society.

Fig. (6.3) (b). This result shows that at high temperatures (higher than 10 K), the conduction band is unbent at the middle of the gap, which is $E_{gap}/2$ from the Fermi energy. However, at lower temperatures, the conduction band bending effect is large enough to influence the middle of the geometry. Eventually, the conduction band becomes flat throughout the entire geometry, located about 4 meV above the Fermi energy instead of $E_{gap}/2$. This result can explain the difference between the transport gap and the spectroscopy gap. Transport at low temperatures will measure the gap between the Fermi energy and the bent conduction band, whereas the spectroscopy gap will remain with the full 20 meV gap.

This model involves two energy scales. At high temperatures, the pure bulk effect dominates the transport. At low temperatures, the bulk bands that are bent by the surface dominate the transport. This model results in a crossover between these two regimes at around 10 – 12 K. Simulating transport, using the simplified band model in Fig. (6.2) (c), this crossover manifests a hump feature that has seen by many researchers in the past. A comparison of the numerical results and the experimental reports are shown in Fig. (6.4). According to the model, this hump feature depends on the geometry of the sample, especially on the thickness. Further experimental studies on the effect of varying the thickness are currently under investigation.

In the following section, we discuss the importance of preparing the sample carefully

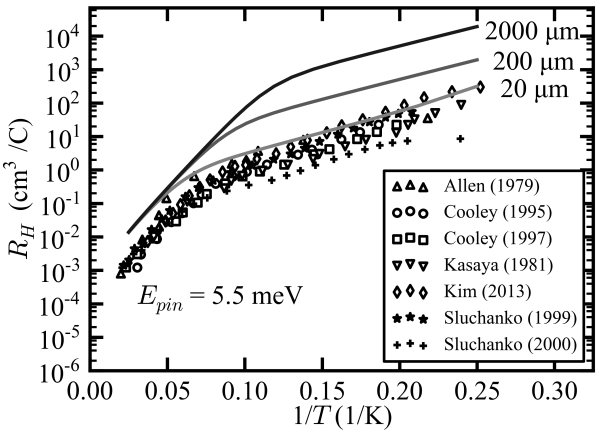

Figure 6.4: Simulation of Hall coefficients for samples of different thickness, and comparison with the reported Hall data [25,59,87,95–97]. Reprinted from [93] with kind permission from the first author. Copyright (2017) by the American Physical Society.

and choosing the correct transport geometry. We show that studying the bulk activation behavior between the range of the hump feature around ∼10 K, and a resistance plateau can be narrow when the sample is not carefully polished, and therefore a wrong activation energy will be estimated.

6.3 Sample Preparation and Transport Geometry Dependence

In Chapter 3, we have emphasized that choosing the proper transport geometry and carefully polishing the sample is very important for properly characterizing the surface of SmB_6. Here, we show that proper transport geometry and sample preparation is also important for characterizing the bulk.

Fig. (6.5) (a) shows the resistance as a function of inverse temperature measured by a Corbino disk (the one used here is part of a double-sided Corbino disk that is later used in the inverted resistance measurement) after carefully polishing the surface and a sample with standard 4-point contacts without any surface preparation. The two samples are from the same crystal growth batch, which is intentionally grown with 10 % less samarium. Consistent with what we learned from Chapter 3, depending on the transport geometry and surface preparation, the resistance plateau at low temperatures changes greatly. The Corbino disk geometry, shown in a solid blue line, reaches up to ∼100 Ω, whereas the 4-point geometry,

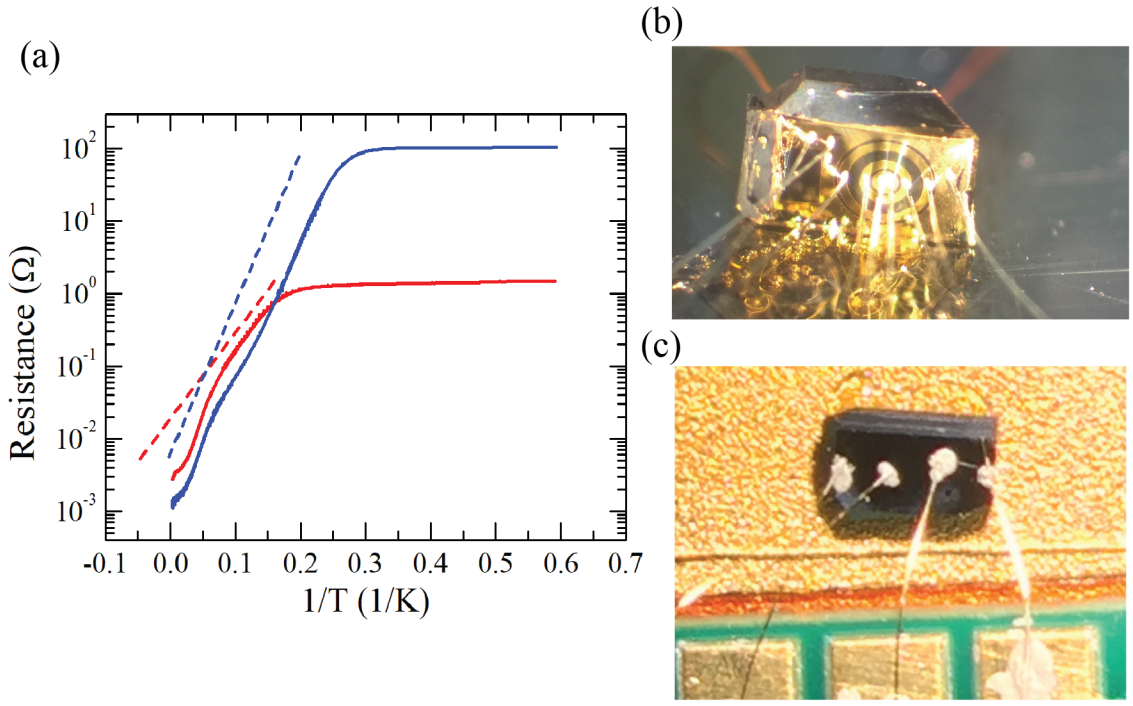

Figure 6.5: Comparison of transport results for different geometries on a sample grown with 10 % Sm deficiency. (a) Resistance vs. $1/T$ of SmB_6 samples grown with 10 % less samarium from two different transport geometries. The solid blue line is the data taken from the four-terminal Corbino disk, and the solid red line is the data taken from a 4-point contact on a raw sample (unpolished). (b) Picture of a four-terminal Corbino disk. The dotted lines are examples of how a researcher might incorrectly fit the slope to analyze the bulk resistivity. (c) Picture of a 4-point contact configuration on a raw sample. In preparation for submission to a journal.

shown in a solid red line, reaches up to a to ∼1 Ω.

Now let us compare the resistance features of the two data sets in the bulk-dominated regime. The high-temperature ranges from 0 – 0.5 K^{-1} seem to be parallel to each other, although the range is too small to be decisive. Below that temperature range, the two data sets show the hump feature near ∼0.1 (1/K), which is predicted in the model by A. Rakoski *et al.* [93], introduced in the previous section. However, the two sets of data have a slightly different magnitude and position. The resistance from the 4-point geometry (solid red line) shows the hump feature at 10 – 12 K extends in a more broader range. In fact, this feature is almost to the resistance plateau. Therefore, the 4-point geometry does not show a good range for analyzing the bulk activation energy. In Fig. (6.5) (a), we also show how one might fit the resistance data for extracting the bulk activation energy in dashed lines. The data from the four-point geometry shows that the extracted bulk activation energy would not be

correct.

Therefore, we must prepare the sample that results in a high resistance plateau magnitude such as the solid red line in Fig. (6.5) (a). However, even this Corbino disk geometry only provides the thermally bulk-activated region of about three orders of magnitude of resistivity. Also, we would like to know how the bulk behaves below the bulk-to-surface crossover temperature, where the resistance plateau dominates. Since we are now capable of extracting the bulk behavior even in the plateau region from our new inverted resistance measurement, we can investigate the bulk resistivity at lower temperatures.

6.4 Inverted Resistance Measurement of Samples Grown with Sm deficiencies

6.4.1 Sample Preparation and Transport Geometry

In this section, we briefly explain how we prepared our samples for bulk transport studies, and how they are measured.

The SmB_6 samples were grown by a flux method in an aluminum solution. In addition to the pure SmB_6 sample, other samples were grown with intentionally less samarium. Samples were grown with 10 %, 25 %, and 40 % less samarium when compared to the pure SmB_6 growth (or nominal $Sm_{0.9}B_6$, $Sm_{0.75}B_6$, and $Sm_{0.6}B_6$ samples). We do not necessarily expect the crystals to have the Sm vacancy level (point defect concentration) identical to these composition ratios, but we do expect the disorder to increase when the Sm is less in the crystal growth.

The samples were polished on both sides. The samples were first thinned with a SiC polishing pad that has a grit size of 15.3 μm. The final thicknesses of the samples result in the range of 200 – 400 μm. All of the samples were finally polished with an Al_2O_3 slurry with a 0.3 μm particle size on a polishing cloth (TexMetC). Any remaining aluminum flux inclusions were thinned away or etched with dilute HCl.

We performed standard photolithography to acquire the transport geometries that allow the inverted resistance measurement. The pure SmB_6 sample was measured on a single surface as shown in Fig. (6.6) (a). For the rest of the samples that were grown with less Sm, we prepared a double-sided geometry, for which all of the surface diagrams are shown in Fig. (6.6) (a), (c), and (e). Here we note that the transport geometry has a four-terminal Corbino disk on one side and a two-terminal Corbino disk on the other side. We performed standard photolithography by covering the pattern of the annular shaped region with photoresist, and expose the pattern where we want to evaporate the highly conductive metal.

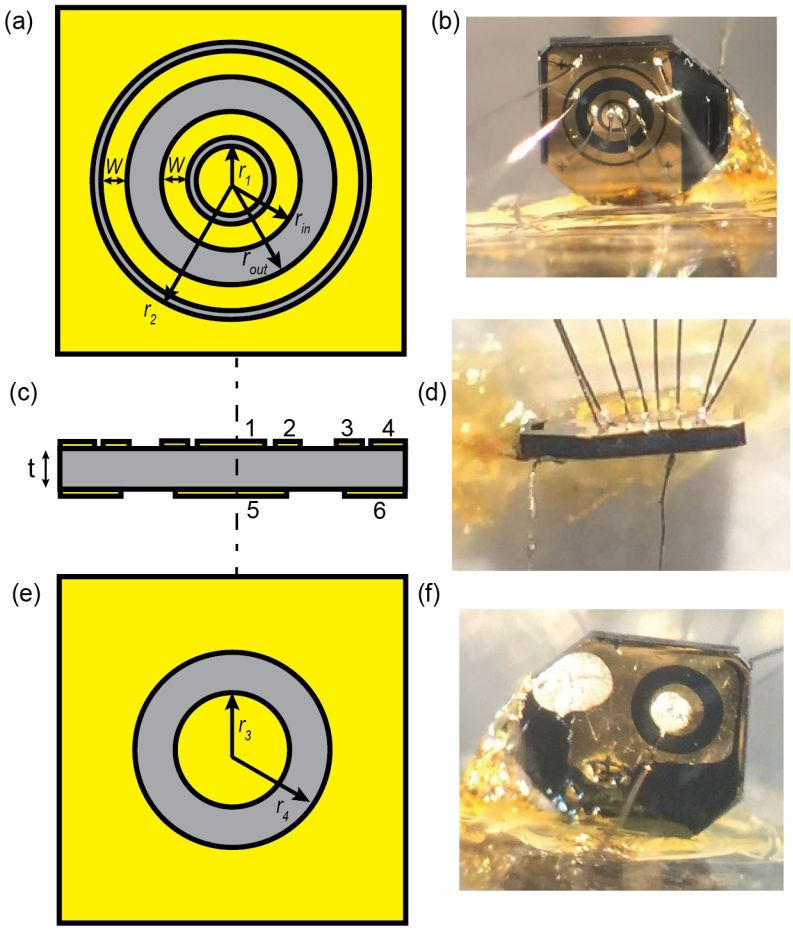

Figure 6.6: Transport geometry and device on a sample grown with a 40 % Sm deficiency (nominal $Sm_{0.6}B_6$). (a) The top view of the transport geometry. (b) Picture of the top view of the 40 % samarium-deficient grown sample. (c) Side view of the transport geometry. (d) Picture of the side view. (e) Bottom view of the transport geometry. (f) Picture of the bottom view of the nominal $Sm_{0.6}B_6$ sample. The dimensions are: $r_1 = 100$ μm, $r_2 = 800$ μm, $r_{\text{in}} = 200$ μm, $r_{\text{out}} = 300$ μm, $W = 75$ μm, $r_3 = 165$ μm, and $r_4 = 290$ μm. In preparation for submission to a journal.

We evaporated Ti/Au 20 Å/1500 Å, and lifted off the remaining photoresist with acetone. This entire process was done on each surface (top and bottom) at a time. We then attached aluminum wires (1 mil) using a wire bonder on one side. The sample was then mounted vertically on a sapphire glass with GE varnish, as shown in Fig (6.6) (d). Gold wires (1 mil) were connected on the other remaining surface by hand with silver paste. We also present pictures of one of our prepared samples in Fig. (6.6) (b), (d), and (f), next to the schematic diagrams for comparison.

We measured our sample from 300K – 1.7 K in the Quantum Design PPMS system. To measure the resistance of the samples, we use our own external electronics that are connected to the sample through the PPMS system. We performed low-frequency lock-in measurements using an external lock-in amplifier (SR830), together with a home-built instrumentation amplifier that has a common-mode rejection ratio performance of 120 dB.

We enumerated the terminals in the side view that is shown in Fig. (6.6) (c). The lateral resistance measurement is measured by sending current from terminal 1 to 4 ($I_{1,4}$), and measuring the voltage between terminal 2 and 3 ($V_{2,3}$), i.e., $R_{\mathrm{L}} = R_{1,4;2,3}$. The inverted resistance measurement is measured by two ways. The inverted resistance of pure SmB_6 is measured on a single surface by sending current from terminal 1 to 2 ($I_{1,4}$), and measuring the voltage between terminal 3 and 4 ($V_{3,4}$), i.e., $R_{\mathrm{Inv}} = R_{1,2;3,4}$. The inverted resistance on the other samples that are Sm-deficient grown are measured by sending current from terminal 5 to 6 ($I_{5,6}$), and measuring the voltage on the opposite surface between terminal 2 and 3 ($V_{2,3}$), i.e., $R_{\mathrm{Inv}} = R_{5,6;2,3}$.

6.4.2 Experimental Results

In this subsection, we discuss our transport results on the pure SmB_6 and the samples grown with less Sm. The resistance as a function of temperature are shown in Fig. (6.7) (a) – (d). In the lateral resistance measurement, shown in blue lines, the resistance plateau appears at low temperatures with magnitudes of 100 – 200 Ω. This corresponds to a sheet resistance of 2 – 3 kΩ. This is inconsistent with the previous reports shown in Fig. (6.1). We do not see a clear trend of the sheet resistance values. In the high-temperature region, above ∼4 K, the resistance increases when the temperature is lowered. This is consistent with the conventional resistance found from the series expansion of the two-channel resistance in the bulk-dominated regime ($\sigma_s \gg \sigma_b t$) when the bulk conductivity is thermally activated by $\sigma_b \propto \exp(-E_a/k_B T)$, where E_a is the activation energy:

$$R_C = \frac{C_{-1}}{\sigma_b t}, \tag{6.2}$$

where σ_b is the bulk conductivity, t is the thickness. Notice that each of the blue lines show a weak hump feature around ∼10 K, consistent with the previous transport reports and the prediction from the band bending discussed in the previous section [93].

In the inverted resistance measurements, shown in red lines, the magnitude first increases by lowering the temperature. The lines are almost parallel with the lateral resistance (blue lines), except for the hump features. Although a more thorough investigation is needed, this may be related to how we measure the resistance, where the corresponding effective thickness can be different between a lateral measurement and an inverted resistance measurement. Below ∼4 K, the bulk-to-surface crossover temperature, the resistance starts to drop, which is consistent with the inverted resistance found from the series expansion of the two-channel resistance in the surface-dominated region ($\sigma_s \gg \sigma_b t$) when the bulk conductivity is thermally activated:

$$R_{\mathrm{Inv}} = \frac{C_1}{\sigma_s^2}\sigma_b t, \tag{6.3}$$

where σ_s is the surface conductivity, and C_1 is the transport coefficient for the inverted resistance found by numerical simulations. In the pure SmB_6 sample, shown in the red line in Fig. (6.1) (a), the resistance approaches to zero as the temperature is lowered. At even lower temperatures, below 1.9 K, the resistance starts to fluctuate between a positive value and a negative value because the measurement has reached the limit of the amplifier performance (common-mode rejection ratio). Here, we only present data that is meaningful, which is higher than that performance limit.

In the SmB_6 samples grown with less Sm, the resistance shows a plateau feature instead of approaching zero. The nominal $Sm_{0.9}B_6$ sample is too noisy to notice whether there is a plateau, but the plateau appears to be more pronounced in the nominal $Sm_{0.6}B_6$ sample than the nominal $Sm_{0.75}B_6$ sample. In the following section, after converting the data shown in Fig. (6.7) to bulk resistivity, these small features will show a bulk resistivity plateau at low temperatures.

6.4.3 Analysis

In this subsection, we convert the resistance data to the bulk resistivity of the pure SmB_6 sample and the SmB_6 samples that are grown with less Sm.

We extract the bulk resistivity from the resistance data sets that are shown in Fig. (6.7). The method of extraction is identical to the demonstrations in Chapter 5. The transport coefficients for the used transport geometry, C_1 and C_{-1}, are shown in Fig. (6.8). The bulk resistivity above ∼4 K is found from the lateral resistance measurement, and the bulk resistivity below ∼4 K is found from the inverted resistance measurement. A two-channel

model (Eq. (4.6)) was used to find the bulk resistivity from the lateral resistance in the bulk-to-surface crossover regime. Similar to the demonstrations of bulk resistivity extraction in Chapter 5, the bulk resistivities in the bulk-dominated regime and the surface-dominated regime were mismatched in magnitude by a few factors. We adjust the bulk resistivity from the surface-dominated regime since the corresponding transport coefficient (C_1) is more vulnerable than the one for the bulk-dominated regime (C_{-1}).

The plots of bulk resistivity as a function of temperature are shown in Fig. (6.9) (a), and the same resistivity data as a function of inverse temperature are shown in Fig. (6.9) (b). For the pure SmB_6 bulk resistivity, shown in black, the thermally activated behavior in the surface-dominated regime and the bulk-dominated regime are identical. The activation energy is $E_a = 4.01$ meV, which is consistent with the earlier reports [40, 62, 82]. The magnitude of the bulk resistivity changes by ∼10 orders of magnitude. For the samples grown with less Sm, the bulk resistivities above ∼2K show a thermally activated behavior, and the activation energies are almost identical to the pure SmB_6 sample. The bulk resistivity of samples that are grown with a deficiency of Sm shows almost identical thermally activated behavior as the pure SmB_6 sample. Below ∼2 K, a strange resistivity plateau develops. The plateau is most pronounced in the nominal $Sm_{0.6}B_6$ sample, which was grown with the least Sm.

6.5 Discussion

For the pure SmB_6 sample, the large resistivity change is surprising when comparing to well-known narrow-gapped insulators (semiconductors). Typically, the temperature dependence of the resistivity of a semiconductor exhibits an intrinsic behavior at high temperatures, and then an extrinsic behavior at low temperatures. The extrinsic regime is dominated by the impurity states in the gap, and the resistivity is nearly flat over a certain temperature range. In order to extend the intrinsic regime over wider temperatures, the impurity concentration must be lowered. Certain applications in semiconductors require a very low impurity concentration. Integrated circuit applications, for example, require a silicon purity of 99.99999999 %, which corresponds to an impurity concentration of 5×10^{14} cm^{-3}. When the semiconductor is heavily doped, variable range hopping dominate the transport with a temperature dependence of $\rho = \rho_0 \exp(T_0/T)^{1/4}$. For even higher levels of doping (degenerate semiconductors), the impurities form extended states, and the material transitions from an insulator to a metal. In fact, in most 3D TIs, the bulk conductivity overwhelms the surface conductivity because the impurity concentration levels are in the heavily-doped regime. For example, in Bi_2Se_3 and Bi_2Te_3, the required impurity density level is ∼10^{14} cm^{-3} to avoid

hopping conduction and metal transition [98]. However, because of technical difficulties, the highest quality samples still have impurity levels that are a few orders of magnitude higher than this critical level [98].

Surprisingly, the bulk resistivity of SmB_6 (pure) neither exhibits the extrinsic regime of a low-doped semiconductor nor the variable range hopping behavior. Instead, the bulk resistivity exhibits a thermally activated behavior consistent with a clean gap over the entire temperature range that was measured. For the samples grown with less samarium, we expect to observe signatures of very large disorder. These samples also exhibit a large resistivity change with almost identical activation energies before the resistivity plateau appears. This indicates that disorder, which we expect to be induced by missing samarium sites in the lattice, does not play a role in the temperature dependence of the bulk resistivity. Instead, it is possible to expect point defects to disturb the density of states that are far away from the gap. A similar example is the BCS gap of a superconductor. Usually the superconducting state is immune to certain amount of alloying (i.e., large disorder) because the density of state is only perturbed far away from the BCS gap [99, 100].

The bulk resistivity plateaus observed in the SmB_6 samples grown with less Sm are also a surprise. They imply that at low temperatures, in the surface-dominated regime, a very small bulk channel is present while the surface conduction dominates. We note that the associated number of carriers are too small to explain the exotic bulk quantum oscillations seen by Tan *et al* [61]. Our current speculation is that these plateaus develop due to higher order defects than point defects, such as dislocations that might not be uniformly distributed, but may exist sporadically with length scales that extend throughout the bulk of the sample. If SmB_6 is a 3D topological insulator, one possibility is that these higher order defects may accompany topologically protected conduction paths. For future studies, this mysterious bulk conduction channel must be studied in more depth, including studies with other variously doped SmB_6 samples. Also, these possible defects must be visualized by probing methods such as tunneling electron microscopy (TEM).

6.6 Conclusion

In this chapter, the bulk transport of pure and Sm-deficient-grown SmB_6 was studied through the new inverted resistance measurement. A bulk model that does not involve in-gap impurity states was first introduced. We then showed experimentally, using the double-sided transport geometry, that the pure SmB_6 sample shows a robust thermally activated behavior. We also studied bulk transport on samples that are intentionally disordered by growing with substantially less samarium. Surprisingly, these samples show identical thermally activated

behavior compared to the pure SmB_6 until an unexpected resistivity plateau develops. Our results suggest that the bulk of SmB_6 is immune to disorder originating from point-like defects, but may be influenced by higher order defects.

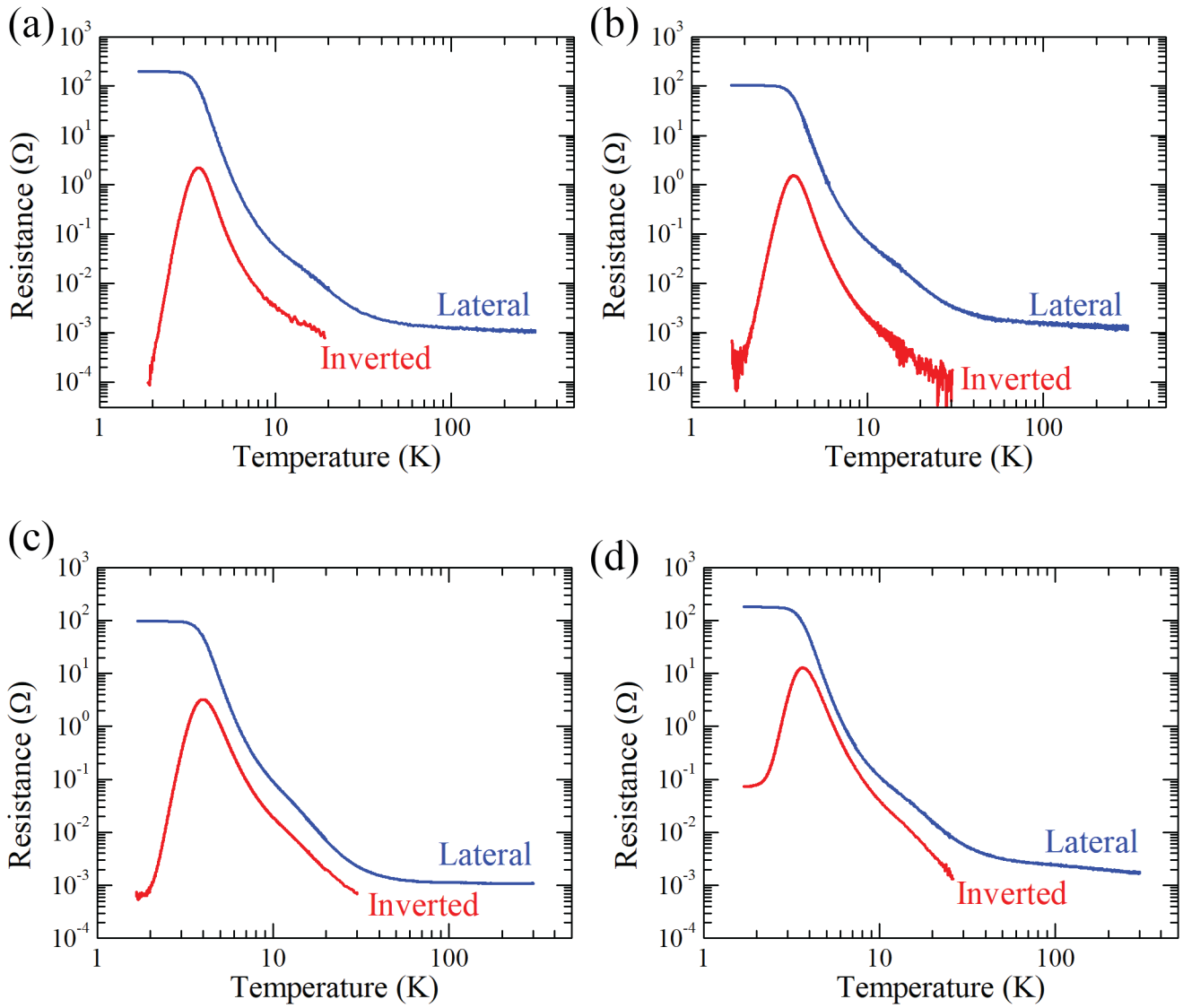

Figure 6.7: Resistance vs. temperature of pure and Sm–deficient grown SmB_6 samples. The blue lines are results from the lateral resistance, and the red lines are results from the inverted resistance. (a) Pure SmB_6. (b) SmB_6 grown with 10 % less Sm.(c) SmB_6 grown with 25 % less Sm. (d) SmB_6 grown with 40 % less Sm. In preparation for submission to a journal.

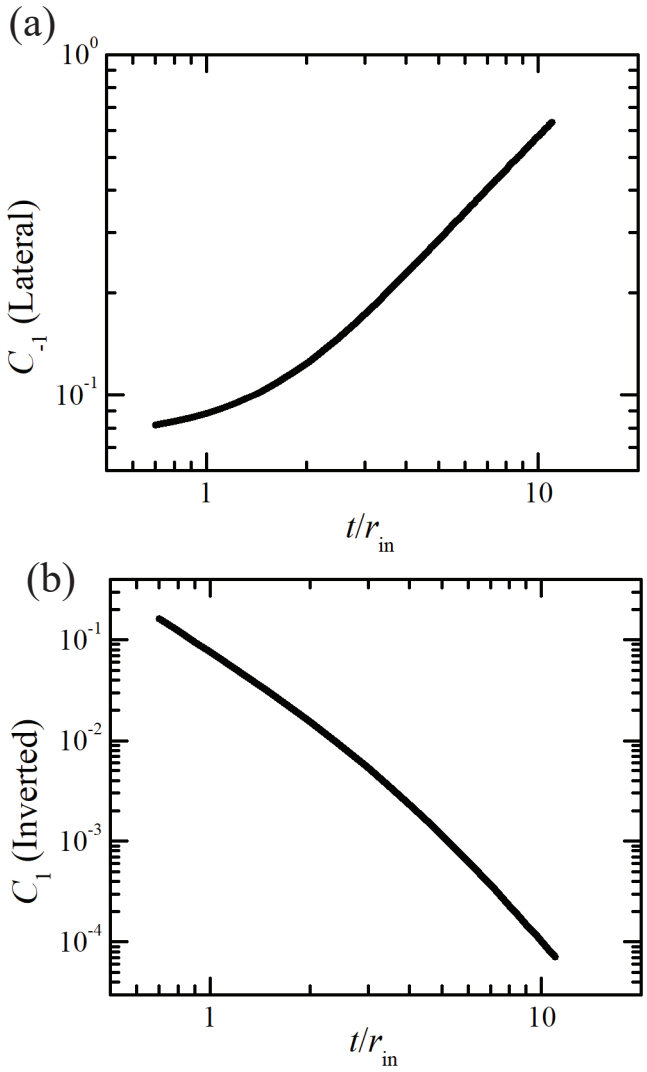

Figure 6.8: The transport coefficients that were used to extract the bulk resistivity of the vacancy SmB_6 samples. (a) Transport coefficient for the lateral resistance at high temperatures. (b) Transport coefficient for the inverted resistance at low temperatures. In preparation for submission to a journal.

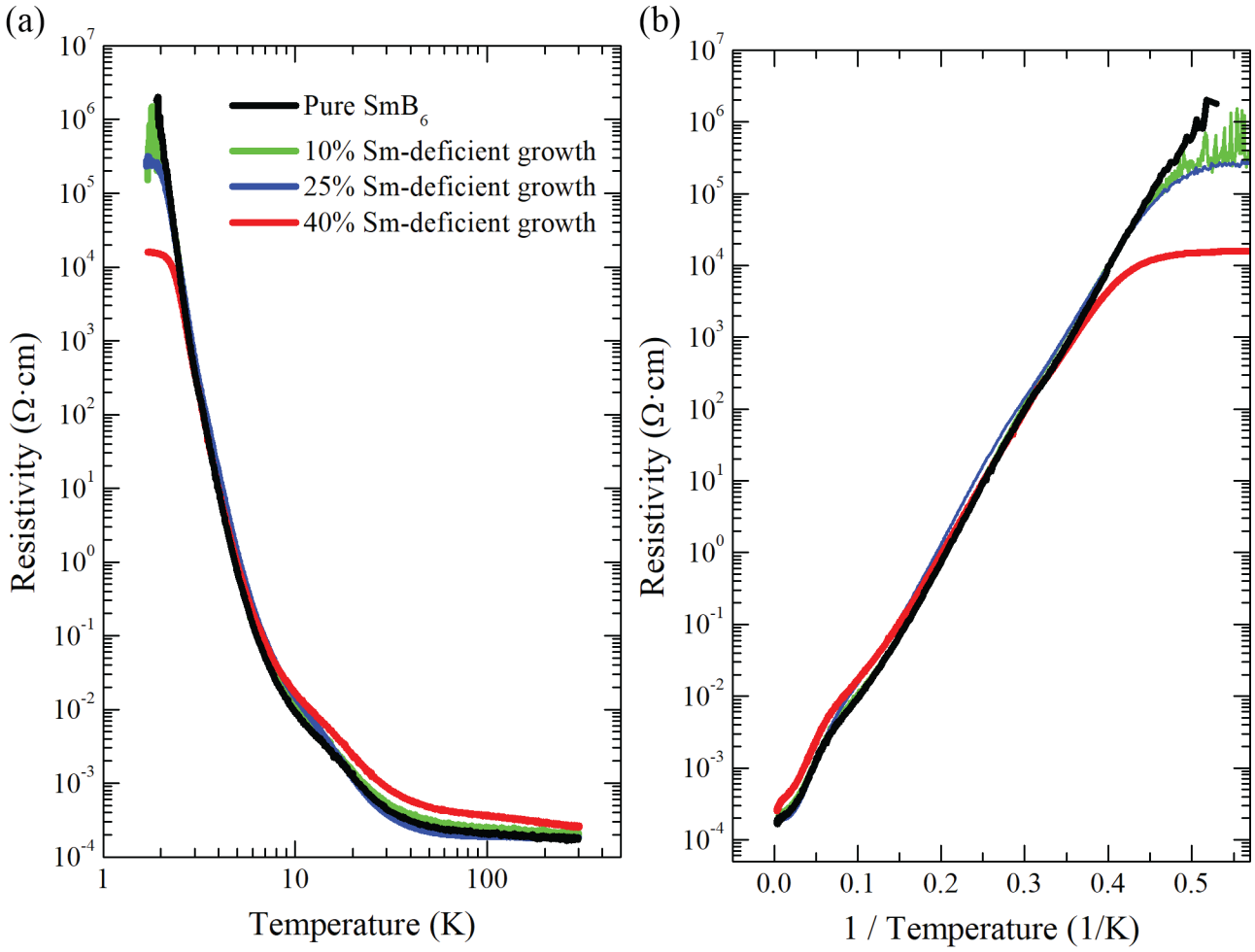

Figure 6.9: Temperature dependence of bulk resistivity of pure SmB_6 and samples grown with less Sm. (a) Bulk Resistivity vs. temperature of SmB_6 and samples grown with less Sm. (b) Bulk Resistivity vs. 1/Temperature of SmB_6 and samples grown with less Sm. In preparation for submission to a journal.

Chapter 7

Conclusions and Outlook

7.1 Summary

Motivated by the theoretical predictions that SmB_6 is a topological Kondo insulator, and the experimental discovery of the conducting surface states [40], the surface and bulk of SmB_6 were investigated by using electrical transport in this dissertation.

We studied the surface of SmB_6 using magnetotransport. We were not able to observe SdH oscillations even at high magnetic fields up to 93 T, and therefore we were not able to separate the contribution of each Fermi pocket. We, therefore, relied on classical magnetotransport and extracted the (effective) carrier density and mobility. During the studies, we found that the transport geometry and surface preparation can significantly impact the surface transport experiments. By choosing a Corbino disk geometry instead of using standard Hall bar geometry, our estimated carrier density has changed from an unphysically large value to an acceptable value. Also, we have noticed that subsurface cracks and boundaries of a polycrystal can conduct as well as the crystalline surface, and therefore can lead to an overestimation of the carrier density. With the careful considerations of these issues, our estimated carrier density and mobility on the SmB_6 (001) crystal surface is 2.71×10^{13} cm^{-2} and 104.5 cm^2/(V·sec), respectively. Using these values, we constructed a parameter space of where each carrier density and mobility of the Fermi pockets (Γ and $2X$) can be located. Among many experimental reports that can be compared with surface transport, only the X-pocket ARPES reports are consistent with our transport parameter space.

To study the bulk of SmB_6, including at low temperatures where the surface conduction dominates, we invented a new transport method, which we call the inverted resistance measurement. The bulk resistivity can be found at low temperatures by measuring the voltage outside of the Corbino disk loop, while the current flows conventionally through the loop. To optimize the performance of this method, we have developed several transport geome-

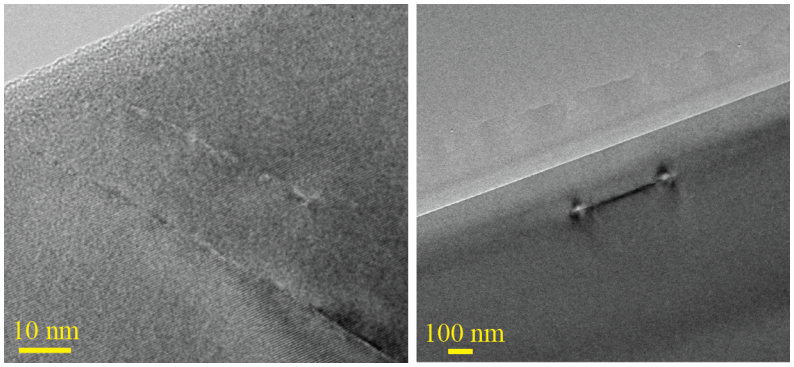

Figure 7.1: TEM image of the 40% Sm-deficient grown SmB_6 sample. The line features can either be local line defects or subsurface cracks created by the final polishing step. Figure courtesy of A. Rakoski.

tries, including Corbino disks that are coaxially aligned on two opposite surfaces. We have demonstrated that this transport geometry works well experimentally, and also showed that this double-sided Corbino disk transport geometry could be used as an alternative to the non-local transport geometry that Wolgast *et al.* [40] used for discovering the surface states of SmB_6. We expect our new transport geometries to be used in materials that are predicted to have surface states similar to SmB_6.

We have studied the bulk of both pure SmB_6 and SmB_6 samples that were grown intentionally with less Sm using our inverted resistance measurement. We find that the bulk resistivity of SmB_6 is an ideal insulator that continues to be thermally activated with an activation energy of 4.01 meV. The bulk resistivity result that includes both the bulk- and surface-dominated regimes extends to about ten orders of magnitude, which is exceptionally large even comparing it with other high-quality intrinsic semiconductors. For the bulk resistivity results on samples grown with Sm-deficiency, we also find a thermally activated behavior that is not significantly different from the pure SmB_6 results. From this, we believe that the gap of SmB_6 is robust against disorder and impurities. In addition, at low temperatures, we find that the highly Sm-deficient samples show a bulk resistivity plateau, which has not been seen by anyone because the surface conduction dominates in conventional transport geometries. To the best of our knowledge, this bulk resistivity plateau cannot be explained by our conventional understanding of conduction through regular carriers or hopping through impurities.

7.2 Future Work

Our study of the bulk of SmB_6 suggests that the role of disorder and impurities may be very different from what we understand in conventional materials. To understand this aspect further, we expect that future inverted resistance measurements on doped SmB_6 with both nonmagnetic and magnetic atoms may provide further excitement and insights. We speculate that conduction through higher order defects that may extend throughout the entire sample may be the cause of the low-temperature bulk-resistivity plateau that we observe in the 25 % and 40 % Sm-deficient samples.

Using a transmission electron microscope (TEM), our group is currently investigating if 1D defects or higher dimensional defects that extend throughout the bulk exist in the samples we measured. So far, we tried to probe through thin specimens that were cut from the active transport region of the 40 % Sm-deficient SmB_6 sample that was used for the double-sided Corbino disk transport measurement in the previous chapter, as shown in Fig. (7.1). Interestingly, we have found small imperfections near the surface. However, these features only exist near the surface of the active region of the Corbino disk. Also, the position and the length scales of these features are in the order of 0.1 μm, which is the same order of magnitude of the Al_2O_3 particles (0.3 μm) that were used in our final polishing procedure. This suggests that these features are subsurface cracks rather than line dislocations. Further investigation is needed if conduction through 1D (or higher dimensional) defects are the very cause of the bulk resistivity plateaus.

Appendix A

More Details on the Parameter Space Construction

In this appendix, we discuss more details about constructing the parameter space of Fig. (3.9).

A.1 Considering Mobilities

For the reader, it may not be clear why one of the channel (Γ) requires a higher mobility than the effective mobility (the mobility we find from the surface Corbino magnetotransport experiment), while the other channel ($2X$) requires a lower mobility than the effective mobility.

In the presence of two mobilities from each channels Γ and $2X$, say μ_Γ and μ_{2X}, suppose they are both higher value than the effective mobility, μ_{eff}, i.e., $\mu_\Gamma > \mu_{\text{eff}}$ and $\mu_{2X} > \mu_{\text{eff}}$.

We can express Eq. (3.6) as:

$$\mu_{\text{eff}}^2 = (\mu_\Gamma^2 - \mu_{2X}^2)(\frac{\sigma_\Gamma}{\sigma_t}) + \mu_{2X}^2 = \frac{\sigma_\Gamma \mu_\Gamma^2 + \sigma_{2X}\mu_{2X}^2}{\sigma_t}, \tag{A.1}$$

We first consider the condition of $\mu_\Gamma > \mu_{\text{eff}}$. This requires:

$$\mu_\Gamma^2 > \frac{\sigma_\Gamma \mu_\Gamma^2 + \sigma_{2X}\mu_{2X}^2}{\sigma_t}. \tag{A.2}$$

Eq. (A.2) can be rearranged as

$$(\sigma_t - \sigma_\Gamma)\ \mu_\Gamma^2 > \sigma_{2X}\ \mu_{2X}^2. \tag{A.3}$$

Since $\sigma_t = \sigma_\Gamma + \sigma_{2X}$, we can write Eq. (A.3) as:

$$\sigma_{2X}\ \mu_\Gamma^2 > \sigma_{2X}\ \mu_{2X}^2. \tag{A.4}$$

Since the conductivity is always positive, we can cancel the conductivity without changing the inequality sign. This reduces to:

$$\mu_\Gamma^2 > \mu_{2X}^2. \tag{A.5}$$

Also, the mobility is always positive, so the square root will not change the inequality:

$$\mu_\Gamma > \mu_{2X}. \tag{A.6}$$

Next we consider $\mu_{2X} > \mu_{\text{eff}}$. We can again use Eq. (A.1):

$$\mu_{2X}^2 > \frac{\sigma_\Gamma \mu_\Gamma^2 + \sigma_{2X}\mu_{2X}^2}{\sigma_t}. \tag{A.7}$$

Then similar to the steps Eq. (A.2) - Eq. (A.6), Eq. (A.7) can be expressed as:

$$\mu_{2X} > \mu_\Gamma. \tag{A.8}$$

Eq. (A.8) is in contradiction to Eq. (A.6), so $\mu_\Gamma > \mu_{\text{eff}}$ and $\mu_{2X} > \mu_{\text{eff}}$ cannot be satisfied at the same time.

Next, we consider when at least one of the mobilities is the same as the effective mobility, $\mu_\Gamma = \mu_{\text{eff}}$ or (and) $\mu_{2X} = \mu_{\text{eff}}$. We consider $\mu_\Gamma = \mu_{\text{eff}}$ case first. From, Eq. (A.1), this condition requires:

$$\mu_\Gamma^2 = \frac{\sigma_\Gamma \mu_\Gamma^2 + \sigma_{2X}\mu_{2X}^2}{\sigma_t}. \tag{A.9}$$

Then, from the similar calculations above, Eq. (A.2) result in:

$$\mu_\Gamma = \mu_{2X}. \tag{A.10}$$

Similarly, from condition $\mu_{2X} = \mu_{\text{eff}}$, we get the identical result. Because Eq. (3.3), $\sigma_t = \sigma_\Gamma + \sigma_{2X}$, must also satisfy, $n_\Gamma = n_{2X}$. This result is meaningless in that we have just split one pocket into two pockets with identical properties.

Therefore, in the presence of two channels, one of the mobilities has to be larger than the effective mobility ($\mu_\Gamma > \mu_{\text{eff}}$), and the other has to be smaller ($\mu_{2X} < \mu_{\text{eff}}$):

$$\mu_{2X} < \mu_{\text{eff}} < \mu_{\Gamma}. \tag{A.11}$$

A.2 Considering Carrier Densities

Next, we consider the carrier densities of each pocket in the parameter space. For the reader, it may also not be clear why one of the channel (Γ) requires a higher carrier density than the effective carrier density (the carrier density we find from the Corbino magneto-transport), while the other channel ($2X$) has to occupy the lower right part of the paramter space region.

Notice because the total conductivity is the sum of the conductivities of each channel, the conductivity of each channel must be smaller than the total conductivity, $\sigma_t > \sigma_{\Gamma}$ and $\sigma_t > \sigma_{2X}$.

We first consider the condition of $\sigma_t > \sigma_{\Gamma}$. This requires:

$$n_{\text{eff}}\mu_{\text{eff}} > n_{\Gamma}\mu_{\Gamma}. \tag{A.12}$$

Then, we can express this as:

$$\frac{\mu_{\text{eff}}}{\mu_{\Gamma}} > \frac{n_{\Gamma}}{n_{\text{eff}}}. \tag{A.13}$$

Since $\mu_{\text{eff}}/\mu_{\Gamma}$ must be smaller than 1 from what we found from the previous section, $n_{\Gamma}/\mu_{\text{eff}}$ must also be smaller than 1. Then we find:

$$n_{\text{eff}} > n_{\Gamma}. \tag{A.14}$$

Next, for the carrier density for the $2X$ channel, since $\sigma_{2X} > (e^2/h)$, and $\mu_{\text{eff}} > \mu_{2X}$, we have the following inequality:

$$n_{2X} > \frac{e}{h}\frac{1}{\mu_{2X}} > \frac{e}{h}\frac{1}{\mu_{\text{eff}}}. \tag{A.15}$$

Therefore, $n_{2X} > 2.3 \times 10^{12}$ cm^{-2}. Together with $\mu_{\text{eff}} > \mu_{2X}$, this corresponds to the lower right region of Fig. (3.9).

Appendix B

Instrumentation Amplifier

In this appendix, we introduce an instrumentation amplifier that was used for measuring small resistance values in the inverted resistance measurements. The circuit is shown in Fig. (B.1). Normally, when subtracting two voltage signals, we use a differential amplifier, which is equivalent to part II in the figure. When R_1 is equal to R_2, and R_3 is equal to R_4, the output voltage, V_{out}, is the differential signal, $V_A - V_B$, multiplied by the gain:

$$G_{II} = -\frac{R_3}{R_1}. \tag{B.1}$$

However, in reality, even if R_1 (R_3) and R_2 (R_4) are slightly different, there can be a significant common mode signal, $V_A + V_B$, with a common mode gain, G_C. This signal can be significant when measuring small signals. If we pre-amplify before the differential amplifier using the circuit as shown in part I in Fig. (B.1), we can overwhelm the common-mode signal. From part I, the differential signal can be amplified by a gain of:

$$G_I = \frac{R_A + R_B + R_C}{R_C}. \tag{B.2}$$

The total gain of the circuit shown in Fig. (B.1) when $R_1 = R_2$, $R_3 = R_4$, and $R_A = R_B$ is:

$$G_{Total} = -(\frac{2R_A}{R_C} + 1)\frac{R_3}{R_1}. \tag{B.3}$$

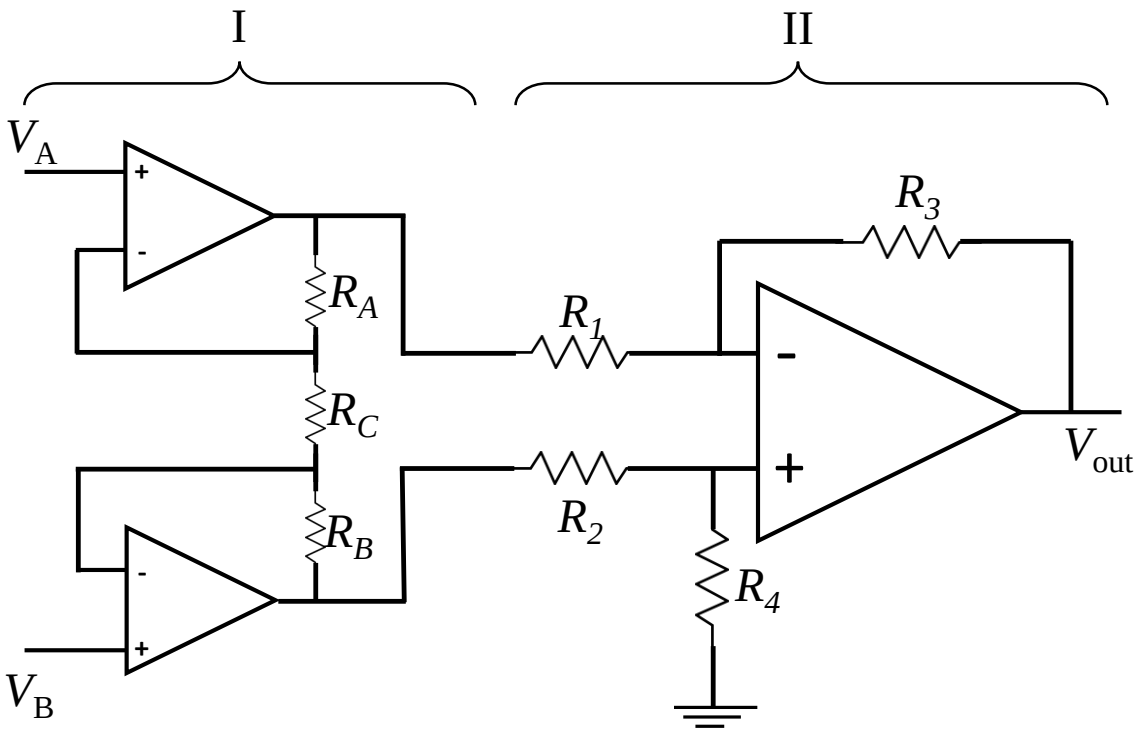

Figure B.1: Instrumentation Amplifier.

Bibliography

[1] N. W. Ashcroft and N. D. Mermin, *Solid State Physics*. (Brooks Cole, 1976).

[2] G. Allard, "X-ray study of some borides," *Bull. Soc. Chim. Fr.*, vol. 51, pp. 1213–1215, 1932.

[3] H. Longuet-Higgins and M. d. V. Roberts, "The electronic structure of the borides MB_6," in *Proceedings of the Royal Society of London A: Mathematical, Physical and Engineering Sciences*, vol. 224, pp. 336–347, The Royal Society, 1954.

[4] R. W. Johnson and A. Daane, "Electron requirements of bonds in metal borides," *The Journal of Chemical Physics*, vol. 38, no. 2, pp. 425–432, 1963.

[5] S. Massidda, A. Continenza, T. De Pascale, and R. Monnier, "Electronic structure of divalent hexaborides," *Zeitschrift für Physik B Condensed Matter*, vol. 102, no. 1, pp. 83–89, 1996.

[6] J. W. Allen, "Pre-TI history of SmB_6." http://smb6-conference.physics.lsa.umich.edu/tutorial, 2015. Accessed 8/04/17.

[7] A. Menth, E. Buehler, and T. H. Geballe, "Magnetic and semiconducting properties of SmB_6," *Phys. Rev. Lett.*, vol. 22, pp. 295–297, Feb 1969.

[8] T. H. Geballe, A. Menth, E. Buehler, and G. W. Hull, "Properties of SmB_6 doped with Eu and Gd," *Journal of Applied Physics*, vol. 41, no. 3, pp. 904–905, 1970.

[9] Y. B. Paderno, V. I. Novikov, and E. S. Garf, "Electrical properties of hexaborides of the alkaline- and rare-earth metals at low temperatures," *Soviet Powder Metallurgy and Metal Ceramics*, vol. 8, pp. 921–923, Nov 1969.

[10] R. L. Cohen, M. Eibschütz, and K. W. West, "Electronic and magnetic structure of SmB_6," *Phys. Rev. Lett.*, vol. 24, pp. 383–386, Feb 1970.

[11] A. Jayaraman, V. Narayanamurti, E. Bucher, and R. Maines, "Continuous and discontinuous semiconductor-metal transition in samarium monochalcogenides under pressure," *Physical Review Letters*, vol. 25, no. 20, p. 1430, 1970.

[12] M. Maple and D. Wohlleben, "Nonmagnetic $4f$ shell in the high-pressure phase of SmS," *Physical review letters*, vol. 27, no. 8, p. 511, 1971.

[13] C. M. Varma, "Mixed-valence compounds," *Rev. Mod. Phys.*, vol. 48, pp. 219–238, Apr 1976.

[14] J. Allen, R. M. Martin, B. Batlogg, and P. Wachter, "Mixed valent SmB_6 and gold−SmS: Metals or insulators?," *Journal of Applied Physics*, vol. 49, no. 3, pp. 2078–2083, 1978.

[15] J. C. Nickerson, R. M. White, K. N. Lee, R. Bachmann, T. H. Geballe, and G. W. Hull, "Physical properties of SmB_6," *Phys. Rev. B*, vol. 3, pp. 2030–2042, Mar 1971.

[16] L. L. Hirst, *Configuration-Based Ionic Energy Levels and Narrow Energy Bands*, pp. 3–16. Boston, MA: Springer US, 1977.

[17] N. Mott, "Rare-earth compounds with mixed valencies," *Philosophical Magazine*, vol. 30, no. 2, pp. 403–416, 1974.

[18] S. Doniach, "The Kondo lattice and weak antiferromagnetism," *Physica B+C*, vol. 91, pp. 231–234, 1977.

[19] J. Kondo, "Resistance minimum in dilute magnetic alloys," *Progress of theoretical physics*, vol. 32, no. 1, pp. 37–49, 1964.

[20] C. Lacroix and M. Cyrot, "Phase diagram of the Kondo lattice," *Physical Review B*, vol. 20, no. 5, p. 1969, 1979.

[21] R. Jullien, P. Pfeuty, J. Fields, and S. Doniach, "Valence instabilities. Theoretical study of the Kondo lattice," *Le Journal de Physique Colloques*, vol. 40, no. C5, pp. C5–293, 1979.

[22] G. Aeppli and Z. Fisk, "Kondo insulators," *Comments Cond. Mat. Phys.*, vol. 16, pp. 155–170, 1992.

[23] R. M. Martin and J. W. Allen, "Theory of mixed valence: Metals or small gap insulators (invited)," *Journal of Applied Physics*, vol. 50, no. B11, pp. 7561–7566, 1979.

[24] R. Martin and J. Allen, "Classification of states at the Fermi energy in mixed valence systems," *Valence Fluctuations in Solids*, 1981.

[25] J. W. Allen, B. Batlogg, and P. Wachter, "Large low-temperature hall effect and resistivity in mixed-valent SmB_6," *Phys. Rev. B*, vol. 20, pp. 4807–4813, Dec 1979.

[26] J. Schrieffer, "The Kondo effect –the link between magnetic and nonmagnetic impurities in metals?," *Journal of Applied Physics*, vol. 38, no. 3, pp. 1143–1150, 1967.

[27] T. Kasuya, K. Kojima, and M. Kasaya, "Theory and experiment on SmB_6," *Valence Instabilities and Related Narrow-Band Phenomena, edited by* R. D. Parks (Springer US, 1977), pp. 137–152.

[28] T. Kasuya, K. Takegahara, T. Fujita, T. Tanaka, and E. Bannai, "Valence fluctuating state in SmB_6," *Le Journal de Physique Colloques*, vol. 40, no. C5, pp. C5–308, 1979.

[29] K. Klitzing, G. Dorda, and M. Pepper, "New method for high-accuracy determination of the fine-structure constant based on quantized Hall resistance," *Phys. Rev. Lett.*, vol. 45, pp. 494–497, Aug 1980.

[30] D. J. Thouless, M. Kohmoto, M. P. Nightingale, and M. den Nijs, "Quantized Hall conductance in a two-dimensional periodic potential," *Phys. Rev. Lett.*, vol. 49, pp. 405–408, Aug 1982.

[31] C. L. Kane and E. J. Mele, "Quantum spin Hall effect in graphene," *Phys. Rev. Lett.*, vol. 95, p. 226801, Nov 2005.

[32] C. L. Kane and E. J. Mele, "$\mathbb{Z}_2$ topological order and the quantum spin Hall effect," *Phys. Rev. Lett.*, vol. 95, p. 146802, Sep 2005.

[33] B. A. Bernevig, T. L. Hughes, and S.-C. Zhang, "Quantum spin Hall effect and topological phase transition in HgTe quantum wells," *Science*, vol. 314, no. 5806, pp. 1757–1761, 2006.

[34] M. König, S. Wiedmann, C. Brüne, A. Roth, H. Buhmann, L. W. Molenkamp, X.-L. Qi, and S.-C. Zhang, "Quantum spin Hall insulator state in HgTe quantum wells," *Science*, vol. 318, no. 5851, pp. 766–770, 2007.

[35] L. Fu, C. L. Kane, and E. J. Mele, "Topological insulators in three dimensions," *Phys. Rev. Lett.*, vol. 98, p. 106803, Mar 2007.

[36] J. E. Moore and L. Balents, "Topological invariants of time-reversal-invariant band structures," *Phys. Rev. B*, vol. 75, p. 121306, Mar 2007.

[37] L. Fu and C. L. Kane, "Topological insulators with inversion symmetry," *Phys. Rev. B*, vol. 76, p. 045302, Jul 2007.

[38] M. Z. Hasan and C. L. Kane, "Colloquium: Topological insulators," *Rev. Mod. Phys.*, vol. 82, pp. 3045–3067, Nov 2010.

[39] Y. Ando, "Topological insulator materials," *Journal of the Physical Society of Japan*, vol. 82, no. 10, p. 102001, 2013.

[40] S. Wolgast, C. Kurdak, K. Sun, J. W. Allen, D.-J. Kim, and Z. Fisk, "Low-temperature surface conduction in the Kondo insulator SmB_6," *Phys. Rev. B*, vol. 88, p. 180405, Nov 2013.

[41] M. Dzero, K. Sun, V. Galitski, and P. Coleman, "Topological Kondo insulators," *Phys. Rev. Lett.*, vol. 104, p. 106408, Mar 2010.

[42] T. Takimoto, "SmB_6: A promising candidate for a topological insulator," *Journal of the Physical Society of Japan*, vol. 80, no. 12, p. 123710, 2011.

[43] D. C. Tsui, H. L. Stormer, and A. C. Gossard, "Two-dimensional magnetotransport in the extreme quantum limit," *Phys. Rev. Lett.*, vol. 48, pp. 1559–1562, May 1982.

[44] K. Novoselov, A. Geim, S. Morozov, D. Jiang, M. Katsnelson, I. Grigorieva, S. Dubonos, and A. Firsov, "Two-dimensional gas of massless Dirac fermions in graphene.," *Nature*, vol. 438, no. 7065, pp. 197–200, 2005.

[45] Y. Zhang, Y.-w. Tan, H. L. Stormer, and P. Kim, "Experimental observation of the quantum Hall effect and Berry's phase in graphene," *Nature*, vol. 438, no. 7065, pp. 201–204, 2005.

[46] D. J. Griffiths, *Introduction to Electrodynamics, 3rd ed.* (Prentice Hall, 1999).

[47] J. D. Jackson, *Classical Electrodynamics, 3rd ed.* (John Wiley and Sons, Inc., 1998).

[48] P. Phillips, *Advanced Solid State Physics, 2nd ed.* (Cambridge University Press, 2012).

[49] B. K. Ridley, *Quantum Processes in Semiconductors, 4th ed.* (Oxford Science Publications, 1999).

[50] M. Born and J. R. Oppenheimer, "On the quantum theory of molecules," *Annalen der Physik*, 1927.

[51] C. Kittel, *Introduction to Solid State Physics, 8th ed.* (John Wiley and Sons, Inc., 2005).

[52] S. H. Simon, *The Oxford Solid State Basics*. (Oxford University Press, 2013).

[53] V. Ariel and A. Natan, "Electron effective mass in graphene," in *Electromagnetics in Advanced Applications (ICEAA), 2013 International Conference on*, pp. 696–698, IEEE, 2013.

[54] C. Kittel and H. Kroemer, *Thermal Physics, 2nd ed.* (W. H. Freeman and Company, 1980).

[55] K. Seeger, *Semiconductor Physics: An Introduction, 3rd ed.* (Springer-Verlag, 1985).

[56] J. M. Ziman, *Electrons and Phonons: The Theory of Transport Phenomena in Solids*. (Oxford at the Clarendon Press, 1960).

[57] A. B. Pippard, *Magnetoresistnace in Metals*. (Cambridge University Press, 1989).

[58] E. Akkermans and G. Montambaux, *Mesoscopic Physics of Electrons and Photons*. (Cambridge University Press, 2007).

[59] D. Kim, S. Thomas, T. Grant, J. Botimer, Z. Fisk, and J. Xia, "Surface hall effect and nonlocal transport in SmB_6: evidence for surface conduction," *Scientific reports*, vol. 3, 2013.

[60] G. Li, Z. Xiang, F. Yu, T. Asaba, B. Lawson, P. Cai, C. Tinsman, A. Berkley, S. Wolgast, Y. S. Eo, D.-J. Kim, C. Kurdak, J. W. Allen, K. Sun, X. H. Chen, Y. Y. Wang, Z. Fisk, and L. Li, "Two-dimensional fermi surfaces in Kondo insulator SmB_6," *Science*, vol. 346, no. 6214, pp. 1208–1212, 2014.

[61] B. S. Tan, Y.-T. Hsu, B. Zeng, M. C. Hatnean, N. Harrison, Z. Zhu, M. Hartstein, M. Kiourlappou, A. Srivastava, M. D. Johannes, T. P. Murphy, J.-H. Park, L. Balicas, G. G. Lonzarich, G. Balakrishnan, and S. E. Sebastian, "Unconventional fermi surface in an insulating state," *Science*, 2015.

[62] J. Denlinger, J. Allen, J.-S. Kang, K. Sun, J.-W. Kim, J. Shim, B. Min, D.-J. Kim, and Z. Fisk, "Temperature dependence of linked gap and surface state evolution in the mixed valent topological insulator SmB_6," *arXiv preprint arXiv:1312.6637*, 2013.

[63] J. Denlinger, S. Jang, G. Li, L. Chen, B. Lawson, T. Asaba, C. Tinsman, F. Yu, K. Sun, J. Allen, *et al.*, "Consistency of photoemission and quantum oscillations for surface states of SmB_6," *arXiv preprint arXiv:1601.07408*, 2016.

[64] N. Xu, X. Shi, P. K. Biswas, C. E. Matt, R. S. Dhaka, Y. Huang, N. C. Plumb, M. Radović, J. H. Dil, E. Pomjakushina, K. Conder, A. Amato, Z. Salman, D. M. Paul, J. Mesot, H. Ding, and M. Shi, "Surface and bulk electronic structure of the strongly correlated system SmB_6 and implications for a topological Kondo insulator," *Phys. Rev. B*, vol. 88, p. 121102, Sep 2013.

[65] J. Jiang, S. Li, T. Zhang, Z. Sun, F. Chen, Z. Ye, M. Xu, Q. Ge, S. Tan, X. Niu, *et al.*, "Observation of possible topological in-gap surface states in the Kondo insulator SmB_6 by photoemission," *Nature communications*, vol. 4, p. 3010, 2013.

[66] M. Neupane, N. Alidoust, S.-Y. Xu, T. Kondo, Y. Ishida, D. Kim, C. Liu, I. Belopolski, Y. Jo, T.-R. Chang, *et al.*, "Surface electronic structure of the topological Kondo-insulator candidate correlated electron system SmB_6," *Nature*, vol. 4, no. 2991, p. 1, 2013.

[67] N. Xu, P. Biswas, J. Dil, R. Dhaka, G. Landolt, S. Muff, C. Matt, X. Shi, N. Plumb, M. Radović, *et al.*, "Direct observation of the spin texture in SmB_6 as evidence of the topological kondo insulator," *Nature Communications*, vol. 5, p. 4566, 2014.

[68] P. Hlawenka, K. Siemensmeyer, E. Weschke, A. Varykhalov, J. Sánchez-Barriga, N. Shitsevalova, A. Dukhnenko, V. Filipov, S. Gabáni, K. Flachbart, *et al.*, "Samarium hexaboride: A trivial surface conductor," *arXiv preprint arXiv:1502.01542*, 2015.

[69] Z.-H. Zhu, A. Nicolaou, G. Levy, N. P. Butch, P. Syers, X. F. Wang, J. Paglione, G. A. Sawatzky, I. S. Elfimov, and A. Damascelli, "Polarity-driven surface metallicity in SmB_6," *Phys. Rev. Lett.*, vol. 111, p. 216402, Nov 2013.

[70] F. Lu, J. Zhao, H. Weng, Z. Fang, and X. Dai, "Correlated topological insulators with mixed valence," *Phys. Rev. Lett.*, vol. 110, p. 096401, Feb 2013.

[71] P. Moetakef, G. Ouellette, Daniel, J. Williams, J. Allen, L. Balents, D. Goldhaber-Gordon, and S. Stemmer, "Quantum oscillations from a two-dimensional electron gas at a Mott/band insulator interface," *Applied Physics Letters*, vol. 101, no. 15, p. 151604, 2012.

[72] S. Wolgast, Y. S. Eo, T. Öztürk, G. Li, Z. Xiang, C. Tinsman, T. Asaba, B. Lawson, F. Yu, J. W. Allen, K. Sun, L. Li, C. Kurdak, D.-J. Kim, and Z. Fisk, "Magneto-transport measurements of the surface states of samarium hexaboride using corbino structures," *Phys. Rev. B*, vol. 92, p. 115110, Sep 2015.

[73] S. Wolgast, Y. S. Eo, C. Kurdak, D.-J. Kim, and Z. Fisk, "Conduction through sub-surface cracks in bulk topological insulators," *arXiv preprint arXiv:1506.08233*, 2015.

[74] Z. Pei, S. Billingsley, and S. Miura, "Grinding induced subsurface cracks in silicon wafers," *International Journal of Machine Tools and Manufacture*, vol. 39, no. 7, pp. 1103–1116, 1999.

[75] T. Mchedlidze, I. Yonenaga, and K. Sumino, "Subsurface damage in single diamond tool machined Si wafers," in *Materials Science Forum*, vol. 196, pp. 1841–1846, Trans Tech Publ, 1995.

[76] N. J. Laurita, C. M. Morris, S. M. Koohpayeh, P. F. S. Rosa, W. A. Phelan, Z. Fisk, T. M. McQueen, and N. P. Armitage, "Anomalous three-dimensional bulk ac conduction within the kondo gap of SmB_6 single crystals," *Phys. Rev. B*, vol. 94, p. 165154, Oct 2016.

[77] M. Ye, J. Allen, and K. Sun, "Topological crystalline Kondo insulators and universal topological surface states of SmB_6," *arXiv preprint arXiv:1307.7191*, 2013.

[78] X. Hong, K. Zou, and J. Zhu, "Quantum scattering time and its implications on scattering sources in graphene," *Phys. Rev. B*, vol. 80, p. 241415, Dec 2009.

[79] E. H. Hwang and S. Das Sarma, "Single-particle relaxation time versus transport scattering time in a two-dimensional graphene layer," *Phys. Rev. B*, vol. 77, p. 195412, May 2008.

[80] A. Damascelli, Z. Hussain, and Z.-X. Shen, "Angle-resolved photoemission studies of the cuprate superconductors," *Reviews of modern physics*, vol. 75, no. 2, p. 473, 2003.

[81] P. Coleman, *Introduction to Manybody Physics*. (Cambridge University Press, 2015).

[82] P. Syers, D. Kim, M. S. Fuhrer, and J. Paglione, "Tuning bulk and surface conduction in the proposed topological Kondo insulator SmB_6," *Phys. Rev. Lett.*, vol. 114, p. 096601, Mar 2015.

[83] S. Thomas, D. J. Kim, S. B. Chung, T. Grant, Z. Fisk, and J. Xia, "Weak antilocalization and linear magnetoresistance in the surface state of SmB_6," *Phys. Rev. B*, vol. 94, p. 205114, Nov 2016.

[84] S. Lee, X. Zhang, Y. Liang, S. W. Fackler, J. Yong, X. Wang, J. Paglione, R. L. Greene, and I. Takeuchi, "Observation of the superconducting proximity effect in the surface state of smb_6 thin films," *Phys. Rev. X*, vol. 6, p. 031031, Aug 2016.

[85] S. Adhikari, Y. Ma, Z. Fisk, J. Xia, C.-B. Eom, and C. Cen, "Ultrafast observation of electron hybridization and in-gap states formation in Kondo insulator SmB_6," *arXiv preprint arXiv:1502.04441*, 2015.

[86] Y. S. Eo, K. Sun, C. Kurdak, D.-J. Kim, and Z. Fisk, "A new method for characterizing bulk and surface conductivities of three-dimensional topological insulators: Inverted resistance measurements," *arXiv preprint arXiv:1708.05762*, 2017.

[87] M. Kasaya, H. Kimura, Y. Isikawa, T. Fujita, and T. Kasuya, "Valence instabilities and electrical properties of the La-and Yb-substituted SmB_6," in *Valence fluctuations in solids,* edited by L. Falicov, W. Hanke, and M. Maple (North − Holland Publishing, 1981).

[88] S. Yeo, K. Song, N. Hur, Z. Fisk, and P. Schlottmann, "Effects of Eu doping on SmB_6 single crystals," *Phys. Rev. B*, vol. 85, p. 115125, Mar 2012.

[89] S. Gabni, M. Orend, G. Prist, E. Gao, P. Diko, S. Piovari, V. Glushkov, N. Sluchanko, A. Levchenko, N. Shitsevalova, and K. Flachbart, "Transport properties of variously doped SmB_6," *Philosophical Magazine*, vol. 96, no. 31, pp. 3274–3283, 2016.

[90] B. Y. Kang, C.-H. Min, S. S. Lee, M. S. Song, K. K. Cho, and B. K. Cho, "Magnetic and nonmagnetic doping dependence of the conducting surface states in SmB_6," *Phys. Rev. B*, vol. 94, p. 165102, Oct 2016.

[91] D. Kim, J. Xia, Z. Fisk, *et al.*, "Topological surface state in the Kondo insulator samarium hexaboride," *Nature Materials*, vol. 13, no. 5, pp. 466–470, 2014.

[92] N. Mott, "Conduction in non-crystalline materials: Localized states in a pseudogap and near extremities of conduction and valence bands," *Philosophical Magazine*, vol. 19, no. 160, pp. 835–852, 1969.

[93] A. Rakoski, Y. S. Eo, K. Sun, and C. Kurdak, "Understanding low-temperature bulk transport in samarium hexaboride without relying on in-gap bulk states," *Phys. Rev. B*, vol. 95, p. 195133, May 2017.

[94] B. Gorshunov, N. Sluchanko, A. Volkov, M. Dressel, G. Knebel, A. Loidl, and S. Kunii, "Low-energy electrodynamics of SmB_6," *Phys. Rev. B*, vol. 59, pp. 1808–1814, Jan 1999.

[95] J. C. Cooley, M. C. Aronson, Z. Fisk, and P. C. Canfield, "SmB_6: Kondo insulator or exotic metal?," *Phys. Rev. Lett.*, vol. 74, pp. 1629–1632, Feb 1995.

[96] N. Sluchanko, A. Volkov, V. Glushkov, B. Gorshunov, S. Demishev, M. Kondrin, A. Pronin, N. Samarin, Y. Bruynseraede, V. Moshchalkov, *et al.*, "Nature of the low-temperature anomalies in the physical properties of the intermediate-valent compound SmB_6," *Journal of Experimental and Theoretical Physics*, vol. 88, no. 3, pp. 533–537, 1999.

[97] J. C. Cooley, *High Pressure Transport Measurements on the Rare Earth Systems* SmB_6*,* $Ce_3Bi_4Pt_3$*, and* EuB_6. PhD thesis, University of Michigan, 1997.

[98] M. Brahlek, N. Koirala, N. Bansal, and S. Oh, "Transport properties of topological insulators: Band bending, bulk metal-to-insulator transition, and weak anti-localization," *Solid State Communications*, vol. 215, pp. 54–62, 2015.

[99] J. Bardeen, L. N. Cooper, and J. R. Schrieffer, "Theory of superconductivity," *Phys. Rev.*, vol. 108, pp. 1175–1204, Dec 1957.

[100] M. A. Woolf and F. Reif, "Effect of magnetic impurities on the density of states of superconductors," *Phys. Rev.*, vol. 137, pp. A557–A564, Jan 1965.